Martin Lucht

The Wavelength of the 14.4 keV Mössbauer Radiation in ^{57}Fe:
A Novel Length Standard For Atomic Scales

The Wavelength of the
14.4 keV Mössbauer Radiation
in ^{57}Fe:
A Novel Length Standard
For Atomic Scales

New Measurements and First Applications

Dissertation

zur Erlangung des Doktorgrades
des Fachbereichs Physik
der Universität Hamburg

vorgelegt von
Martin Lucht
aus Lübeck

Hamburg
2005

Abstract

The wavelength of the Mössbauer radiation of ^{57}Fe, λ_M, has been measured in an experiment using Bragg backscattering from a Si reference crystal with precisely known lattice spacing. The latest measured value, obtained at the 1 km beamline at SPring-8 (Hyogo, Japan) in the year 2002, is $\lambda_\mathrm{M} = 86.025\,587\,(26)$ pm. The wavelength of the Mössbauer radiation of ^{57}Fe is ideal as a new length standard for atomic scales due to its unique sharpness, stability and ease of reproduction. In other experiments the new length standard has been successfully applied in the measurement of the lattice parameters of $\alpha{-}\mathrm{Al}_2\mathrm{O}_3$ in the temperature range from 4.5 to 374 K, and in the measurement of the wavelength of the Mössbauer radiation of the isotopes ^{151}Eu, ^{119}Sn, and ^{161}Dy.

Zusammenfassung

Die Wellenlänge der Mößbauer-Strahlung von ^{57}Fe, λ_M, wurde gemessen durch Anwendung von Bragg-Rückstreuung an einem Si-Referenzkristall mit sehr genau bekanntem Gitterebenenabstand. Der neueste an der 1 km-Beamline bei SPring-8 (Hyogo, Japan) im Jahr 2002 gemessene Wert beträgt $\lambda_\mathrm{M} = 86.025\,587\,(26)$ pm. Die Wellenlänge der Mößbauer-Strahlung von ^{57}Fe ist aufgrund ihrer einzigartigen Schärfe, Stabilität und leichten Reproduzierbarkeit ideal geeignet als Längenstandard für atomare Größenordnungen. In weiteren Experimenten wurde der neue Längenstandard erfolgreich angewendet, um die Gitterparameter von $\alpha{-}\mathrm{Al}_2\mathrm{O}_3$ im Temperaturbereich von 4.5 bis 374 K sowie die Wellenlängen der Mößbauer-Strahlung der Isotope ^{151}Eu, ^{119}Sn und ^{161}Dy zu messen.

Contents

List of Figures

List of Tables

Chapter 1

Introduction

Length measurements belong to the most important experimental tasks, not only in natural science but also in engineering and daily life. They are typically performed by comparison of the length under study with a *length standard*, i.e. a length that is very well known in SI units, and reproducible with reasonable effort.

The SI unit meter is determined by referring to the definition of the speed of light: $c = 299\,792\,458\,\mathrm{m\,s^{-1}}$. Herein, the second is defined as $9\,192\,631\,770$ times the oscillation period of the radiation originating from the transition between the two hyperfine structure levels of the ground state of ^{133}Cs atoms.

In the region of optical wavelengths there are lasers available with a relative frequency accuracy and stability of better than 10^{-11}. The frequency f of such devices can be measured against the frequency of the abovementioned ^{133}Cs radiation. The wavelength of the laser radiation $l = c/f$ is then also known with an accuracy of better than 10^{-11}. In this way, the laser becomes both a frequency and a wavelength standard. E.g. the PTB[a] uses the radiation of iodine stabilized helium-neon lasers with a wavelength of $\approx 500\,\mathrm{nm}$ as standard devices.

In the hard x-ray region however, no such precise length standard was available in the past. The most common length standard in use was the lattice parameter of Si which is known with 2×10^{-8} uncertainty for some Si reference crystals specially prepared for this purpose. Combined x-ray and optical interferometry techniques were used to measure the ratio of the Si $(2\,2\,0)$ lattice spacing and optical wavelength standards by Bergamin et al. (1999). It is considered possible to achieve a 10^{-9} uncertainty for the measurement of the Si lattice parameter by further development of the experimental method. However, an improvement beyond this limit is inhibited by the quality of the Si reference crystal iself (Bergamin et al., 1999).

Obviously the Si length standard is only valid for a well defined temperature and pressure. For $T = 22.500\,^\circ\mathrm{C}$ and in vacuum, it has been determined to be $5.431\,020\,88\,(16) \times 10^{-10}\,\mathrm{m}$ (Mohr and Taylor, 2000). The need for maintenance of an accurate temperature makes the experimental use of the Si length standard quite difficult.

On the other hand, the wavelength of the Mössbauer radiation of ^{57}Fe nuclei, $\lambda_\mathrm{M} \approx 0.86\,\text{Å}$, is an ideal candidate for a new length standard in the hard x-ray region. The Mössbauer radiation of ^{57}Fe is originating from the decay of the ^{57}Fe nuclei from the first excited state to the ground state. The lifetime of the excited state is $\tau = 141\,\mathrm{ns}$, thus the energy width is determined by the uncertainty principle $\Gamma\tau = \hbar$ to $\Gamma = 4.8 \times 10^{-9}\,\mathrm{eV}$. Thus, with a radiation energy

---

[a] Physikalisch-Technische Bundesanstalt, Braunschweig, Germany

1

of $\approx 14.4\,\text{keV}$, the relative uncertainty of λ_M is 3×10^{-13}. Due to the so-called hyperfine interactions between the nuclei and their environment, e.g. the electrons in the atomic shell, the relative shift of the splitted line (cf. Section 2.1) may reach up to 10^{-11}.

Thus, even if nothing is known about the hyperfine interactions, the wavelength of the Mössbauer radiation of ^{57}Fe would be about 100 times more accurate than the Si length standard could ever be under optimal conditions.

Although the investigation of the energy *shifts* of the Mössbauer radiation of ^{57}Fe due to hyperfine interactions is for decades a widely applied technique to gather information about e.g. pressure, chemical composition, or magnetic fields around the ^{57}Fe nuclei, the absolute value of λ_M was known only coarsely for a long time.

It was first proposed as a wavelength standard in 1965 by Bearden (1965). However, at that time, only radioactive sources were available to generate Mössbauer radiation. Bearden concluded that the brightness of his 200 mCi source had to be increased by a factor of 100 to make the Mössbauer wavelength standard experimentally feasible with an accuracy of 10^{-6}. This was not possible since the brightness of radioactive sources is limited due to self-absorption.

This situation changed drastically with the possibility to generate the Mössbauer radiation of ^{57}Fe at synchrotron radiation sources, which was first demonstrated by Gerdau et al. (1985) and rapidly evolved to a well established technique in many fields of science (cf. Gerdau and de Waard, 1999/2000). Today, at modern synchrotron radiation facilities of the third generation, one can create a well collimated Mössbauer radiation beam with a countrate of several kHz simply by putting an enriched ^{57}Fe foil into the premonochromatized synchrotron radiation beam. Since the quanta emitted from the ^{57}Fe foil by means of coherent nuclear resonant forward scattering have an average delay of about 50 ns (Shvyd'ko et al., 1991), it is easy to distinguish the Mössbauer radiation from the prompt synchrotron radiation pulses with $\approx 100\,\text{ps}$ duration using time-resolving detectors with $\lesssim 1\,\text{ns}$ resolution.

Several experiments have been made during the recent years to measure the wavelength of the Mössbauer radiation of ^{57}Fe, λ_M, using synchrotron radiation. Xiaowei et al. (2000) have measured λ_M with a relative uncertainty of 0.6×10^{-6} using a method proposed by Siddons et al. (1988). The lattice parameters of several Si samples were compared with λ_M. The averaged result reported by the autors is $\lambda_\text{M} = 86.02557(5)\,\text{pm}$.

This thesis will focus on another experimental technique developed in the group of Shvyd'ko at the University of Hamburg (Germany). Here we have measured λ_M using almost exact backscattering of x-rays from a calibrated Si reference crystal which is kept in an environment with precisely controlled temperature and pressure. Our result recently reported is $\lambda_\text{M} = 86.025474(16)\,\text{pm}$; the relative uncertainty is thus 0.19×10^{-6} (Shvyd'ko et al., 2000).

These two results are already a reliable base for use of the Mössbauer wavelength standard to measure radiation wavelengths or lattice parameters, although they still differ by 1.1×10^{-6} which is outside the rated uncertainty

range of the individual results. Furthermore, the uncertainty of the result from Shvyd'ko et al. (2000) is not as low as one would expect from the theory for this method. The backscattering approach for measurement of the Mössbauer radiation wavelength of ^{57}Fe has therefore undergone a lot of improvements and additional experiments since the publication from Shvyd'ko et al. (2000).
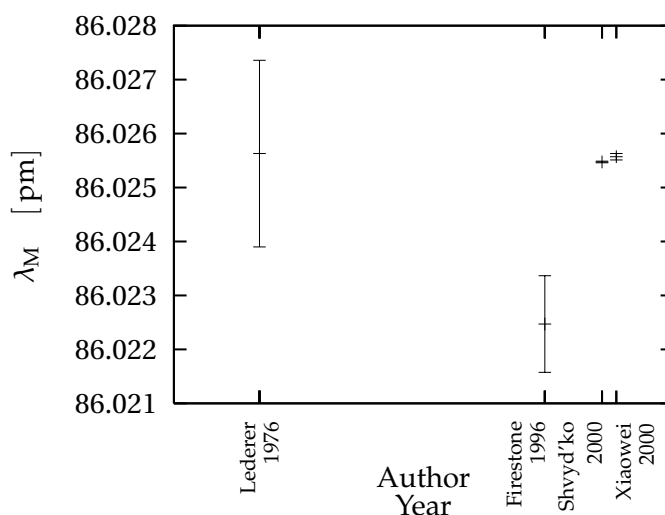
Fig. 1.0.1: Historical overview of the published results of the Mössbauer radiation wavelength of ^{57}Fe.

The development of measured values and uncertainties of the wavelength of the Mössbauer radiation of ^{57}Fe is summarized in Fig. 1.0.1, together with the originating literature references. Herein, the value published in 1976 by Lederer and Shirley (1976) is derived from Bearden (1965). The recent measurements using synchrotron radiation by Shvyd'ko et al. (2000); Xiaowei et al. (2000) show a remarkably improvement in their uncertainty over the past results (Firestone et al., 1996; Lederer and Shirley, 1976) obtained with classical methods using radioactive sources.

The experimental method presented in this thesis allows to measure the ratio between the wavelength of the Mössbauer radiation of ^{57}Fe (or some other Mössbauer isotope) and the lattice parameters of some single crystal. In the first experiment, the Mössbauer radiation wavelength of ^{57}Fe is determined in units of the lattice parameter of an almost perfect Si reference crystal that is known with 6×10^{-8} precision at 22.5 °C. This result allows us to express the Mössbauer radiation wavelength of ^{57}Fe itself in SI units. In subsequent experiments deploying the same method, the Mössbauer radiation wavelength of ^{57}Fe is used as the length standard to measure the lattice parameters of $\alpha-\text{Al}_2\text{O}_3$. To determine the Mössbauer radiation wavelengths of other isotopes than ^{57}Fe, like ^{119}Sn, ^{151}Eu, and ^{161}Dy, an $\alpha-\text{Al}_2\text{O}_3$ single crystal is used, and its orientation and temperature are adjusted to back-reflect the Mössbauer radiation of the respective isotope. By this procedure, the wavelength of the Mössbauer radiation of one of the abovementioned isotopes is

R_{PT100} $[\,\Omega\,]$
R_{Cernox} $[\,\Omega\,]$
ΔT $[\,\text{K}\,]$

transferred to the interplanar distance in $\alpha-\text{Al}_2\text{O}_3$. The latter one can then be determined by measuring the ratio of the wavelength of the Mössbauer radiation of ^{57}Fe and the lattice parameters of $\alpha-\text{Al}_2\text{O}_3$ at the same temperature.
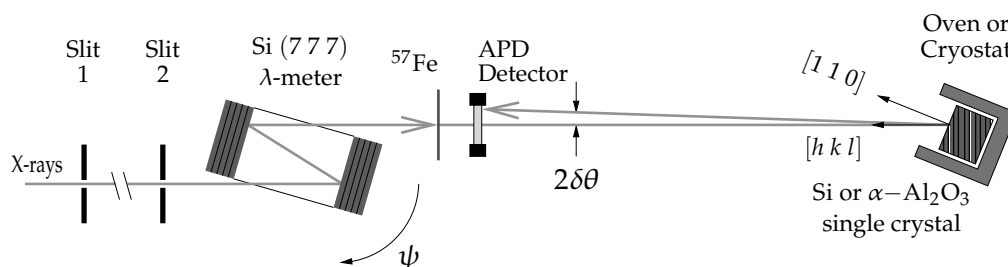
Fig. 1.0.2: Simplified overview of the experimental setup for the measurement of the ratio between the lattice parameters of a single crystal and the Mössbauer radiation wavelength of ^{57}Fe.

A simplified overview of the experimental setup is shown in Fig. 1.0.2. The basic components are an ^{57}Fe foil in the incoming synchrotron radiation beam, the beforementioned Si or $\alpha-\text{Al}_2\text{O}_3$ single crystal, which can be oriented in such a way that the incoming beam is exactly back-reflected (i.e. some set of atomic planes $(h\,k\,l)$ must be perpendicular to the beam), and a Si $(7\,7\,7)$ channel-cut crystal which can be rotated by an angle ψ to tune a narrow energy band selected from the incoming beam to either the energy of the back-reflected beam or of the Mössbauer radiation of ^{57}Fe. The angular difference between transmission of Mössbauer radiation of ^{57}Fe and back-reflected beam is measured for some back-reflections with different Bragg energies. If n is the number of independent lattice parameters in the reference crystal, then one can calculate from $n+1$ angular difference measurements the ratio between the Mössbauer radiation wavelength of ^{57}Fe and the lattice parameters of the reference crystal and the Si $(7\,7\,7)$ channel-cut crystal. Since the Si $(7\,7\,7)$ channel-cut crystal is used to measure differences of the wavelength λ it will be named *λ-meter* in the following. The setup is accomplished by slits which are used to collimate the beam and to adjust exact backscattering, and APD[a] detectors. For a Si backscattering crystal, it is necessary to perform the measurements at a small deviation $\delta\theta \approx 100\,\mu\text{rad}$ from exact backscattering to avoid the intensity loss and energy shift which are caused by multiple beam diffraction at exact backscattering.

The experimental setup will be discussed in much more detail in Chapter 4.

The measurements of the wavelength of the Mössbauer radiation of ^{57}Fe have been performed at the HASYLAB[b] beamline BW4, at the SRI-CAT 3ID beamline at APS[c], and at the BL29XUL beamline at SPring-8[d]. The latter experimental station was chosen because it provides a distance between undulator and experiment of about 1 km, thus allowing an energy-independent beam

---

[a] Avalanche Photo Diode
[b] Hamburger Synchrotronstrahlungslabor, Hamburg, Germany
[c] Advanced Photon Source, Argonne, Il., U.S.A.
[d] Super Photon Ring 8 GeV, Hyogo, Japan

collimation to 1 μrad angular width by placing two 1 mm slits at the beginning and the end of the beam path. The lattice parameters of sapphire were measured above room temperature at SRI-CAT 3ID, and for low temperature at the PETRA[a] beamline at HASYLAB.

This thesis is organized as follows: In Chapter 2 we will discuss the theory of some subjects which are important prerequisites to understand the experiments described in this work. These are the generation and properties of Mössbauer radiation, exact Bragg backscattering of x-rays, multiple beam diffraction, and thermal expansion of solids.

Chapter 3 will first deal with the requirements on temperature stability and accuracy which are necessary to use the Si lattice parameter as a length standard to measure the Mössbauer radiation wavelength of ^{57}Fe. As these turn out to be in the mK range, a big technical effort is required to fulfill them. This will be presented in detail, including special thermostats, selection and calibration of temperature sensors, and a discussion of possible temperature errors that still persist in the experimental equipment.

In Chapter 4 we will first develop the experimental method which is used to measure the the lattice parameters of a crystal in units of the wavelength of the Mössbauer radiation of ^{57}Fe, or vice versa. Then the wavelength of the Mössbauer radiation of ^{57}Fe in units of the lattice parameter of Si will be derived from the raw experimental data. This will lead to the *Mössbauer wavelength standard*, i.e. the Mössbauer radiation wavelength of ^{57}Fe in meter units, since the lattice parameter of the Si reference crystal in use is very precisely known. Here we will also discuss the progress of some technical aspects of the experimental setup at different synchrotron radiation facilities, and some error sources which are attributed to remaining technical limits in the experimental setup.

In Chapter 5 some further experiments will be presented and discussed, where the Mössbauer wavelength standard was applied to measure precisely the wavelength of the Mössbauer radiations of ^{119}Sn, ^{151}Eu, and ^{161}Dy, as well as the lattice parameters of $\alpha-Al_2O_3$ in a broad temperature range from 4.5 K to 374 K.

Finally, in Chapter 6, some future applications of the experimental results will be proposed. Among them are the use of Mössbauer radiation wavelengths of different isotopes as a set of reference wavelengths or energies in the hard x-ray regime, as well as the cryogenic $\alpha-Al_2O_3$ backscattering monochromator. Furthermore, we will discuss how one could improve the knowledge about the value of the wavelength of the Mössbauer radiation of ^{57}Fe over the current limit—which is finally determined by the uncertainty of the Si lattice parameter—by coupling the Mössbauer radiation wavelength of ^{57}Fe directly to the wavelength of optical laser radiation, using a combined x-ray/optical resonator of the Fabry-Pérot type.

---

[a] Positron Electron Tandem Ring Accelerator

Chapter 2

Theory

2.1. Mössbauer radiation

The *nuclear resonant radiation* of ^{57}Fe with $E_M \approx 14.4\,\mathrm{keV}$ is originating from the decay of ^{57}Fe nuclei from their first excited state to the ground state. From the lifetime of the excited state, $\tau = 141\,\mathrm{ns}$, the energy bandwidth of the radiation is determined as $\Gamma = 4.8 \times 10^{-9}\,\mathrm{eV}$ by use of the uncertainty principle $\Gamma\tau = \hbar$. Thus, the relative linewidth of E_M is only $\Gamma/E_M \approx 3 \times 10^{-13}$.

The transition wavelength may be, however, considerably affected by the hyperfine interactions between the nuclei and their environment, e.g. the electrons in the atomic shell or externally applied magnetic fields. Thus the nuclear states of ^{57}Fe with different magnetic quantum numbers are no longer degenerate, and the transition from the first excited to the ground state is split up into 6 lines of slightly different energy. This may increase the uncertainty of λ_M to about 10^{-11}.

Closely related to the nuclear resonant radiation is the effect of *recoilless nuclear resonance absorption of gamma radiation* which was first demonstrated with the 129 keV transition of ^{191}Ir by Mössbauer (1958), and awarded with the Nobel prize in 1961. It is therefore widely known as the *Mössbauer effect*. Scientific interest switched fastly to ^{57}Fe, not only because of the unique sharpness of the 14.4 keV resonance and the easier experimental conditions, but also due to the importance of iron in many fields of science, like magnetism, geology, material science, chemistry, biology and medicine.

Typical Mössbauer experiments make only use of the unique sharpness and stability of the nuclear resonance, and the fact that the energy shifts arising from the hyperfine interactions can be precisely measured. Thus, spectroscopy with ultimate energy resolution becomes possible. An overview of classical applications of the Mössbauer effect is given e.g. by Gütlich et al. (1978), and of more recent applications using synchrotron radiation by Gerdau and de Waard (1999/2000). The knowledge about the value of the wavelength of the Mössbauer radiation of ^{57}Fe, λ_M, remained however rather coarse for decades, cf. Fig. 1.0.1. The present report will only focus on the absolute value of λ_M itself, but not on the wide field of science which is opened up by the study of the hyperfine interactions.
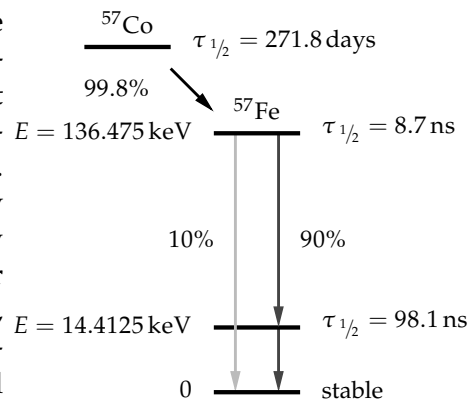
Fig. 2.1.1: Generation of 14.4 keV Mössbauer radiation by the radioactive decay of ^{57}Co

T [K]
R_{PT100} [Ω]
R_{Cernox} [Ω]
ΔT [K]
Slit 1
Slit 2
Si (7 7 7)
λ-meter
^{57}Fe
APD
Detector
Oven or
Cryostat
Si or $\alpha-Al_2O_3$
single crystal
[1 1 0]
[h k l]
ψ
χ-rays
2δθ

Besides ^{57}Fe, there are many other isotopes which show nuclear resonances with similar properties. Among them are ^{151}Eu, ^{119}Sn, and ^{161}Dy, which will be addressed later in this report, see Section 5.2.

Mössbauer radiation can be generated either by the nuclear decay of radioactive sources, or by synchrotron radiation. In the case of ^{57}Fe, one may use a source made of ^{57}Co, with the decay scheme shown in Fig. 2.1.1. The brightness of radioactive sources is, however, limited by self-absorption. E.g., the spectral flux of of a 250 mCi ^{57}Co source into a solid angle of 20×20 µrad^2 is only 1 photon s$^{-1}\Gamma^{-1}$. Furthermore, for some interesting Mössbauer isotopes the handling of radioactive sources may become difficult if the mother isotope has a short lifetime.

PSfrag replacements
T [°C]
T [K]
R_{PT100} [Ω]
R_{Cernox} [Ω]
ΔT [K]
Slit 1
Slit 2
Si (7 7 7)
λ-meter
^{57}Fe
APD
Detector
Oven or
Cryostat
Si or $\alpha-Al_2O_3$
single crystal
[1 1 0]
[h k l]
ψ
χ-rays
2δθ

e^+ or e^- Storage ring

Monochromator ^{57}Fe foil Detector

synchrotron radiation Mössbauer radiation
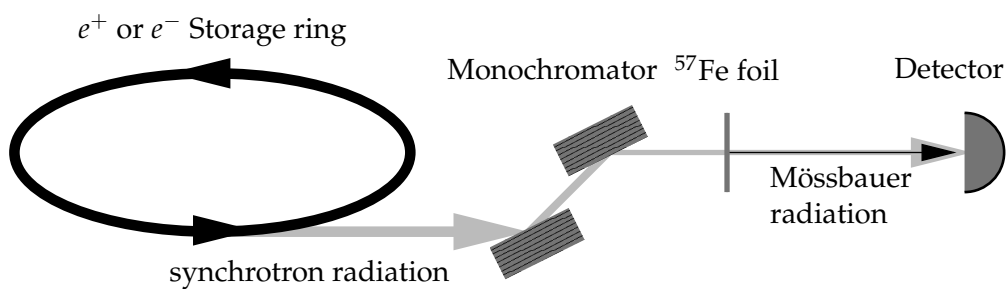
Fig. 2.1.2: Generation of Mössbauer radiation by means of synchrotron radiation
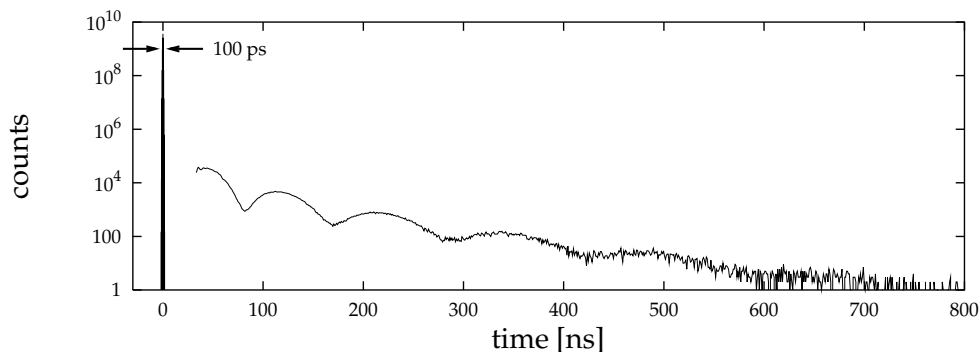
Fig. 2.1.3: Time structure of the detected photons in a Mössbauer experiment using synchrotron radiation

Since the breakthrough experiment from Gerdau et al. (1985) it is also possible to generate Mössbauer radiation by means of synchrotron radiation. The general setup of such an experiment is shown in Fig. 2.1.2. Electromagnetic radiation is generated by electrons in a storage ring being accelerated perpendicular to their flight direction while passing through a bending magnet, a wiggler, or an undulator. The initially almost "white" spectrum is monochromatized to a bandwidth of 1 eV or less[a)] in the 14.4 keV range, and then trans-

---

[a)]Most experiments use a pre-monochromator with $\approx 1\,$eV bandpass which takes the heat load out of the beam, and a second high-resolution monochromator with only $\approx 1\,$meV band-

mitted through a foil made of ^{57}Fe. If the wavelength of the x-rays transmitted by the monochromator coincides with the wavelength of the Mössbauer radiation of ^{57}Fe, the ^{57}Fe nuclei are excited and emit Mössbauer photons with coherent enhancement in the forward direction (Hastings et al., 1991; Shvyd'ko et al., 1991) with an average delay of $\tau = 141$ ns. The x-rays and the Mössbauer radiation hit the detector, typically a silicon APD (Baron, 2000). Since the synchrotron radiation comes in sharp pulses with less than 100 ps duration and a delay of several 100 ns in between, and the time resolution of an APD is ≈ 1 ns, one can easily distinguish between the x-rays in the prompt synchrotron radiation pulse and the delayed Mössbauer photons by blocking the prompt pulse electronically. A typical time structure is shown in Fig. 2.1.3. The characteristic pattern ("beating") in the time structure of the delayed photons is attributed to the hyperfine splitting of the nuclear resonance energy.

At modern synchrotron radiation facilities of the third generation the brightness of the generated Mössbauer radiation is by many orders of magnitude superior to radioactive sources. Typical values of the spectral flux into a solid angle of $20 \times 20 \, \mu\text{rad}^2$ at HASYLAB, ESRF[a], APS, SPring-8, and XFEL[b][c] are given in Tab. 2.1.1.

SR facility	HASYLAB		ESRF	APS	SPring-8	XFEL
Beamline	BW4	PETRA 1	ID18, ID22	ID3		
Flux $\left[\text{s}^{-1}\Gamma^{-1} \right]$	3×10^2	2×10^3	5×10^4	5×10^4	5×10^4	2×10^7

Tab. 2.1.1: Spectral flux of Mössbauer radiation of ^{57}Fe at different synchrotron radiation facilities

2.2.   Exact Bragg backscattering of x-rays

In the following, the dynamical theory of x-ray diffraction in perfect crystals will be outlined with a special focus on the backscattering geometry. The dynamical theory of two-beam diffraction in the backscattering case was discussed by Brümmer et al. (1979); Caticha and Caticha-Ellis (1982); Graeff and Materlik (1982); Kohra and Matsushita (1972). Some special cases of backscattering where multi-beam diffraction effects are considered were addressed in Kohn et al. (1999); Sutter (2000). A summary of the dynamical theory, with regards to the experiments reported in this thesis, is also given in Shvyd'ko (2002, 2004). The subsequent discussion will follow Shvyd'ko (2002).

The two-beam diffraction case will be considered first. Some expressions will be derived which enable the evaluation of the angular, energy, and tem-

---

pass which cuts down the ratio between Mössbauer photons and synchrotron radiation photons to a reasonable value that can be handled by the detector.
[a]European Synchrotron Radiation Facility, Grenoble, France
[b]X-ray Free Electron Laser (currently under development at DESY, Hamburg, Germany)
[c]At the XFEL, the solid angle into which the x-rays are emitted is only $1 \times 1 \, \mu\text{rad}^2$.

perature dependence of the crystal reflectivity[a]. The derivation relies on the fact that the general equations of the dynamical theory of diffraction (see von Laue (1931), and also Azaroff et al. (1974); Batterman and Cole (1964); Pinsker (1978); Zachariasen (1945)) are valid in the backscattering case, too. However, the parameter α denoting the deviation from Bragg's condition is defined differently here. A new expression for α which is valid in backscattering geometry has been reported by Caticha and Caticha-Ellis (1982). A general expression for α valid for any angle of incidence was given by Shvyd'ko and Gerdau (1999) and used in Shvyd'ko et al. (1998). The latter expression allows using the dynamical theory of diffraction in a generalized form, without the need to distinguish between "standard" and "backscattering" regimes for the glancing angle.

We consider scattering of a plane monochromatic electromagnetic wave

$$\mathcal{E}(\boldsymbol{r}, t) = \mathcal{E}_0\, e^{i\,(\boldsymbol{K_0}\cdot\boldsymbol{r} - Et/\hbar)} \tag{2.2.1}$$

from a perfect crystal, with the energy E and the wave vector $\boldsymbol{K_0}$, which are related by $|\boldsymbol{K_0}| = K = E/\hbar c = 2\pi/\lambda$. The wave is linearly polarized.

The crystal is a plate with the thickness d. Inside the crystal, a radiation field with the electric vector $\mathcal{D}(\boldsymbol{r}, t) = e^{-i\,Et/\hbar}\mathcal{D}(\boldsymbol{r})$ is excited by the incident wave. The spatial part $\mathcal{D}(\boldsymbol{r})$ is a solution of the wave equation

$$(-\nabla^2 - K^2)\,\mathcal{D}(\boldsymbol{r}) = K^2\chi(\boldsymbol{r})\,\mathcal{D}(\boldsymbol{r}). \tag{2.2.2}$$

The wave equation is derived directly from Maxwell's equations for a medium with the electric susceptibility $\chi(\boldsymbol{r})/4\pi$, with the assumption that the electric field inside the crystal remains practically transverse. Since $\chi(\boldsymbol{r})$ is a continuous periodic function in space with the same symmetry as the crystal lattice, it can be written as Fourier series

$$\chi(\boldsymbol{r}) = \sum_{\boldsymbol{H}} \chi_{\boldsymbol{H}}\, e^{i\,\boldsymbol{H}\cdot\boldsymbol{r}} \tag{2.2.3}$$

with the reciprocal lattice vectors $\boldsymbol{H}$ of the crystal. The Fourier components of the electric susceptibility are

$$\chi_{\boldsymbol{H}} = -r_e\, \frac{\lambda^2}{\pi V}\, F_{\boldsymbol{H}} \tag{2.2.4}$$

with the classical electron radius r_e, the volume V of the unit cell, and the structure factor of the unit cell

$$F_{\boldsymbol{H}} = \sum_{n} f_n(\boldsymbol{H})\, e^{i\,\boldsymbol{H}\cdot\boldsymbol{r}_n}\, e^{-W_n(\boldsymbol{H})}. \tag{2.2.5}$$

Herein,

$$f_n(\boldsymbol{H}) = f_n^{(0)}(\boldsymbol{H}) + f_n'(\lambda) + i\, f_n''(\lambda) \tag{2.2.6}$$

---

[a]The dynamical theory allows also for the evaluation of the time dependence of diffraction (see e.g. Shvyd'ko (2002, 2004)). This is of special interest for x-ray Fabry-Pérot resonators and for the upcoming synchrotron radiation sources of the fourth generation, which will generate radiation pulses of only 0.1 ps duration

is the atomic scattering amplitude, where $f_n^{(0)}$ is the atomic form factor, and $f_n'(\lambda)$ and $f_n''(\lambda)$ are the anomalous scattering corrections of an atom located at a point r_n in the unit cell.[a)] These corrections are wavelength dependent. Their values, which were computed using relativistic Hartree-Fock-Slater wave functions, are reported in Kissel and Pratt (1990); Kissel et al. (1995).

The term e^{-W_n} in Eq. 2.2.5 is the square root of the Debye-Waller factor (cf. Ziman, 1969), which is measuring the thermal vibrations of the atoms. The definition of the Debye-Waller factor reads

$$
\begin{aligned}
f_{\mathrm{DW}_n}(H) &= e^{-2W_n(H)} \\
W_n(H) &= \frac{B_n(H)}{4\,d_H^2} \\
B_n(H) &= 8\,\pi^2\,\langle u_H^2\rangle_n,
\end{aligned}
$$
(2.2.7)

with $\langle u_H^2\rangle_n$ the mean square displacement of the atom from its equilibrium position in the unit cell, projected on the direction of the scattering vector H.

For hard x-rays with $\lambda = 10\ldots100\,\mathrm{pm}$, the Fourier coefficients χ_H in Eq. 2.2.3 are negative with typical values below 10^{-5}.

The classical derivation of Eqs. 2.2.4, 2.2.5 can be found e.g. in Azaroff et al. (1974); Batterman and Cole (1964); James (1950); Pinsker (1978); Zachariasen (1945). Afanas'ev and Kagan (1967) have given a quantum mechanical derivation with a thorough account of the lattice vibrations.

The reciprocal lattice vectors of the crystal lattice are in general expressed as $H = hb_1 + kb_2 + lb_3$, where h, k, l are integers known as the Miller indices, and b_1, b_2, b_3 is a set of linear independent vectors, called reciprocal lattice unit vectors. The atomic planes perpendicular to H are denoted as $(h\,k\,l)$. The interplanar distance between the atomic planes $(h\,k\,l)$ is

$$
d_{(h\,k\,l)} = \frac{2\pi}{H}.
$$
(2.2.8)

Since $\chi(r)$ is periodic, the solution of the wave equation Eq. 2.2.2 can be expressed as a Bloch wave (cf. Ziman, 1969):

$$
\mathfrak{D}(r) = e^{i\,k_0\cdot r}\sum_H \mathfrak{D}_H\,e^{i\,H\cdot r} = \sum_H \mathfrak{D}_H\,e^{i\,k_H\cdot r}
$$
(2.2.9)

with

$$
k_H = k_0 + H.
$$
(2.2.10)

Thus, the radiation field inside the lattice appears as a set of plane waves with the wave vectors k_H. The vector amplitudes $\mathfrak{D}_H$ of the plane waves are the solutions of the following system of linear algebraic equations which can be derived by substituting Eq. 2.2.9 into Eq. 2.2.2:

$$
\frac{k_H^2 - K^2}{K^2}\mathfrak{D}_H = \sum_G \chi_{H-G}\,\mathfrak{D}_G.
$$
(2.2.11)

[a)]In the following, we will generally notate the real part of any complex value with a single prime (f'), and the imaginary part with a double prime (f'').

Herein, the reciprocal lattice vectors H and G take all possible discrete values, including 0. The coefficients χ_{H-G} can be interpreted as being proportional to the probability amplitude of scattering a plane wave with wave vector k_G into another plane wave with the wave vector k_H, with a momentum transfer $H - G$. Scattering with a momentum transfer equal to a reciprocal lattice vector is nothing but Bragg scattering. Thus, the system of dynamical equations Eq. 2.2.11 describes plane wave amplitudes $\mathcal{D}_H$ which are mutually coupled by Bragg scattering.

The number of equations in this system is in principle very large. However, the coefficients χ_{H-G} are very small, and therefore only those components $\mathcal{D}_H$ are significant for which $\left| k_H^2 - K^2 \right|$ is also small, i.e. the *resonance condition* $|k_H| \approx K$ is valid.

2.2.1. Single beam case

In the single beam case the resonance condition is valid only for a single wave vector k_0. From Eq. 2.2.11 follows immediately $k_0 = K(1 + \chi_0/2)$, where

$$n(\lambda) = 1 + \frac{\chi_0}{2} = 1 + \delta(\lambda) + \mathrm{i}\,\beta(\lambda) \tag{2.2.12}$$

is the *complex index of refraction*. Since χ_0' is small and negative, the real part of the index of refraction $\delta(\lambda) < 1$. Thus, the magnitude k_0 of the crystal wave vector is smaller than the magnitude K of the vacuum wave vector, and the wavelength inside the crystal is respectively larger:

$$\lambda_{\mathrm{cryst.}} = \frac{\lambda}{1 + \frac{\chi_0}{2}} \approx \lambda \left(1 + r_e \frac{\lambda^2}{2\pi V} F_0' \right) \tag{2.2.13}$$

2.2.2. Two beam case

In the following, we will discuss the case of the resonance condition being fulfilled for two particular wave vectors k_0 and k_H.[a] The equation system Eq. 2.2.11 reduces then to a system of only two vector field amplitudes:

$$
\begin{aligned}
\frac{k_0^2 - K^2}{K^2}\,\mathcal{D}_0 &= \chi_0\,\mathcal{D}_0 + \chi_{\overline{H}}\,\mathcal{D}_H \\
\frac{k_H^2 - K^2}{K^2}\,\mathcal{D}_H &= \chi_H\,\mathcal{D}_0 + \chi_0\,\mathcal{D}_H
\end{aligned}
\tag{2.2.14}
$$

The incident wave is diffracted from the atomic planes of the crystal which are perpendicular to the reciprocal lattice vector H. The in-crystal vectors k_0 of the incident wave and k_H of the diffracted wave are associated with the vacuum wave vectors K_0 and K_H, respectively. The vectors K_0 and K_H define the scattering plane (K_0, K_H). The glancing angle of incidence between the wave vector K_0 and the reflecting atomic planes is θ. The incidence angle $\delta\theta = \pi/2 - \theta$

---

[a] Herein, H is a specific index, rather than a running index as in the discussions before.

is a measure of the deviation from normal incidence to the reflecting atomic planes. We also introduce the unit vector $\hat{z}$ being the internal normal to the front crystal surface.

The in-crystal wave vectors differ from the vacuum vave vectors because of the crystal susceptibility. Since the tangential component of the electric field is continuous at the crystal surface, we have $k_0 = K_0 + \delta \cdot \hat{z}$, i.e. the wave vectors differ only in their components parallel to the normal of the surface (similar for the diffracted wave). In the subsequent discussion we apply these conditions in the following form:

$$
\begin{aligned}
k_0 &= K_0 + \frac{\epsilon_0 K}{\gamma_0} \hat{z} \\
k_H &= K_H + \frac{\epsilon_H K}{\gamma_H} \hat{z}.
\end{aligned}
\tag{2.2.15}
$$

Herein, the corrections ϵ_0 and ϵ_H are unknowns which have to be determined along with $\mathcal{D}_0$ and $\mathcal{D}_H$, while γ_0 and γ_H are defined by the scattering geometry: $\gamma_0 = K_0 \cdot \hat{z}/K$ and $\gamma_H = (K_0 - H) \cdot \hat{z}/K$ are cosines between the surface normal $\hat{z}$ and the wave vectors K_0 and $K_0 + H$, respectively. With the angle η between the crystal surface and the reflecting atomic planes, one can also obtain the expressions $\gamma_0 = \sin(\theta - \eta)$ and $\gamma_H = -\sin(\theta + \eta)$.

The corrections ϵ_0 and ϵ_H are dependent: Using the momentum conservation Eq. 2.2.10 in crystals, one can obtain

$$
K_H = K_0 + H \left(\frac{\epsilon_0}{\gamma_0} - \frac{\epsilon_H}{\gamma_H} \right) \hat{z}.
\tag{2.2.16}
$$

Furthermore, we assume an isotropic vacuum and elastic Bragg scattering, i.e. the magnitudes of the incident and the diffracted wave should be equal:

$$
|K_H|^2 = |K_0|^2 = K^2.
\tag{2.2.17}
$$

Both equations lead to the following relation:

$$
\epsilon_H = \frac{\epsilon_0}{b} + \frac{\alpha}{2}
\tag{2.2.18}
$$

with

$$
\alpha = \frac{2 K_0 \cdot H + H^2}{K^2}
\tag{2.2.19}
$$

and

$$
b = \frac{\gamma_0}{\gamma_H} = -\frac{\sin(\theta - \eta)}{\sin(\theta + \eta)}.
\tag{2.2.20}
$$

As a result we obtain the wave vector of the diffracted wave in vacuum

$$
K_H = K_0 + H' \quad \text{with} \quad H' = H - K \frac{\alpha}{2 \gamma_H} \hat{z}.
\tag{2.2.21}
$$

Thus, the momentum transfer H' for the diffracted wave in vacuum is different from the momentum transfer H in the crystal, cf. Eq. 2.2.10, and if $H \nparallel \hat{z}$

then also $H \nparallel H'$. This can be interpreted as if the crystal is reflecting from virtual planes perpendicular to H' rather than from real atomic planes perpendicular to H. Using Eq. 2.2.21 one can express the angle Ψ between the virtual and the real reflecting atomic planes as a function of α:

$$\Psi = \frac{K \, |\alpha|}{2 \, H \, |\gamma_H|} \, \sin \eta. \tag{2.2.22}$$

The parameter α from Eq. 2.2.19 will turn out to be important since it is possible to express the reflectivity and transmissivity of the crystal as functions of only this one parameter.

   The parameter b characterizes how far the wave vectors of the incident and reflected radiation deviate from being symmetric to the normal on the crystal surface. It is therefore referred to as the *asymmetry parameter*.

   Subsequently, we will discuss the Bragg-case of the scattering geometry, where the incident and the reflected wave are on the same side of the vacuum-crystal interface. In this case, $\gamma_0 > 0$ and $\gamma_H < 0$, thus $b < 0$. If the angles of both the incident and the diffracted wave vector with the normal to the crystal surface are equal, which is always the case for exact backscattering ($\theta = \pi/2$), then $b = -1$.

   Combining the previous equations with Eq. 2.2.14, neglecting terms quadratic in ϵ_0 and ϵ_H, one obtains:

$$\begin{aligned}
2 \, \epsilon_0 \, \mathcal{D}_0^s &= \chi_0 \quad \mathcal{D}_0^s \;\; + \;\; \chi_{\overline{H}} \, C^s \, \mathcal{D}_H^s \\[2mm]
\left(\frac{2 \, \epsilon_0}{b} + a \right) \mathcal{D}_H^s &= \chi_H \, C^s \, \mathcal{D}_0^s \;\; + \;\; \chi_0 \quad \mathcal{D}_H^s
\end{aligned} \tag{2.2.23}$$

Herein, $\mathcal{D}_F^s$ with $s = \{\pi, \sigma\}$ and $F = \{0, H\}$ are the linearly polarized components of the electric vector $\mathcal{D}_F = e_F^\pi \mathcal{D}_F^\pi + e_F^\sigma \mathcal{D}_F^\sigma$. The π polarization unit vector e_F^π lies in the scattering plane, while the σ polarization unit vector e_F^σ is perpendicular to that plane. The polarization factors are $C^\pi = \cos 2\theta$ and $C^\sigma = 1$. In the special case of backscattering there is also $|\cos 2\theta| \approx 1$. Therefore, in the subsequent discussion the different polarization components are ignored, and the polarization index s is omitted.

   The compatibility condition for Eq. 2.2.23 determines two possible values for ϵ_0:

$$2 \, \epsilon_{0(\nu)} - \chi_0 = \sqrt{C^2 \, |b| \, \chi_H \chi_{\overline{H}}} \left(-y \pm \sqrt{y^2 - 1} \right), \quad \text{with} \quad \nu = 1, 2 \tag{2.2.24}$$

and

$$y = \frac{\chi_0 \, (1 - b) + \alpha \, b}{2\sqrt{C^2 \, |b| \, \chi_H \chi_{\overline{H}}}}. \tag{2.2.25}$$

2.2.3. Wave fields in a crystal and in vacuum

In the following, we will discuss the two-beam case for wave fields inside a crystal of the thickness d and in vacuum with incidence only on the front surface of the crystal.

Because of the two solutions for ϵ_0 in Eq. 2.2.24, the Bloch wave expression Eq. 2.2.9 inside the crystal reads

$$\mathcal{D}(\boldsymbol{r}) = e^{i\,K_0 \cdot \boldsymbol{r}} \left(\mathcal{D}_0(z) + \mathcal{D}_H(z)\, e^{i\,H \cdot \boldsymbol{r}} \right), \tag{2.2.26}$$

with

$$\mathcal{D}_0(z) = \sum_{\nu=1,2} e^{i\,\delta_\nu z}\, \mathcal{D}_{0(\nu)}, \quad \mathcal{D}_H(z) = \sum_{\nu=1,2} e^{i\,\delta_\nu z}\, \mathcal{D}_{H(\nu)}, \quad \delta_\nu = \frac{K}{\gamma_0}\,\epsilon_{0(\nu)}. \tag{2.2.27}$$

From Eq. 2.2.23 one can determine the ratio of the amplitudes as

$$R_\nu = \frac{\mathcal{D}_{H(\nu)}}{\mathcal{D}_{0(\nu)}} = \frac{2\,\epsilon_{0(\nu)} - \chi_0}{C\,\chi_{\overline{H}}}. \tag{2.2.28}$$

The amplitudes themselves have to be determined by the boundary condition that $\mathcal{E}$ on the vacuum side and $\mathcal{D}$ inside the crystal are equal.

For the incident beam, propagating in forward direction, the boundary condition at the front surface $\boldsymbol{r} = \boldsymbol{r_1}$ is

$$\mathcal{E}_0^{(\text{in})}\, e^{i\,K_0 \cdot \boldsymbol{r_1}} = \mathcal{D}_0(z_1)\, e^{i\,K_0 \cdot \boldsymbol{r_1}}. \tag{2.2.29}$$

Since there is no incident beam on the rear surface, the the boundary condition for the in-crystal reflected beam at the rear surface $\boldsymbol{r} = \boldsymbol{r_2}$ is

$$\mathcal{D}_H(z_2)\, e^{i\,(K_0 + H) \cdot \boldsymbol{r_2}} = 0. \tag{2.2.30}$$

With Eq. 2.2.27 one can rewrite these conditions as

$$\begin{array}{rcl} \mathcal{D}_{0(1)}\, e^{i\,\delta_1 z_1} & + & \mathcal{D}_{0(2)}\, e^{i\,\delta_2 z_1} = \mathcal{E}_0^{(\text{in})} \\ \mathcal{D}_{H(1)}\, e^{i\,\delta_1 z_2} & + & \mathcal{D}_{H(2)}\, e^{i\,\delta_2 z_2} = 0. \end{array} \tag{2.2.31}$$

This leads to the following result for the forward $\mathcal{D}_0(z)$ and Bragg-scattered $\mathcal{D}_H(z)$ components of the radiation field inside the crystal at a depth z:

$$\begin{aligned} \mathcal{D}_0(z) &= \mathcal{E}_0^{(\text{in})}\, \frac{R_1\, e^{i\,\delta_2(z-z_2)} - R_2\, e^{i\,\delta_1(z-z_2)}}{R_1\, e^{i\,\delta_2(z_1-z_2)} - R_2\, e^{i\,\delta_1(z_1-z_2)}} \\[2ex] \mathcal{D}_H(z) &= \mathcal{E}_0^{(\text{in})}\, \frac{R_1 R_2 \left(e^{i\,\delta_2(z-z_2)} - e^{i\,\delta_1(z-z_2)} \right)}{R_1\, e^{i\,\delta_2(z_1-z_2)} - R_2\, e^{i\,\delta_1(z_1-z_2)}} \end{aligned} \tag{2.2.32}$$

We will now develop some general expressions for the transmission and reflection amplitudes of the system. From Eqs. 2.2.26, 2.2.32, the forward and

reflected components of the radiation field at the rear and front surfaces can be expressed as

$$
\begin{aligned}
\mathcal{D}(\boldsymbol{r_2})_{\text{forward}} &= \mathcal{E}_0^{(\text{in})}\, t_{00}\; e^{\,i\,\boldsymbol{K}_0 \cdot \boldsymbol{r}_2} \\[2mm]
\mathcal{D}(\boldsymbol{r_1})_{\text{reflected}} &= \mathcal{E}_0^{(\text{in})}\, r_{0H}\, e^{\,i\,(\boldsymbol{K}_0 + \boldsymbol{H}) \cdot \boldsymbol{r}_2}.
\end{aligned}
\tag{2.2.33}
$$

Herein,

$$
\begin{aligned}
t_{00} &= e^{\,i\,\delta_1 d}\; \frac{R_2 - R_1}{R_2 - R_1\, e^{\,i\,(\delta_1 - \delta_2)\,d}} \\[2mm]
r_{0H} &= R_1 R_2\; \frac{1 - e^{\,i\,(\delta_1 - \delta_2)\,d}}{R_2 - R_1\, e^{\,i\,(\delta_1 - \delta_2)\,d}}
\end{aligned}
\tag{2.2.34}
$$

are the transmission and reflection amplitudes, measured at the rear and front surfaces, respectively. They are obtained from Eqs. 2.2.32, 2.2.33 with the crystal thickness $d = z_2 - z_1$.

Because of the continuity of the wave fields at the crystal surfaces, we have the following expressions for the transmitted and reflected wave fields at any arbitrary point $\boldsymbol{r}$ in vacuum:

$$
\begin{aligned}
\mathcal{E}_0(\boldsymbol{r}) &= \mathcal{D}(\boldsymbol{r_2})_{\text{forward}}\; e^{\,i\,\boldsymbol{K}_0 \cdot (\boldsymbol{r} - \boldsymbol{r}_2)} \\[2mm]
\mathcal{E}_H(\boldsymbol{r}) &= \mathcal{D}(\boldsymbol{r_1})_{\text{reflected}}\; e^{\,i\,\boldsymbol{K}_H \cdot (\boldsymbol{r} - \boldsymbol{r}_1)}.
\end{aligned}
\tag{2.2.35}
$$

From Eqs. 2.2.33, 2.2.21 one can calculate the wave fields in vacuum as follows:

$$
\begin{aligned}
\mathcal{E}_0(\boldsymbol{r}) &= \mathcal{E}_0^{(\text{in})}\, t_{00}\; e^{\,i\,\boldsymbol{K}_0 \cdot \boldsymbol{r}} \\[2mm]
\mathcal{E}_H(\boldsymbol{r}) &= \mathcal{E}_0^{(\text{in})}\, \rho_{0H}\, e^{\,i\,\boldsymbol{K}_H \cdot \boldsymbol{r}},
\end{aligned}
\tag{2.2.36}
$$

with the reflection amplitude in vacuum at the front crystal side

$$
\rho_{0H} = r_{0H}\, e^{\,i\,\frac{K z_1}{2 \gamma_H}\alpha}.
\tag{2.2.37}
$$

The transmission amplitudes at the crystal surface and in vacuum are equal.

2.2.4.   Reflectivity of thick crystals

The *reflectivity R* of a crystal is defined as the ratio between the fluxes of the incident and the reflected beam. As follows from Eqs. 2.2.36, 2.2.37, using the asymmetry parameter b, Eq. 2.2.20, it is given by

$$
R = \frac{1}{|b|}\, |r_{0H}|^2.
\tag{2.2.38}
$$

We will now discuss the case of a *thick crystal* with $d \gg d_{\text{e}}$, i.e. the crystal thickness d is much larger than $d_{\text{e}} = \text{Im}\,(\delta_1 - \delta_2)^{-1}$, or

$$
d_{\text{e}}(y) = \text{Im}\, \frac{\gamma_0}{K \sqrt{C^2\, |b|\, \chi_H \chi_{\overline{H}}}}\, \frac{1}{\sqrt{y^2 - 1}}.
\tag{2.2.39}
$$

From Eq. 2.2.34 follows that for a thick crystal the reflection amplitude does not depend on the thickness d, but can be approximated by $r_{0H} = R_1$. In this case, the reflectivity becomes $R = |R_1|^2 / |b|$. By using Eqs. 2.2.24 and 2.2.28 additionally, we can find the following well-known expression for the reflectivity of a semi-infinite crystal:

$$R = \left| \frac{\chi_H}{\chi_{\overline{H}}} \right| \left| -y \pm \sqrt{y^2 - 1} \right|^2 , \qquad (2.2.40)$$

which is a function of the parameter y alone. Furthermore, we assume vanishing photo-absorption, i.e. $\chi_0'' \approx 0$ and $\chi_H'' \approx 0$. In this case there is a region of total reflection with $R = 1$, given by the condition $-1 \leq y \leq 1$. We also assume $\chi_H = \chi_{\overline{H}}$ which is true for centrosymmetric crystals. With the notation $y = \cos \phi_r$, the reflection amplitude reads

$$r_{0H} = -\sqrt{|b|} \, e^{-i\,\phi_r}. \qquad (2.2.41)$$

As y varies from -1 to 1 in the region of total reflection, the phase jump ϕ_r changes from $-\pi$ to 0.

Using Eq. 2.2.25, one can also express the region of total reflection in terms of the parameter α:

$$\alpha_{-1} \leq \alpha \leq \alpha_{+1}$$

$$\alpha_{\pm 1} = \alpha_c \pm \frac{2\,|C\chi_H|}{\sqrt{|b|}} \qquad (2.2.42)$$

$$\alpha_c = \chi_0' \left(1 - \frac{1}{b} \right).$$

Herein, the region of total reflection is centered at a_c, and its width is

$$\Delta\alpha = \alpha_{+1} - \alpha_{-1} = \frac{4\,|C\,\chi_H|}{\sqrt{|b|}}. \qquad (2.2.43)$$

The order of magnitude of χ_H is typically $\leq 10^{-5}$ for x-rays with energy $E \approx 15\,\text{keV}$.

Thus, even tiny variations of α, and consequently E, θ, or the crystal temperature T, will result in large changes in reflectivity. Such small variations leave the components of the electric susceptibility χ_0, χ_H, the asymmetry parameter b, and the polarisation factor C—which constitute the parameter y, cf. Eq. 2.2.25—practically unchanged. Therefore, it should be possible to express the reflectivity as a function of the universal parameter α. If both $R(\alpha)$ and the relation $\alpha = f(\theta, E, T)$ are known, then one can obtain immediately the reflectivity as a function of the glancing angle of incidence θ, the photon energy E, and the crystal temperature T. The relation $\alpha = f(\theta, E, T)$ will be derived in the following section.

2.2.5.   Parameter of deviation from Bragg's condition

In the following, different representations and the physical interpretation of the parameter α will be discussed.

For $\alpha = 0$, Eq. 2.2.19 reads:

$$2\,\boldsymbol{K_0} \cdot \boldsymbol{H} + \boldsymbol{H}^2 = 0. \tag{2.2.44}$$

For geometrical reasons $\boldsymbol{K_0} \cdot \boldsymbol{H} = -HK\sin\theta$, and from Eq. 2.2.8 follows $H = 2\pi/d_H$. This leads to

$$\lambda = 2\,d_H\,\sin\theta_B, \tag{2.2.45}$$

which is very well known as *Bragg's law*. In the kinematical theory of Bragg diffraction (cf. James, 1950) where no multiple scattering effects are taken into account, Bragg's law relates the radiation wavelength λ to the *Bragg angle* θ_B, i.e. the glancing angle of incidence at which the radiation is reflected from the atomic planes.

It is also possible to write Bragg's law in terms of the photon energy E:

$$E_H = E\,\sin\theta_B \tag{2.2.46}$$

with the *Bragg energy*

$$E_H = \frac{1}{2}\,H\,\hbar c = \frac{hc}{2d_H}. \tag{2.2.47}$$

In the kinematical theory, x-rays with energy E_H are reflected exactly backwards.

The picture of diffraction in crystals provided by the kinematical theory is, however, only simplified. As will be shown later, the dynamical theory will give a slightly different relation between the glancing angle of incidence and the radiation wavelength than Bragg's law.

The parameter α can be interpreted as a measure for the deviation from Bragg's condition as long as Bragg's law is fulfilled when $\alpha = 0$.

In the following discussion we will derive the relations between the parameter α and the physical parameters of the problem, i.e. the energy E or wavelength λ of the incident plane wave, the glancing angle of incidence θ, and the temperature T of the crystal. From the definition of α, Eq. 2.2.19, and the fact that incident and reflected wave build the same angle with the atomic planes, one obtains directly

$$\alpha = \frac{-2\,H\,K\sin\theta + H^2}{K^2} \tag{2.2.48}$$

Next, we insert the definition of the Bragg energy Eq. 2.2.47, under the assumption that the interplanar distance is temperature dependent, and obtain the following relation:

$$\alpha = 4\,\frac{E_H(T)}{E}\left(\frac{E_H(T)}{E} - \sin\theta\right), \tag{2.2.49}$$

which is valid for any glancing angle of incidence, including $\theta = \pi/2$. This is the required general dependence $\alpha = f(E, \theta, T)$ for any given Bragg energy E_H. It is also possible to express α as a function of the x-ray wavelength:

$$\alpha = \frac{2\lambda}{d_H(T)} \left(\frac{\lambda}{2\,d_H(T)} - \sin\theta \right). \tag{2.2.50}$$

With Bragg's law Eq. 2.2.45 one can also express α by angles:

$$\alpha = 4 \sin\theta_B \left(\sin\theta_B - \sin\theta \right) \tag{2.2.51}$$

These are exact expressions which were given by Shvyd'ko and Gerdau (1999). In other texts about the dynamical theory, like Batterman and Cole (1964); Pinsker (1978); Zachariasen (1945) and others, the approximation

$$\alpha = 2(\theta_B - \theta) \sin 2\theta_B \tag{2.2.52}$$

is used, which is valid for $|\theta_B - \theta| \ll 1$, but fails in the region of backscattering $\theta_B = \pi/2$. Caticha and Caticha-Ellis (1982) have shown that another approximation

$$\alpha = 2 \left(\delta\theta^2 - 2\epsilon \right), \tag{2.2.53}$$

with $\delta\theta = \theta_B - \theta$ and $\epsilon = (E - E_H)/E_H$, is applicable for backscattering. It can be derived from Eq. 2.2.49 under the assumptions $\delta\theta \ll 1$ and $\epsilon \ll 1$.

We will now take into account the temperature dependence of the Bragg energy, which can be expressed in a small temperature range as

$$E_H(T + \delta T) = E_H(T) \left(1 - \rho_H(T)\,\delta T \right) \tag{2.2.54}$$

with the linear temperature expansion coefficient[a] in the direction of H

$$\rho_H(T) = \frac{1}{d_H(T)} \left. \frac{\mathrm{d}d_H}{\mathrm{d}T} \right|_T. \tag{2.2.55}$$

This allows the generalization of Eq. 2.2.53 as follows:

$$\alpha = 2\,\delta\theta^2 - 4 \left(\frac{\delta E(T)}{E_H(T)} + \rho_H(T)\delta\theta \right) \tag{2.2.56}$$

with $\delta E(T) = E - E_H(T)$. This equation shows the important fact that in the backscattering region α varies linearly both with the x-ray energy and the crystal temperature, and quadratically with the angular deviation.

From Eq. 2.2.56 one can show the equivalence of variations of x-ray energy and temperature: Those values of E and T are considered equivalent which result in the same reflectivity, and if the reflectivity is solely a function of α, the equivalence relation reads:

$$\delta E = E_H(T)\,\rho_H(T)\,\delta T. \tag{2.2.57}$$

---

[a]The linear temperature expansion coefficient is denoted with the letter ρ througout this thesis, to avoid confusion with the parameter α from Eq. 2.2.19

2.2.6. Center of the region of total reflection

With Eq. 2.2.50, which is valid for any glancing angle of incidence and photon energy, it is possible to rewrite the expression for the center of total reflection from Eq. 2.2.42 as follows:

$$\frac{2\,\lambda_c}{d_H}\left(\frac{\lambda_c}{2\,d_H} - \sin\theta_c\right) = \chi_0'\left(1 - \frac{1}{b}\right). \tag{2.2.58}$$

Using Eq. 2.2.4, this can be written as

$$2\,d_H\,\sin\theta_c = \lambda_c(1 + w_H) \tag{2.2.59}$$

with

$$w_H = -\chi_0'\,\frac{d_H^2}{\lambda^2}\left(1 - \frac{1}{b}\right) = r_e\,\frac{d_H^2}{\pi V}\,F_0'\left(1 - \frac{1}{b}\right). \tag{2.2.60}$$

Similarly, the expression for the center of total reflection on the energy scale reads:

$$E_c\,\sin\theta_c = E_c(1 + w_H). \tag{2.2.61}$$

Equation 2.2.59 looks similar to Bragg's law Eq. 2.2.45, but differs by a small, yet significant correction w_H which is typically $10^{-4}\ldots10^{-6}$. Since $w_H > 0$, the peak of reflectivity is shifted to higher wavelengths or energies than given by Bragg's law. The relations Eqs. 2.2.59, 2.2.61 are often referred to as the *dynamical Bragg's law*. It is valid in the whole range of glancing angles, without division into standard and backscattering regimes.

For a given Bragg reflection, the correction w_H is almost constant in a relatively large spectral range, since the only energy dependence arises from the anomalous scattering correction $f'(\lambda)$ in F_0, cf. Eqs. 2.2.5, 2.2.6. E.g., for the spectral range $\lambda_M - 0.01\,\text{Å} \le \lambda_c \le \lambda_M + 0.01\,\text{Å}$, where $\lambda_M = 0.86\,\text{Å}$ is approximately the wavelength of the Mössbauer radiation of ^{57}Fe, the anomalous scattering correction for silicon varies by no more than ±0.003 around its average value of 0.119 (Deutsch and Hart, 1988, cf.). Thus, the variation of w_H is less than 10^{-8}, compared to the leading term 1.

The difference between Bragg angle and center of total reflection according to the dynamical Bragg's law is

$$\sin\theta_B - \sin\lambda_c = w_H\,\frac{\lambda_c}{2\,d_H}. \tag{2.2.62}$$

Also the wavelength reflected at the center of total reflection deviates from the wavelength given by Bragg's law according to

$$\lambda_c = \frac{1}{1 + w_H}. \tag{2.2.63}$$

Thus, the wavelength determined by the dynamical theory is always smaller than the wavelength determined by Bragg's law. However, by virtue of Eq. 2.2.13, the wavelength inside the crystal is larger than in vacuum. The corrections in Eqs. 2.2.13, 2.2.63 look similar but are not equal, since there is no λ^2 dependence in w_H. Only under the exact backscattering condition, where $\lambda = d_H$ and $b = -1$, these corrections are equal.

2.2.7. Spectral width of the region of total reflection

The spectral width of the Bragg reflection is defined as

$$\epsilon_H = \frac{\Delta\lambda}{\lambda} = \frac{\Delta E}{E}. \qquad (2.2.64)$$

Using Eqs. 2.2.43 and 2.2.50, one obtains

$$\epsilon_H = \frac{\Delta\alpha}{4\sin^2\theta} = \frac{|C\chi_H|}{\sin^2\theta\sqrt{|b|}}, \qquad (2.2.65)$$

which is valid for all glancing angles of incidence except $\theta = 0$. Since $\chi_H \propto \lambda^2$, cf. Eq. 2.2.4, we have $\epsilon_H \propto \lambda^2/\sin^2\theta = (2d_H)^2 = \text{const.}$, i.e. the relative spectral width is constant independent of the glancing angle of incidence. The Debye-Waller-factor and the atomic scattering amplitude, which are parts of of χ_H, have the same $\lambda/\sin\theta$ dependence, and are therefore also constant for a given reflection.

By use of Eq. 2.2.39 one can now express the extinction length at the center of total reflection as

$$d_e(0) = \frac{\gamma_0}{K\,|C\chi_H|\,\sqrt{|b|}}. \qquad (2.2.66)$$

Assuming the symmetric diffraction geometry, $b = -1$, the combination of Eqs. 2.2.65 and 2.2.66 leads to

$$\epsilon_H = \frac{d_H}{\pi\,d_e(0)} = \frac{1}{\pi\,N^*}, \qquad (2.2.67)$$

with $N^* = d_e(0)/d_H$ the number of reflecting planes within the extinction length. Thus the spectral width is reciprocal to the effective number of reflecting planes contributing to diffraction. Since the extinction length increases with higher x-ray energy, the relative spectral width becomes smaller, respectively.

Extinction lengths of $d_e(0) \approx 10\ldots100\,\mu\text{m}$ are typical for x-rays with $E \approx 14\,\text{keV}$, or $\lambda \approx 100\,\text{pm}$. Thus, a relative energy resolution of about $10^{-6}\ldots10^{-7}$, corresponding to an energy width of about $10\ldots1\,\text{meV}$, is achievable with single Bragg reflections in this energy range.[a]

The fact that the relative spectral width of a given Bragg reflection is constant implies that the absolute value of the spectral width, in terms of energy units, is smallest for the lowest possible photon energy, which occurs at normal incidence.

---

[a]It is possible to achieve higher energy resolution by use of asymmetric Bragg reflections, see e.g. Toellner (2000) and references therein.

2.2.8. Angular width of the region of total reflection

Since there is no simple expression for the angular width of the region of total reflection which is valid for the whole range of glancing angles, we will discuss the cases $\theta < \pi/2$ and $\theta \approx \pi/2$ separately. For $\theta < \pi/2$, the approximation Eq. 2.2.52 is valid, which leads to

$$\Delta\theta = \frac{\Delta\alpha}{2\,\sin(2\theta)} = \frac{2\,|C\,\chi_H|}{\sin(2\theta)\,\sqrt{|b|}}. \tag{2.2.68}$$

Since $\chi_H \propto \lambda^2$ and $\sin\theta/\lambda = \text{const.}$ one can deduce from Eq. 2.2.68 that the angular acceptance $\Delta\theta$ increases as $\tan\theta$ with increasing glancing angle of incidence θ.

In the backscattering region, however, the expression Eq. 2.2.53 should be used. At the x-ray energy $E = E_H(1 - \alpha_c/4) = 2\sqrt{|C\,\chi_H|}$, the center of the angular region of total reflection is exactly at $\delta\theta = 0$, and its width is

$$\Delta\theta = \sqrt{\Delta\alpha} = 2\sqrt{|C\,\chi_H|}. \tag{2.2.69}$$

Distinct from Eq. 2.2.68, the angular width at exact backscattering is proportional to the square root of $|C\,\chi_H|$. The reason for this is the quadratic angular dependence of λ near $\delta\theta \approx 0$. Taking into account that $|\chi_H| \lesssim 10^{-5}$, this implies a drastical increase of the angular width in backscattering geometry. By using Eq. 2.2.65 one can rewrite Eq. 2.2.69 as

$$\Delta\theta = 2\sqrt{\epsilon_H}, \tag{2.2.70}$$

which is valid for near-normal incidence to the reflecting planes.

This relation is one of the most important features of Bragg backscattering: The angular acceptance scales with the square root of the relative spectral width! This implies that, e.g., Bragg reflections with a relative spectral width as narrow as $\epsilon_H = 10^{-9}$ are still not blurred by an x-ray beam with a divergence of about $60\,\mu\text{rad}$.

2.3. Multiple beam diffraction

In exact backscattering geometry, it is possible that Bragg scattering does not only occur for the single diffraction vector $\boldsymbol{H}$ which satisfies the condition $\boldsymbol{K_0} = -\boldsymbol{H}/2$. If there is another diffraction vector $\boldsymbol{G}$ which fulfills Bragg's law in vector form $2\,\boldsymbol{K_0}\cdot\boldsymbol{G} + \boldsymbol{G}^2 = 0$, both diffraction vectors are related by

$$\boldsymbol{G}\cdot\boldsymbol{H} = \boldsymbol{G}^2. \tag{2.3.1}$$

in the kinematical approximation. From $(\boldsymbol{H}-\boldsymbol{G})\cdot\boldsymbol{G} = \boldsymbol{G}\cdot\boldsymbol{H} - \boldsymbol{G}^2 = 0$ follows that the vectors $\boldsymbol{H}$, $\boldsymbol{G}$, and $\boldsymbol{H}-\boldsymbol{G}$ compose a triangle with a right angle between the vectors $\boldsymbol{G}$ and $\boldsymbol{H}-\boldsymbol{G}$. Furthermore, with $\boldsymbol{F} = \boldsymbol{H}-\boldsymbol{G}$, a similar relation $\boldsymbol{F}\cdot\boldsymbol{H} = \boldsymbol{F}^2$ is valid. Thus, if a reflection fulfilling Eq. 2.3.1 exists, it is always accompanied by another reflection with the diffraction vector

$$\boldsymbol{F} = \boldsymbol{H} - \boldsymbol{G}. \tag{2.3.2}$$

The reflections described by **G** and **F** build a *conjugate pair* of reflections. The fact that **H**, **G**, and **F** compose a right-angle triangle implies that such *parasitic reflections* appear systematically in rectangular reciprocal lattices. They can also appear in non-rectangular reciprocal lattices when there is a rectangular sub-lattice.

Steyerl and Steinhauser (1979) have pointed out originally that in crystals with diamond structure, like Si, parasitic reflections occur for all allowed orders of reflection. There are only two reflections not affected by multiple beam diffraction: (1 1 1) and (2 2 0). As discussed by Sutter (2000), e.g., the (12 4 0) exact back-reflection in Si is accompanied by 22 other reflections. Together with the incident and the back-reflected beam, this is referred to as a 24-beam case. Due to the many new reflection channels opening up at normal incidence, one expects a strongly reduced reflectivity in the backscattering channel, and also a complicated energy dependence. Therefore, Si is, in general, not suitable for diffraction experiments in the exact backscattering geometry.[a]

However, in the experiment for the measurement of the wavelength of the Mössbauer radiation of ^{57}Fe, we have no other choice but using backscattering from Si, since the lattice spacing of Si is the underlying length standard.

The (12 4 0) reflection of Si is used in the experiment for the determination of the wavelength of the Mössbauer radiation of ^{57}Fe, together with (9 7 5), also a 24-beam case, and (9 1 1), a 6-beam case. These reflections were chosen because their Bragg energy (Eq. 2.2.47) is close to the Mössbauer radiation wavelength of ^{57}Fe to be measured. The relative spectral width of these reflections is $\simeq 3 \times 10^{-7}$, which leads according to Eq. 2.2.70 to an angular width of about 1 mrad. The angular region where multiple beam diffraction has a considerable impact is in most cases narrower than 100 µrad (Sutter, 2000). It is therefore possible to use Si in a near-backscattering geometry where the multiple beam diffraction almost vanishes while the the advantages of backscattering are still in effect.

The offset from exact backscattering is described by the deviation $\delta\theta$ of the incident wave vector from the reciprocal lattice vector of the back-reflection, and by the azimuthal angle ϕ measured counterclockwise from the [0 0 1] direction. Sutter (2000, 2001) has shown that for certain values ϕ_{mult}, which are given in Tab. 2.3.1, some of the parasitic reflections are still excited if $\delta\theta$ extends over a range of some mrad, even outside the angular width of the back-reflection. This implies that by setting $\delta\theta$ to some small amount off exact backscattering, one has still a case of multiple beam diffraction if ϕ is set to one of the ϕ_{mult} values. Therefore, the cases with $\phi = \phi_{\mathrm{mult}}$ have to be avoided if one wants to get rid of the abovementioned disadvantages of multiple beam

---

[a] Another reason why Si, or other materials with a cubic symmetry, are disadvantageous for Bragg backscattering, is that the Bragg energies in such a structure are highly degenerate. With the interplanar distance $d_H = a(h^2 + k^2 + l^2)^{-1/2}$ it is easy to see that there are many reflections with different Miller indices h, k, l but the same interplanar distance d_H. Thus, the number of distinct Bragg energies is rather low. Typically, in the energy range $10 \ldots 25$ keV there is only one Bragg energy per $\simeq 500 \ldots 250$ eV interval. Therefore it becomes impossible to shift the Bragg energy to any given value by changing the temperature of the crystal. See Shvyd'ko (2004) for further discussion of this topic.

Back-reflection	ϕ_{mult} [°]	Parasitic Reflections	No. of beams
$(12\,4\,0)$	0.00	$(8\,\bar{4}\,0)$, $(4\,8\,0)$, $(8\,8\,0)$, $(4\,\bar{4}\,0)$, $(12\,0\,0)$, $(0\,4\,0)$	8
	19.36	$(6\,8\,2)$, $(6\,\bar{4}\,\bar{2})$	4
	46.50	$(12\,2\,\bar{2})$, $(0\,2\,2)$	4
	72.45	$(6\,4\,6)$, $(6\,0\,\bar{6})$	4
	83.98	$(8\,2\,\bar{6})$, $(4\,2\,6)$	4
	96.02	$(8\,2\,6)$, $(4\,2\,\bar{6})$	4
	107.55	$(6\,4\,\bar{6})$, $(6\,0\,6)$	4
	133.49	$(12\,2\,2)$, $(0\,2\,\bar{2})$	4
	160.64	$(6\,8\,\bar{2})$, $(6\,\bar{4}\,2)$	4
$(9\,9\,1)$	33.90	$(9\,5\,5)$, $(0\,4\,\bar{4})$	4
	146.10	$(4\,0\,\bar{4})$, $(5\,9\,5)$	4
$(9\,7\,5)$	0.00	$(8\,8\,0)$, $(1\,\bar{1}\,5)$	4
	21.26	$(7\,9\,1)$, $(2\,\bar{2}\,4)$	4
	87.70	$(3\,9\,5)$, $(6\,\bar{2}\,0)$	4
	102.30	$(2\,8\,6)$, $(7\,\bar{1}\,\bar{1})$	4
	107.12	$(10\,6\,4)$, $(\bar{1}\,1\,1)$	4
	111.48	$(10\,2\,0)$, $(\bar{1}\,5\,5)$	4
	113.01	$(9\,1\,\bar{1})$, $(0\,6\,6)$	4
	136.24	$(2\,0\,\bar{2})$, $(7\,7\,7)$	4
	147.77	$(3\,1\,\bar{3})$, $(6\,6\,8)$	4
	159.47	$(7\,5\,\bar{3})$, $(2\,2\,8)$	4
	161.00	$(8\,6\,\bar{2})$, $(1\,1\,7)$	4

Tab. 2.3.1: Azimuthal angles of the backscattering multiple-beam cases for the back-reflections used in the experiment for the determination of the wavelength of the Mössbauer radiation of ^{57}Fe. When $\phi = \phi_{mult}$, the angular width in $\Delta\theta$ of the mentioned parasitic reflections is larger than the angular width of the back-reflection.

diffraction. Preferable are values of ϕ which are in the center of large gaps between two ϕ_{mult} values.

The multiple beam diffraction in backscattering geometry is a highly encouraging field of science which deserves in-depth studies on its own. This is, however, far beyond the scope of the present work. The PhD Theses of Sutter (2000) and Lerche (2004) are good starting points for further reading.

We have, however, made a short demonstration how the setup for the measurement of the wavelength of the Mössbauer radiation of ^{57}Fe could also be used for studies on multiple beam diffraction—see Section 6.4.

Chapter 3

Temperature measurement and control

The setup for the measurement of the ratio between the lattice parameters of a Si or $\alpha-Al_2O_3$ single crystal and the wavelength of the Mössbauer radiation of ^{57}Fe was introduced in Chapter 1, and is shown in Figs. 1.0.2, 4.1.1, and 5.1.1. There are two components in this setup which require precise temperature measurement and control. These are the single crystal itself and the Si (7 7 7) channel-cut crystal which are both affected by thermal expansion. In this chapter we will first discuss the requirements on temperature accuracy and stability for the two crystals. Thereafter, we will describe in great detail the apparatus and the methods which were used to meet these requirements.

3.1. Requirements on temperature accuracy and stability

3.1.1. Temperature requirements for the backscattering crystal

The current state of precise measurements of the Si lattice parameter is discussed in detail by Bergamin et al. (1999). The overall uncertainty of the Si lattice parameter is reported there to be 2.2×10^{-8} and the thermal expansion at $22.5\,°C$ is $\rho = 2.581(2) \times 10^{-6}\,K^{-1}$.

Therefore, it is at first view desirable to know the crystal temperature well enough, and have it controlled precise enough, to keep the lattice parameters unchanged within $\Delta a/a = 2.2 \times 10^{-8}$ accuracy. Therefore, the temperature accuracy should be $\Delta T = \Delta a/(a\,\rho) \approx 8.5\,mK$.

3.1.2. Temperature requirements for the λ-meter crystal

The λ-meter is used in the experiments described in this thesis to measure wavelength differences. Its main component is a Si (7 7 7) channel-cut crystal which transmits a narrow energy band from the incoming synchrotron radiation beam. The wavelength of the transmitted radiation λ_c is determined, according to Bragg's law Eq. 2.2.45, by the glancing angle of incidence θ_c to the (7 7 7) reflecting planes in the Si crystal. It is changed by rotation of the Si crystal. The temperature of the Si crystal has to be kept stable during one *run* of the experiment, i.e. one sequence of measurements of the Bragg angles where the wavelength of the transmitted beam matches the wavelengths of Mössbauer radiation or back-reflections. It is however not required to keep the temperature accurately at a predefined temperature, since the interplanar distance of

PSfrag replacements
T [°C]
T [K]
R_{PT100} [Ω]
R_{Cernox} [Ω]
ΔT [K]

the Si (7 7 7) channel-cut crystal will be an experimental result together with the Mössbauer radiation wavelength of ^{57}Fe.

Furthermore one has to ensure that both faces of the channelcut have the same temperature, because otherwise the Bragg energy of the second reflection will not match the first one, resulting in loss of intensity.

At $T = 300\,$K, for the Mössbauer radiation of ^{57}Fe with an energy of 14.4125 keV, the glancing angle of incidence of the Si (7 7 7) reflection planes is 73.784847°, with an angular acceptance of 1.276 µrad. The change of the glancing angle of incidence with temperature is $\delta\theta/\delta T = -8.830\,$µrad K^{-1}.[a] This leads to a temperature width of 0.14 K; since the peak region is again much narrower than the bandpass one should assume $\Delta T \approx 15\,$mK as the requirement for temperature stability.

3.2. Temperature measurement setup

3.2.1. Oven
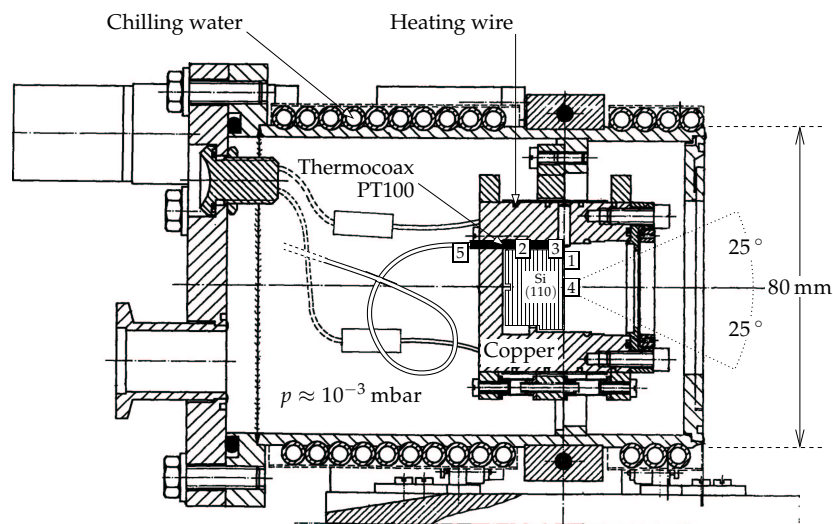
Fig. 3.2.1: Oven for high temperature stability and accuracy of backscattering crystals. The numbers in boxes denote different positions of additional thermocouples or PT100 sensors which are used to measure temperature gradients inside the oven.

For the measurements of the Mössbauer radiation wavelength of ^{57}Fe, and of the lattice parameters of $\alpha-\text{Al}_2\text{O}_3$ above room temperature, an oven designed for high temperature stability was deployed to keep the Si reference or $\alpha-\text{Al}_2\text{O}_3$ crystal under study. This oven has been constructed for previous experiments on exact Bragg backscattering of x-rays (Shvyd'ko et al., 1998), where temperature stability in the mK range is essential. It is shown in Fig. 3.2.1.

---

[a]These data are calculated with the `reflex` program from Yu.V. Shvyd'ko.

The oven is made of a cylindrical copper block with 4.2 cm outer diameter and about 1 cm wall thickness. A heating wire is winded on to the outer mantle surface of the cylinder. Due to the high thermal conductivity and capacity of copper, an even heat distribution inside the cylinder is ensured. On the inner surface a PT100[a] thermoresistor is installed which is used for temperature measurement and control, cf. Section 3.2.5 and Lucht (1998). At the open end of the cylinder a cap with a window is mounted. Different types of caps allow one to operate at different conditions. In experiments where the lattice parameters of the sample inside the oven are to be used as a length standard (cf. Chapter 4) or to be measured (cf. Chapter 5), it is preferable to keep the crystal in vacuum since then there is no need for pressure control. In such a case a cap with a narrow groove on one edge is used, so that the oven is evacuated together with the outer tank. To ensure a good temperature homogeneity and to avoid thermal radiation between the sample and the environment, some heat conductive compound must be applied between the cylinder and the cap. The window must also be made of some material with good thermal conductivity and good transmission for x-rays, like Aluminum.[b] In other experiments on exact backscattering a vacuum-sealed cap is preferred which ensures some air to remain in the oven when the outer tank is evacuated. The thermal conduction within the air will lead to a better temperature homogeneity inside the oven.

The oven is mounted in an evacuated tank for thermal insulation against the ambient temperature. Since the temperature control is working only by changing the heating power (see Section 3.2.5), it is necessary to keep a temperature gradient of at least some K between the tank and the oven. For a crystal temperature setpoint around room temperature, the tank is chilled with water flowing through a copper tube winded around the vacuum tank. For a higher temperature setpoint[c] the tank is chilled good enough just by the surrounding air.

3.2.2. Liquid Helium flow cryostat

For the measurements of the lattice parameters of $\alpha-Al_2O_3$ in the temperature range from 4.2 K to room temperature a custom-made LHe[d] flow cryostat was obtained from CryoVac[e]. It was specially constructed for this experiment. The main modifications from CryoVac's standard flow cryostats are extra large windows. They allow changing the angle of incidence of the beam on the mounted backscattering crystal by 30° in any direction from the cryo-

---

[a] Platinum Thermoresistor with nominal resistance $R = 100\,\Omega$ at $T = 0\,°C$

[b] The use of Beryllium windows was disapproved because this material imposes high risk of damage to health.

[c] For example, at $\approx 100\,°C$ which are used for exact backscattering of ^{57}Fe nuclear resonant quanta with the $(1\,3\,\overline{4}\,28)$ reflection of sapphire (Shvyd'ko et al., 1998).

[d] liquid helium

[e] CryoVac mbH & Co. KG, Heuserweg 14, 53842 Troisdorf, Germany

T [°C]
T [K]
R_{PT100} [Ω]
R_{Cernox} [Ω]
ΔT [K]
S(777)
$\frac{1}{2}$ Slit
^{57}Fe
APD Detector
Oven or cryostat
Si or $\alpha-$Al$_2$O$_3$ single crystal
[1 1 0]
[$h\,k\,l$]
X-rays ψ
2θ

Liquid helium

Helium gas

Vacuum

Cernox thermoresistors

$\alpha-$Al$_2$O$_3$

30°   30°   30°

80 mm
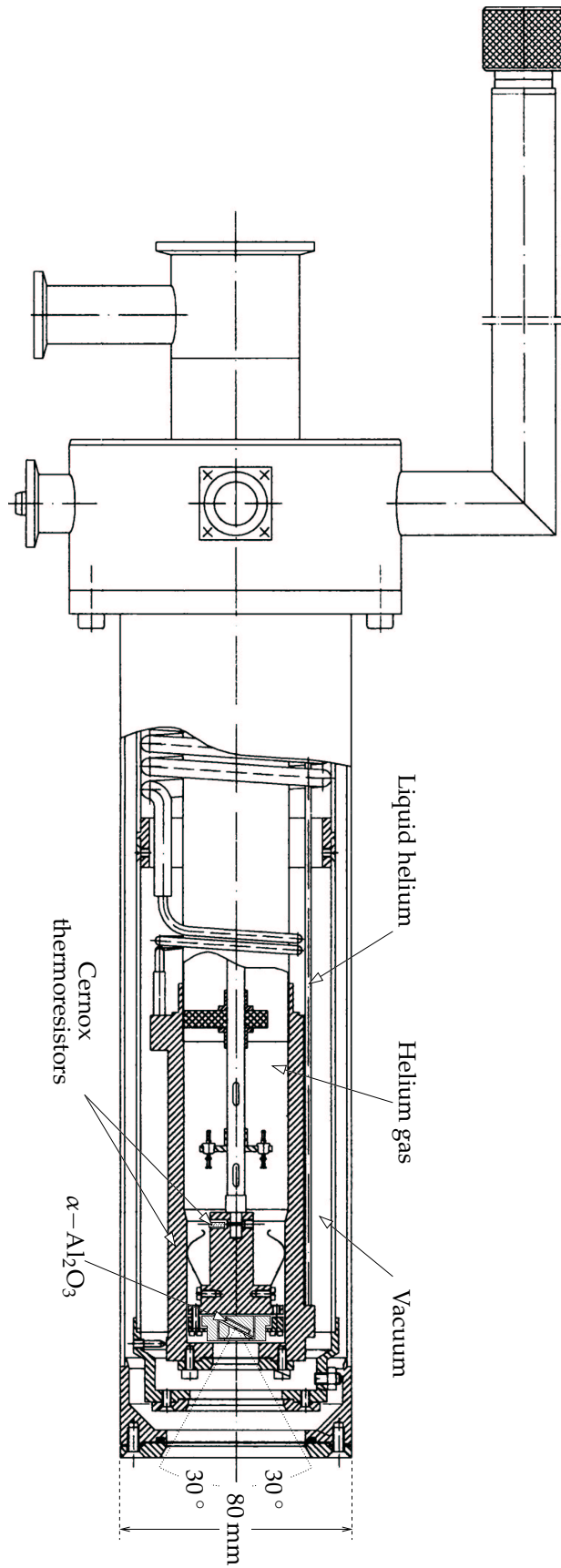
Fig. 3.2.2: *Liquid helium flow cryostat for backscattering from* $\alpha-$Al$_2$O$_3$ *at temperatures between 4.2 K and room temperature*

stat's axis (see Fig. 3.2.2[a)]) thus selecting different sets of lattice planes in the $\alpha-Al_2O_3$ crystal for exact backscattering.

Both the crystal holder and the heat exchanger at the inner shell of the cryostat are equipped with electric heating wires and Cernox temperature sensors which can be used for temperature measurement and control. The temperature can be controlled either by changeing the electric power applied on the heating wires (see Section 3.2.5) or the LHe flux in the heat exchanger; in practice it is best to use the LHe flux only for a rough temperature preset and do the fine control electrically.

PSfrag replacements

$T \quad [\,°C\,]$
$T \quad [\,K\,]$
$R_{PT100} \quad [\,\Omega\,]$
$R_{Cernox} \quad [\,\Omega\,]$
$\Delta T \quad [\,K\,]$
Slit
1
Slit
2
Si $(7\,7\,\overline{7})$
λ-meter
^{57}Fe
APD
Detector
Oven or
Cryostat Beam
Si or $\alpha-Al_2O_3$
single crystal
$[1\,1\,0]$
$[h\,k\,l]$
ψ
X-rays
$2\delta\theta$

3.2.3. Temperature control setup for the λ-meter
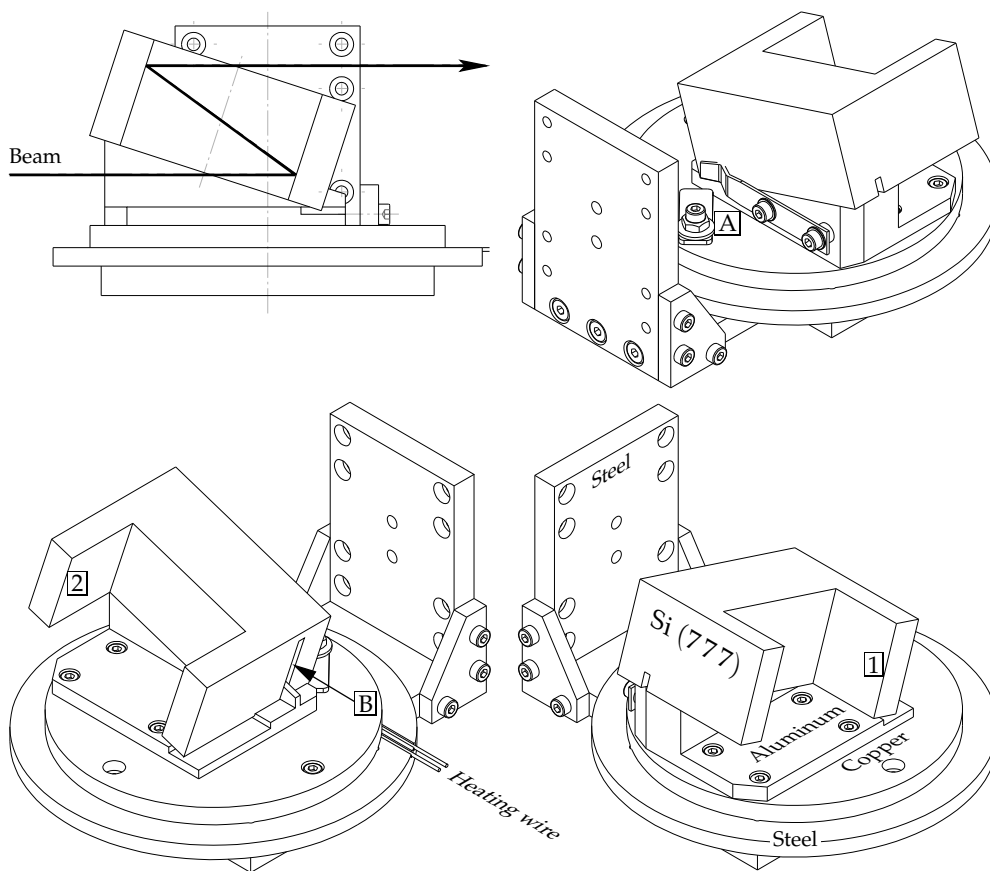
Fig. 3.2.3: Si $(7\,7\,7)$ *channel-cut crystal with holder (λ-meter). Top left panel: Side view with approximate beam path. Other panels: Isometric views with material annotations and positions of temperature sensors. [A],[B]: positions of PT100 thermoresistors; [1],[2]: positions of thermocouples*

[a)]The drawing is shown here as provided by the manufacturer. It does not reveal the details of the heat exchanger to the customer. The tilted sample holder was added to the drawing by the author.

The Si (7 7 7) channel-cut crystal in the λ-meter is sitting on an aluminum block which is mounted on a copper plate. The aluminum block holds the Si crystal in such a way that the synchrotron radiation beam hits the reflecting surfaces with an angle of incidence of about 74 ° when the copper plate is parallel to the beam, cf. Fig. 3.2.3. On the bottom side of the copper plate a heating wire is installed. The copper plate and the Si crystal are covered by a cylindrical plastic cap (not shown in the figure) with thermal insulation made of aluminum foil and rubber foam, and two small windows for the incoming and outgoing beam. Several temperature sensors can be mounted on the copper plate and the Si crystal, see Section 3.2.4.3 for details. The copper plate is mounted on a bracket made of stainless steel, providing both mechanical rigidity and thermal insulation. The upright part of the bracket is used to attach the λ-meter to a goniometer.

3.2.4. Temperature sensors

3.2.4.1. Choice

The choice of a thermometer type for our experiments is first of all determined by the fact that we want a computer based temperature control, data acquisition, and real-time remote data display. Therefore, only temperature sensors with an electrical output signal can be used. Among them, the most important types are *thermoresistors*, and *thermocouples*.

Thermoresistors make use of the fact that the resistance of an electrical conductor is temperature dependent. If this dependence is monotonous, stable, and has sufficient slope, while other influences on the resistance are small, then the resistance $R(T)$ can be used for temperature measurement. For temperatures between 77 K (liquid nitrogen) and ≈ 1200 K, platinum is very well qualified for this purpose. For lower temperatures, however, the slope of $R(T)$ for platinum is too small. Here some other types are preferable, like the *Cernox* thin-film thermoresistors from Lake Shore[a], which have a high negative slope at cryogenic temperatures. Both types of thermoresistor can be calibrated with 5 mK accuracy (Becker, 2002; Lake Shore, 1999), and allow the detection of temperature changes of 1 mK (Lucht, 1998) in their respective temperature ranges. They are also very resistant to radiation environments.

A thermocouple is basically a junction between two wires made of different metals. Over such a junction there is a *contact voltage* which is determined by the electromotive force originating from the difference of the chemical potentials of both materials. This contact voltage is temperature dependent. In a closed loop of conductors there are at least two junctions between the different materials in opposite orientation, so that the overall voltage vanishes if the junctions are at the same temperature, and the measured voltage depends on the temperature difference between the junctions.[b] A pair of thermocouples is therefore useful for measuring temperature differences. Absolute temper-

---

[a]Lake Shore Cryotronics, Inc., 575 McCorkle Blvd, Westerville, Ohio 43082, USA

[b]If only one thermocouple is connected to a voltage meter, then the connections between the thermocouple wires and the voltage meter are junctions between different metals, too.

ature values can be obtained by measurement of the difference between one thermocouple at the point of interest and the other at some well defined temperature reference, like boiling water, the triple point of water, liquid nitrogen, or a temperature controlled oil bath. The accuracy of such a measurement is then determined by the accuracy of the reference temperature, which is in most cases not better than 0.1 K.

We have therefore used Platinum thermoresistors for measurements around room temperature and above, and Cernox resistors below room temperature, down to 4.2 K, the temperature of liquid helium.

3.2.4.2. Properties

For platinum thermoresistors, the temperature dependence of the resistance is very well described by the quadratic equation

$$R(\vartheta) = R_0 \cdot (1 + A\vartheta + B\vartheta^2) \tag{3.2.1}$$

with ϑ the temperature in $°C$, R_0 the resistance at $\vartheta = 0\,°C$, and the parameters A and B which are to be determined either by calibration or standardization. For industrially manufactured platinum thermoresistors, the parameters are determined by the IEC 751 standard to

$$
\begin{aligned}
A_{\mathrm{IEC}} &= 3.9083 \times 10^{-3}\,\mathrm{K}^{-1} \\
B_{\mathrm{IEC}} &= -5.775 \times 10^{-7}\,\mathrm{K}^{-2}.
\end{aligned}
\tag{3.2.2}
$$

The most common type is the PT100. The $R(\vartheta)$ characteristic from Eq. 3.2.2 is used in most DMM[a] types that can display the temperature directly when connected to a PT100. It is also used for computing $R(\vartheta)$ tables.

The PT100 is available in different *tolerance classes*, where at $\vartheta = 0\,°C$ class A has an accuracy of 150 mK and class B 300 mK. If better accuracy is required, the parameters R_0, A, B of the individual thermoresistors have to be determined by calibration.

If the PT100 resistance is measured using a current of $I = 1\,\mathrm{mA}$, the thermoresistor will produce a heating power of $P = RI^2 \approx 0.1\,\mathrm{mW}$. This is however dissipated in the copper shell of the oven (Fig. 3.2.1), and is very small compared to the power of the heating wire which is typically $> 1\,\mathrm{W}$, so we don't consider this as a relevant error.

Cernox thermoresistors may sample out very different and thus have no standard characteristic. They have to be calibrated in any case, with an accuracy to be determined by the application. This is explained in detail in Section 3.2.4.4.

Thermocouples are available in different combinations of materials. Most of them are standardized and indicated by a single letter type classification. For measurements around room temperature the type K, which is constituted of nickel-chromium and nickel-aluminum wires, is by far the most common, and also used in the experiments described in this work. Its sensitivity is

---

[a] Digital MultiMeter

$\Delta U/\Delta T = 40\,\mu\text{V} \cdot \text{K}^{-1}$. Most other types have a much smaller sensitivity and are mainly useful at extremely low or high temperatures. Thermocouples are usually made by welding the wire tips together at a single point, leading to a very small temperature sensitive area.

3.2.4.3. Installation

The resistance of thermoresistors was always measured using the four wire technique, where one pair of wires is used to apply a current of $\approx 0.96\,\text{mA}$ to the resistor, and the other pair is used to measure the voltage only over the resistor but not over the wires.

The PT100 in the oven, manufactured by Thermocoax[a], is about 20 mm in length, enclosed in a stainless steel tube with 1.6 mm diameter. It is shown as black rectangle in Fig. 3.2.1. The tube is about 120 mm long and contains also the connection wires. This type of thermoresistor was used successfully before for experiments on exact Bragg backscattering on $\alpha-\text{Al}_2\text{O}_3$ by Shvyd'ko et al. (1998). Two considerations motivated the choice for this type:

1. It can be easily mounted in the oven by hard soldering or glueing, so that the PT100 is inside the oven close to the crystal, and the connecting wires are accessible from outside, and the oven remains vacuum-tight. This makes it possible to keep air inside the oven which helps to maintain a good spatial temperature homogeneity, while the oven is kept in vacuum for better thermal insulation. The requirement for air inside the oven was however dropped for the Mössbauer radiation wavelength measurements, since for stability of the Si lattice parameter one needs not only a stable temperature but also a stable pressure. This is easiest in vacuum.

2. The stainless steel tube protects the PT100 against damage during mounting or exchanging crystals.

However, during the experimental work on the measurement of the wavelength of the Mössbauer radiation of ^{57}Fe, which is described in Chapter 4, it turned out that the thermal conductivity of the tube covering the connection wires is a disadvantage of this type of temperature sensor. Although the thermal conductivity of stainless steel is small, it may still lead to considerable measurement deterioration if the temperature gradient along the tube is large enough. Some doubt on the impact of such a temperature gradient was still remaining after the last experiment on the measurement of the wavelength of the Mössbauer radiation of ^{57}Fe which was conducted at SPring-8 in 2002. To check for this kind of measurement errors, another type of PT100, the chip sensor made by Jumo[b], was used. It is made of a 1 mm thick ceramic substrate with a thin platinum layer one one surface. The smallest chip size available is $2\,\text{mm} \times 2.5\,\text{mm}$, thus allowing more flexibility in positioning the sensor, and more precise measurement of the temperature of a tiny spot. The sensors have

---

[a]THERMOCOAX, 40 Bld Henri Sellier, 92156 SURESNES, Cedex, France

[b]Jumo GmbH & Co. KG, Moltkestr. 13–31, 36039 Fulda, Germany

been connected with four Manganin[a)] wires of 200 µm diameter. The thermal conductivity of Manganin is about one order of magnitude smaller than of copper, and the contact voltage at the connection between Manganin and copper wires is neglibly small. Therefore Manganin is the ideal material for the wires if both the errors introduced by thermal conductivity and contact voltages shall be minimized. To avoid additional thermal conduction, the wires are insulated only with a thin layer of lacquer, and no additional covering is used. Three sensors of this type have been installed inside the oven (at the positions [2], [4], and [5] in Fig. 3.2.1) to find temperature corrections for the reading of the Thermocoax PT100; this will be discussed in detail in Section 3.2.6. These sensors have to be mounted very carefully because the thin wires get easily damaged. For sensors inside the oven it is very important to make sure that at least some cm of the Manganin wires are also inside the oven, to make the temperature gradient along the wires as small as possible.

During the last experiment on the measurement of the wavelength of the Mössbauer radiation of ^{57}Fe described on p. 51, we had already installed a pair of thermocouples in the oven, at positions [1] and [2] as shown in Fig. 3.2.1. These are used to measure the temperature difference between the PT100 and the crystal surface. However, they do not allow the determination of systematical errors of the PT100 which may be introduced by a temperature gradient along the connection wires.

In the LHe flow cryostat, two Cernox sensors are installed, one at the copper block of the sample holder (see Fig. 3.2.2), another one somewhere at the heat exchanger. Unfortunately the manufacturer of the cryostat does not provide information about the internals of the heat exchanger, like the locations of the LHe tubes, the temperature sensor, and the heating wire.

On the λ-meter, the PT100 is mounted either on the copper plate (position [A] in Fig. 3.2.3) with a clamp, or in a narrow (2 mm) gap in the Si crystal (position [B]). The latter position has the advantage that the PT100 is measuring the temperature of the Si crystal directly. It is however difficult to find a good working set of parameters for the temperature controller in this case, since the thermal coupling with the heating wire under the copper plate is indirect. Therefore position [A] was preferred in the earlier experiments. Additionally, a pair of thermocouples (positions [1] and [2]) can be installed on the faces of the channel-cut crystal to check whether their temperatures are the same.

[a)]Alloy of 86 Cu, 12 Mn, 2 Ni

3.2.4.4. Calibration

For the determination of the Mössbauer radiation wavelength of ^{57}Fe it is necessary to have a precisely calibrated temperature sensor at 22.5 °C, the temperature where the lattice parameter of the Si reference crystal is given.

The Thermocoax PT100 in the oven, together with the wires and the Keithley[a] 2002 DMM used to measure its resistance, have been calibrated in the range from 0 °C to 100 °C at the PTB. The whole oven with the built-in thermoresistor was submerged in a stirred, temperature controlled oil bath, and the temperature reading of the Keithley 2002 DMM[b] was compared with the temperature measured by a reference PT25 thermometer placed as close as possible to the PT100 under study (Becker, 2002).

The calibration procedure has been repeated three times in the years 1999 and 2001. The first calibration includes five points around 22.5 °C with a stated measurement accuracy of 5 mK, and one single point at 100.243 °C with an accuracy of 10 mK. The second calibration includes four points around 22.5 °C and one point at 0 °C. The stated accuracy is only 50 mK due to a different measurement setup. The third calibration covers a narrow range around 22.5 °C with four data points, and a stated accuracy of again 5 mK.

The resulting $T(R)$ dependence from the third calibration is shown in Fig. 3.2.4, together with the standard IEC751 $T(R)$ characteristic. The temperature readings obtained from the PT100 resistance by using the $T(R)$ calibration are about 300 mK below the readings that would result from the IEC751 curve. This is still within the manufacturer stated accuracy and shows clearly the importance of calibration.

Within the temperature range from 16 °C to 27 °C, the following linear function has been fitted to the $T(R)$ data points of the third calibration:

$$T_1(R) = (-253.073 + 2.53075 \, \Omega^{-1} \cdot R) \, °C. \tag{3.2.3}$$

Fig. 3.2.5 displays the deviation of all the three calibrations from the IEC751 characteristic, together with their stated calibration errors. As one can see, the results agree within ≈ 5 mK. This shows that also the results of the second calibration are very reliable despite the worse stated accuracy given by the PTB, and that the PT100 and the DMM are very stable over long time.

Thus is should be possible to meet the temperature requirement stated in Section 3.1.1.

The three PT100 chip sensors from Jumo which were used for additional temperature measurements in the oven were also calibrated at the PTB, together with the complete wiring and the Keithley 2002 DMM. The same method as for the built-in Thermocoax sensor was applied, with the only difference that the Jumo sensors were mounted in the oven *after* the calibration. The deviations between the temperature readings of the three PT100 chip sensors according to the calibration and the IEC751 characteristic are shown in Fig. 3.2.6.

---

[a] Keithley Instruments, Inc., 28775 Aurora Road, Cleveland, Ohio 44139, USA

[b] The Keithley 2002 can display temperature readings from a PT100 by measuring the resistance and computing the temperature from the IEC751 characteristic internally.

^{57}Fe
APD
Detector
Oven or
Cryostat
Si or $\alpha-Al_2O_3$
single crystal
[1 1 0]
[h k l]
ψ
X-rays
$2\delta\theta$
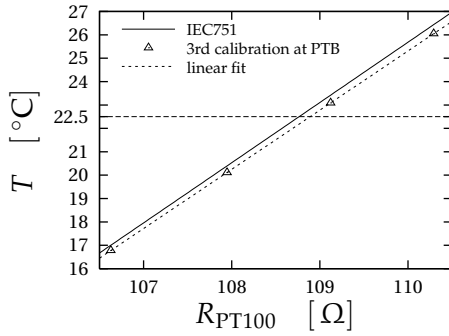
Fig. 3.2.4: Comparison of the latest PTB calibration of the Thermocoax PT100 with the standard characteristic defined in IEC751. The stated accuracy of the calibration is 5 mK. The dotted line is the linear fit function Eq. 3.2.3.
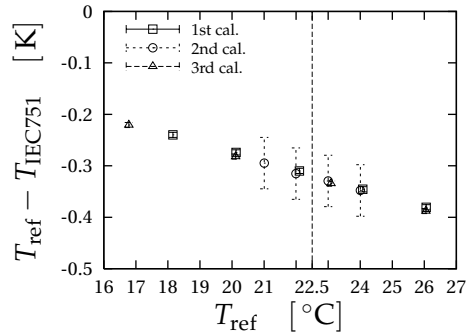
Fig. 3.2.5: Deviations of the PTB calibrated temperature reading from the Thermocoax PT100 from the IEC751 characteristic, according to three subsequent calibrations of the same sensor

^{57}Fe
APD
Detector
Oven or
Cryostat
Si or $\alpha-Al_2O_3$
single crystal
[1 1 0]
[h k l]
ψ
X-rays
$2\delta\theta$

Fig. 3.2.6: Deviations between the PTB calibrated temperature readings of the three Jumo PT100 chip sensors and the standard characteristic defined in IEC751
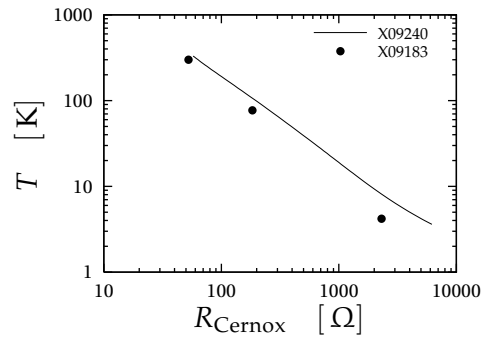
Fig. 3.2.7: Calibration data for the two Cernox thermoresistors in the LHe flow cryostat. The solid line shown for X09240 is an interpolation curve through 71 $T(R)$ data points.

The Jumo sensors are labeled #2, #3, #4 because the label #1 was already in use for the Thermocoax PT100. The following linear functions have been fitted to the $T(R)$ data points from the calibration of the respective sensor:

$$T_2(R) = (-0.0957961 + 2.57074\,\Omega^{-1} \cdot [R - 100\,\Omega])\,°\text{C} \qquad (3.2.4)$$

$$T_3(R) = (-0.0737399 + 2.57275\,\Omega^{-1} \cdot [R - 100\,\Omega])\,°\text{C} \qquad (3.2.5)$$

$$T_4(R) = (-0.1146922 + 2.57204\,\Omega^{-1} \cdot [R - 100\,\Omega])\,°\text{C}. \qquad (3.2.6)$$

The Cernox sensor at the sample holder of the liquid helium flow cryostat has been calibrated by its manufacturer Lake Shore, at 71 points in the temperature range from 3.6 to 331 K, against Germanium and Platinum resistance standards. The other Cernox sensor at the heat exchanger has only been tested roughly at room temperature and in open dewars filled with liquid Nitrogen or Helium. The $T(R)$ dependence for both sensors is displayed in Fig. 3.2.7. In Tab. 3.2.1 a summary of the calibrat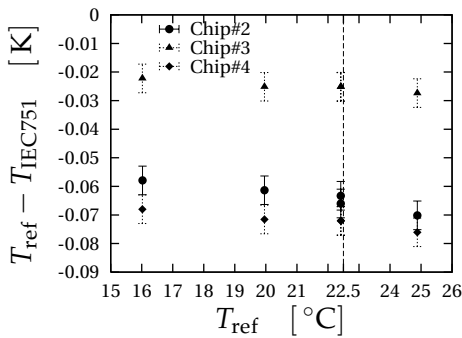ion results of both sensors is shown, together with the stated calibration accuracy of the sensor at the sample holder. The differences in the resistance readings of two sample Cernox sensors at the same temperature can bee seen very clearly in the figure and the table.

Serial No.	Position	$R\,[\,\Omega]$ @ $T = 300\,\text{K}$	$R\,[\,\Omega]$ @ $T = 77\,\text{K}$	$R\,[\,\Omega]$ @ $T = 4.2\,\text{K}$
X09183	heat exchanger	52.6	184.0	2310
X09240	sample holder	63.1	255.2	5045
Stated accuracy		$\Delta T\,[\,\text{mK}]$ @ $T = 300\,\text{K}$	$\Delta T\,[\,\text{mK}]$ @ $T = 77\,\text{K}$	$\Delta T\,[\,\text{mK}]$ @ $T = 4.2\,\text{K}$
X09240	sample holder	50	25	4

Tab. 3.2.1: Calibration data of Cernox thermoresistors in the liquid helium flow cryostat

The PT100 at the λ-meter was not calibrated because here we are, as explained in Section 3.1.2, only interested in temperature stability but don't need to know the exact temperature value.

3.2.5.   Temperature control

Keeping a temperature stability of about 1 mK is possible with the methods described in great detail by Lucht (1998). The backscattering crystal is placed inside an oven designed for high temperature stability (see Section 3.2.1). Its temperature is measured with a PT100 and a DMM with an internal high resolution ADC[a]. A PID[b] controller program running on a PC[c] calculates from the measured PT100 resistance the appropriate heating voltage to keep the temperature constant. The heating voltage is applied to the heating wire inside the oven by a power supply with an internal high resolution DAC[d]. The

---

[a] Analog to Digital Converter
[b] Proportional-Integral-Differential
[c] Personal Computer
[d] Digital to Analog Converter

data transfer from the DMM to the PC, and from the PC to the power supply is made by GPIB[a)] interfaces. The controller program is able to control multiple temperature sensors simultaneously. The setpoints and measured temperatures can be recorded to a file periodically. It is also possible to record the readings of additional temperature sensors which are used for measurements only but not for control. The same temperature control technique is applied for the oven, the λ-meter, and the LHe cryostat.

This works well even with uncalibrated temperature sensors if the aim is to keep the temperature *stable*, i.e. to make sure that it does not change by more than 1 mK over time. If however one wants to set the temperature *accurately* to a predefined value, like the 22.5 °C where the Si lattice parameters are very well known, then the PT100 sensors have to be calibrated, since the deviation of commercially available standard sensors from the IEC751 characteristic (Eqs. 3.2.1, 3.2.2) may be up to 300 mK. This was discussed in Section 3.2.4.4.

3.2.6. Temperature correction

The experiment for the measurement of the wavelength of the Mössbauer radiation of ^{57}Fe has been performed four times at different synchrotron radiation facilities, as described in Chapter 4. The results of the last experiment, conducted at SPring-8 in 2002, and its comparison with the previous results, gave reason to some doubt about the assumed temperature homogeneity in the oven. Therefore, measurements of the temperature distribution became necessary. These measuements lead to a temperature correction that has to be applied to the reading of the PT100 in the oven.

It is a general problem in temperature measurements that only the temperature of the thermometer itself is measured, while the aim is the knowledge of the temperature of the object under study. Thus, the experimental data achieved so far may be deteriorated not only by some difference of the temperature of the PT100 and the surface of the Si backscattering crystal, but also by the thermal conduction along the connecting wires ant the shielding of the PT100.

In the calibration procedure described in Section 3.2.4.4, the oil bath ensures both a good thermal contact between the reference thermometer and the PT100 to be calibrated, and low temperature gradients along the connection wires. But in the real experiments performed with this oven the situation is not like that because the oven is kept in vacuum inside a chilled tank (see Section 3.2.1). This leads to a temperature difference of some K which may appear along the connection wires of the PT100. Since the wires of the Thermocoax PT100 are shielded by stainless steel, a material with low thermal conductivity, the influence of such a temperature gradient has been underestimated for a long time.

There are two main causes of the temperature difference of the PT100 and the crystal:

[a)]General Purpose Interface Bus. Also known as HP-IB or IEEE 488

1. If the oven is chilled from outside and the temperature gradient along the connecting wires is large enough, the PT100 will be colder than its surrounding. Thus if we set the setpoint to the desired temperature of the crystal, the crystal will be *too warm*.

2. If the oven window is not shielded well enough, some heat exchange between the crystal and the environment may occur by means of thermal radiation. Depending on the environmental temperature this may lead to temperature measurement errors in either direction. However, if the vacuum tank is strongly chilled, there may be thermal radiation from the crystal through the window to the tank, and the crystal will be *colder* than the PT100.

Without further experimental data it is hard to tell which of the effects is dominant. Therefore the three calibrated Jumo PT100 sensors were used to determine the temperature differences. They were mounted at the positions [2], [4], and [5] shown in Fig. 3.2.1. The sensor [4] allows one to measure directly the temperature of the spot where the synchrotron radiation beam would hit the crystal surface.[a] The difference of the readings of the sensor [4] and the Thermocoax PT100 is the temperature correction we need to apply to the experimental data which were obtained only with the Thermocoax PT100.

The other two Jumo sensors provide additional information about the temperature distribution inside the oven, and thus about the possible reason of measurement errors of the Thermocoax PT100. From the readings of the sensors [2] and [4] one can determine the temperature difference between the crystal surface and the Thermocoax PT100. The sensor [5] is measuring the temperature of the connection wire shielding at a point close to the outer surface of the copper cylinder. A temperature differece along the Thermocoax PT100 itself is detected by the difference of the readings of the sensors [2] and [5]. This gradient may lead to a measurement error of the Thermocoax PT100, which is directly measured by the difference of the readings of the Thermocoax PT100 and the Jumo sensor [2].

With this setup, the temperature distribution was measured for different operating conditions of the oven. These conditions and the measured temperatures of the different sensors are summarized in Tab. 3.2.2. The temperature values shown in this table are derived from the resistance readings and the calibrations $T(R)$ for the respective sensor, given in Eqs. 3.2.3 to 3.2.6.

Herein, the operation at a chilling water temperature of 5 °C resembles the operating conditions at the APS experiment (Shvyd'ko et al., 2000), where the facility-wide chilling water supply without temperature control was used. In the experiments at SPring-8 and in the measurement of the temperature distribution, a temperature control was applied to the chilling water. In the first experiment at SPring-8, May 2001, the chilling water temperature has been set to 5 °C to reproduce the conditions from APS, but in the second experiment at SPring-8, February 2002, the setpoint of the chilling water temperature was

---

[a] Obviously, the sensor has to be removed from the position [4] before the real experiment with synchrotron radiation, because otherwise it would block the beam.

Temperature settings					
Chilling water	[°C]	5.0	18.0	19.0	20.0
Thermocoax PT100 #1	[°C]	22.500	22.500	23.500	24.500
Temperature readings					
Jumo PT100 #2 @ pos. [5]	[°C]	20.00(10)	21.70(10)	22.75(10)	23.60(10)
Jumo PT100 #3 @ pos. [2]	[°C]	22.63(5)	22.545(5)	23.547(5)	24.550(7)
Jumo PT100 #4 @ pos. [4]	[°C]	22.61(5)	22.525(5)	23.528(5)	24.535(7)
Temperature corrections					
Jumo [4] - Thermocoax	[K]	0.11(5)	0.025(5)	0.028(5)	0.035(7)
Jumo [2] - Thermocoax	[K]	0.13(5)	0.045(5)	0.047(5)	0.050(7)
Jumo [4] - Jumo [2]	[K]	0.020(5)	0.020(5)	0.019(5)	0.015(7)
Jumo [5] - Jumo [2]	[K]	−2.50(10)	−0.70(10)	−0.75(10)	−0.90(10)

Tab. 3.2.2: Temperature readings of the three Jumo PT100 sensors, and corresponding temperature corrections, under different operating conditions of the oven. The numbers in square brackets denote sensor positions as displayed in Fig. 3.2.1.

4.5 K below the setpoint of the Thermocoax PT100. Under this condition the temperature gradients in the oven have been kept low, but still large enough for the temperature control to work stable.

The results in Tab. 3.2.2 show clearly that there is a considerable impact of temperature gradients on the temperature measurements with the Thermocoax PT100. The difference between the center of the Thermocoax PT100 (pos. [2]) and the connection point of the wires (pos. [5]) is in the range of a few Kelvin. This leads, for a chilling water temperature of 5 °C, to a temperature measurement error of the Thermocoax PT100 of about 130 mK. The temperauture gradient between the Thermocoax PT100 and the crystal surface (pos. [4]) has a small effect in opposite direction. Thus, the total measurement error with respect to the crystal surface is about 110 mK, with the crystal being warmer than the Thermocoax PT100 reads. This leads to a relative error of the lattice parameter *a* of the Si reference crystal of about 2.6×10^{-7} to larger values. Thus, if we are interested in the value of *a* at the temperature which is read from the Thermocoax PT100, we have to correct the measured value of *a* to a lower value.

The wavelength of the Mössbauer radiation of ^{57}Fe is calculated by $\lambda_M = a_0/\tilde{a}$ with a_0 the presumed lattice parameter of the Si reference crystal at 22.500 °C, and $\tilde{a}$ the lattice parameter of the Si reference crystal in units of λ_M, determined by the experiment—see Section 4.3 for a detailed description of the data evaluation procedure. Using the temperature corrected value of $\tilde{a}$ instead of the uncorrected one will lead to a higher value of λ_M.

For chilling water temperatures of 18 °C, 19 °C, and 20 °C, the temperature corrections which have to be applied are much smaller, about 30 mK, but still large enough to be taken into account.

In the sections 4.3 and 4.4 the impact of the temperature corrections on the final results for the wavelength of the Mössbauer radiation of ^{57}Fe will be further discussed.

3.2.7. Temperature gradients in the λ-meter crystal

The λ-meter has also undergone some checks for temperature gradients along the Si $(7\,7\,7)$ channel-cut crystal. Such gradients could deteriorate not only the intensity and spectral distribution of the transmitted radiation. If the gradient varies with the environmental temperature, also the assumption that the temperature of the Si $(7\,7\,7)$ channel-cut crystal is constant during one run of the experiment is violated.
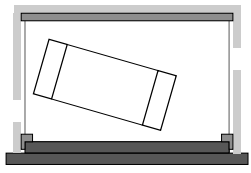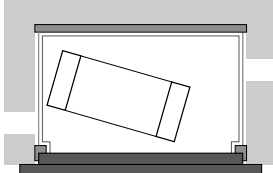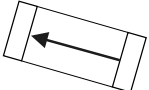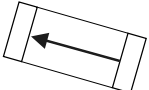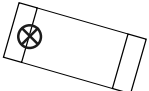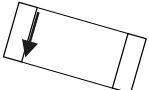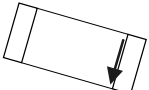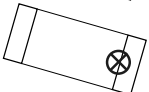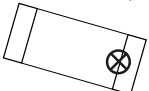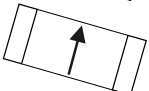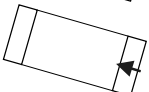
Therefore some table-top experiments have been made to measure the the temperature gradients along the surfaces of the λ-meter crystal with a pair of thermocouples. The operating conditions from the different experiments where the λ-meter was used at synchrotron radiation facilities have been resembled in these table-top experiments. The operating conditions have been altered by different setpoints for the temperature control, and by use of different insulation caps, as shown in the top rows of Tab. 3.2.3. The thin insulation cap, with a PT100 resistance setpoint of $112\,\Omega$, has been used in the experiments for the measurement of the wavelength of the Mössbauer radiation of ^{57}Fe at HASYLAB and APS. The other insulation cap, with thick rubber foam and an additional aluminum foil on the inside, was used in the two experiments at SPring-8, and also in the experiment at PETRA for the measurement of the lattice parameters of $\alpha-\mathrm{Al_2O_3}$. With a room temperature of about $22.5\,^\circ$C, a setpoint of $R = 109\,\Omega$ ($\vartheta = 23.107\,^\circ$C) is the lowest where the temperature control is operating stable. See Chapter 4, in particular Section 4.4, and Chapter 5 for details of these experiments.

To avoid damage of the specially prepared surfaces of the original Si $(7\,7\,7)$ channel-cut crystal by thermocouples and heat conductive compound, these studies were performed with another Si $(7\,7\,7)$ channel-cut crystal of the same shape but with no special surface treatment.

A total of 22 different combinations of thermocouple positions, setpoints and insulations were tested. The details of these operating conditions and the measured temperature differences are shown in Tab. 3.2.3.

The measurements show that temperature gradients are mainly a problem within the faces of the Si $(7\,7\,7)$ channel-cut crystal (rows No. 3, 4, 5, 6, and 9). Since the beam will hit the surfaces on different spots if the λ-meter is rotated, this could lead to some error in the interplanar distance, and thus, in the glancing angle. Furthermore, with such angular errors, the direction of the transmitted beam might slightly vary when the λ-meter is rotated.

With the thin insulation and the setpoint $R = 112\,\Omega$, the temperature differences across the faces of the channel-cut crystal come close to the temperature width of about $0.14\,$K which was derived in Section 3.1.2. With the thick insulation and the setpoint $R = 109\,\Omega$ the temperature differences are about 5 times lower.

	Si (7 7 7) λ-meter ^{57}Fe APD Detector Oven or Cryostat Si or $\alpha-$Al$_2$O$_3$ single crystal [1 1 0] [h k l]	Si (7 7 7) λ-meter ^{57}Fe APD Detector Oven or Cryostat Si or $\alpha-$Al$_2$O$_3$ single crystal [1 1 0] [h k l]
Insulation	ψ X-rays $2\delta\theta$	ψ X-rays $2\delta\theta$
Setpoint ϑ [$^\circ$C]	30.844	23.107 30.844 *heater*
Setpoint R [Ω] (PT100)	112	109 112 *off*

Locations of thermocouples and direction of temperature gradient	Temperature difference ΔT [mK]			
	-9	9	4	10
	29		10	
	111	1	33	
	39			
	97	18	33	
	107	21	60	
		16		
	12		1	
	94	13	52	

Tab. 3.2.3: Measurements of the temperature distribution along the Si (7 7 7) *channel-cut crystal in the λ-meter under different operating conditions, which resemble the different experiments for the measurement of the wavelength of the Mössbauer radiation of* ^{57}Fe. *The top row shows the different types of insulation caps. Center:* 2 mm *rubber foam; right:* 25 mm *rubber foam outside and thin aluminum foil inside. The left column shows the* Si (7 7 7) *channel-cut crystal viewed from the open side and from the top. A pair of thermocouples was used to measure the temperature differences. The arrow points from the position of one thermocouple to the other. The head of the arrow denotes the position where the higher temperature is measured. The temperature setpoint is given both as the resistance value R of the PT100 thermoresistor used for the temperature measurement, as well as the correspondung temperature value ϑ according to Eqs. 3.2.1 and 3.2.2.*

The temperature gradients are probably caused by the fact that the heat source is only below the crystal, and that the heat exchange between heater and crystal works mostly through the aluminum socket where the crystal is sitting on.

3.2.8.   Recommendations for future experiments

The evaluation of the temperature distribution in the oven has shown that the use of the Thermocoax PT100 is not suitable well enough for the high precision temperature measurements and control which are required in experiments for the determination of the wavelength of the Mössbauer radiation of ^{57}Fe. Additional temperature corrections become necessary which make the data evaluation more complicated and introduce possible new error sources.

For future experiments where the oven is used, it is therefore recommended not to use the Thermocoax PT100 at all. Instead only the calibrated Jumo PT100 chip sensors with Manganin connecting wires should be applied, and installed as described in Section 3.2.4.3 on page 35. Obviously the PT100 cannot be installed at pos. [4] in Fig. 3.2.1 in a real synchrotron radiation experiment. Instead, one sensor could be installed at pos. [1] to measure the temperature at a spot very close to the synchrotron radiation beam, and another one at pos. [2] in direct contact with the copper shell, for a precise temperature control. It could also be possible to use a single Jumo PT100 sensor at pos. [3], where it is in direct thermal contact with the copper shell and also close to the crystal surface.

One should also think about an improvement of the temperature homogeneity by filling the oven with some contact gas under low pressure. The pressure should not exceed some mbar, otherwise the uncertainty of the pressure itself could also deteriorate the measurement of the lattice parameter of the Si reference crystal. However, if we want to keep the vacuum surrounding the oven for better thermal insulation, a vacuum-tight feed-through for the connection wires of the temperature sensors will be necessary. While this is already the case for the Thermocoax PT100, for the Jumo PT100 an appropriate feed-through still needs to be deployed.

The Thermocoax PT100 is still good enough in experiments where it is required to keep the temperature of a crystal inside the oven stable, while accurate knowledge of the temperature is less important. In such a case the mechanical robustness of the Thermocoax PT100 is an advantage over the installation of Jumo sensors which is prone to damage.

In addition to the operating recommendations given at the end of Section 3.2.7, the temperature gradients in the λ-meter could also be minimized by other means. Instead of the insulation cap, one could use a more sophisticated tank where all surfaces are temperature controlled, not only the bottom. Furthermore, one could mount the crystal on a thermally insulated socket, so that the heat exchange works mostly by radiation and by conduction through the surrounding air.

Chapter 4

Measurements of the wavelength of the Mössbauer radiation of ^{57}Fe

The measurement of the wavelength of the Mössbauer radiation of ^{57}Fe has been carried out four times in the years 1998 to 2002. The experiments from HASYLAB in 1998 and from APS in 1999 are published by Shvyd'ko et al. (2000). The other two experiments, which were performed at the the 1 km beamline BL29XUL (Ishikawa et al., 2001) at SPring-8, are reported for the first time in the present thesis. In the experiment in 2001, the author has worked with direct participation of T. Ishikawa, A.Q.R. Baron, K. Tamasaku, and M. Yabashi from SPring-8, Yu. V. Shvyd'ko[a] from the University of Hamburg (Germany), and J. P. Sutter[b] from HASYLAB (Hamburg, Germany). The same staff from SPring-8 took part with the author's experiment in 2002, together with M. Lerche[c] and H.-C. Wille[d] from the University of Hamburg (Germany).

One can use basically use the same method both to ascertain the wavelength of the Mössbauer radiation of ^{57}Fe, λ_{M}, from the well-known lattice parameter of a Si reference crystal, and vice versa to measure the lattice parameters of some other single crystal in units of the Mössbauer wavelength standard λ_{M}. We will discuss therefore the general method in Section 4.1 and will address the differences where appropriate. Then in Section 4.2 we will show how to calculate the ratio between Mössbauer radiation wavelength of ^{57}Fe and lattice parameters from the raw data obtained in the experiment. Here we will also discuss the possible sources of uncertainty. In Section 4.3 the data evaluation procedure will be demonstrated by the experimental data obtained in an experiment conducted at SPring-8 in February 2002. This will lead to a result which is slightly different from the value of the Mössbauer radiation wavelength of ^{57}Fe we have published earlier as a result of a previous experiment at the APS (Shvyd'ko et al., 2000). The changes in the results originate from the technical improvements of the setup during several performances of the experiment. These changes will be discussed in Section 4.4 together with

---

[a]Current address: Yu. V. Shvyd'ko, Advanced Photon Source, Argonne National Laboratory, 9700 South Cass Avenue, Argonne, Illinois 60439, USA

[b]Current address: J. P. Sutter, SPring-8, Japan Synchrotron Radiation Research Institute (JASRI), 1-1-1 Kouto Mikazuki-cho Sayo-gun Hyogo 679-5198, Japan

[c]Current address: M. Lerche, Department of Geology, University of Illinois at Urbana Champaign, 1301 W. Green Street, Urbana, Illinois 61801, USA

[d]Current address: H.-C. Wille, Nuclear Resonance Group, European Synchrotron Radiation Facility, BP220, 38043 Grenoble Cedex, France

their expected or (if possible) observed impact on the uncertainty of the results.

Some issues which are dependent on changes in the setup will be addressed in general in Section 4.1 and Section 4.2, and then discussed in detail in Section 4.4.

4.1. Experimental setup
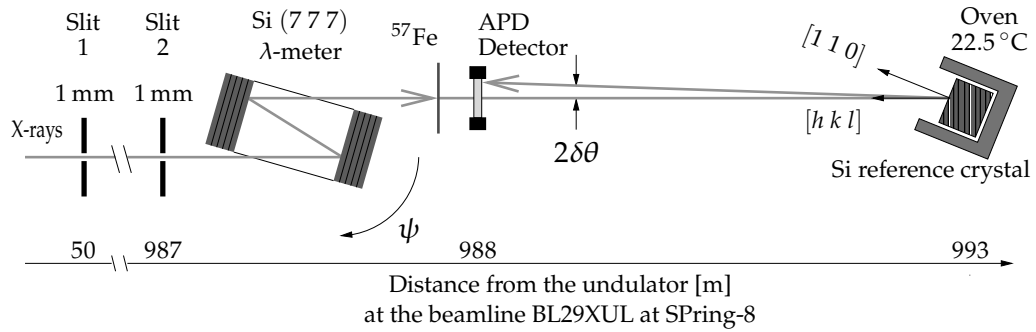
Fig. 4.1.1: Setup for the experiment to measure the Mössbauer radiation wavelength of ^{57}*Fe in units of the lattice parameter of* Si.

The setup of the experiment which allows one to determine the ratio of the lattice parameter of a Si reference crystal and the wavelength of the Mössbauer radiation of ^{57}Fe is shown in Fig. 4.1.1.

The synchrotron radiation coming from an undulator and premonochromatized by a high heat load monochromator (not shown in the figure) to an energy bandwidth of some eV is passing through two narrow vertical slits. These are used to collimate the beam to an angular width of some µrad, and to keep the beam direction fixed, independently from the beam energy. Even if the direction of the outgoing radiation from the high heat load monochromator should be unstable or change with energy, the slits may cut down the intensity but the beam direction after the slits will remain the same.

The beam is passing through the λ-meter, a Si channel-cut crystal where it is two times reflected by the symmetric Bragg reflection

(7 7 7). The angle of incidence Θ of the beam to the (7 7 7) atomic planes is varied by rotating the channel-cut crystal by the angle ψ, thus changing according to Bragg's law the wavelength λ of the radiation exiting the λ-meter. The channel-cut geometry ensures that the direction of incoming and outgoing beam are always parallel. The temperature of the λ-meter is kept constant with a stability of some mK—see Chapter 3 about the technical details.

The angular acceptance of the (7 7 7) Bragg reflection in Si for x-rays with $\lambda \approx 86$ pm is $\Delta E = 1.2$ µrad, corresponding to an energy bandpass of 5.3 meV and an intrinsic relative width $\Delta\lambda/\lambda = 3.5 \times 10^{-7}$. Thus it should be possible to measure wavelengths with a better relative accuracy than 10^{-7}. To achieve this goal it is necessary that both the angular divergence and the variation of

the direction of the incident beam are below the 1.2 μrad limit imposed by the angular acceptance of the $(7\,7\,7)$ reflection. This is what the slits are used for.

If the wavelength transmitted by the λ-meter coincides with λ_M, it will excite coherently the ^{57}Fe nuclei in an α-Fe foil. The foil is enriched to 95% in ^{57}Fe, and its thickness is 6 μm. The excited nuclei emit Mössbauer radiation in forward direction with an average delay of 141 ns.[a] The synchrotron radiation comes in short pulses of some 100 ns distance and about 100 ps duration. Thus it is possible to discriminate the Mössbauer quanta from the prompt synchrotron radiation pulses.

At a distance of 5 m downstream from the λ-meter the backscattering single crystal is positioned. The backscattering geometry is used because only in this case the angular acceptance of the reflection scales with the square root of the relative spectral width, cf. Section 2.2.8. For the measurement of the wavelength of the Mössbauer radiation of ^{57}Fe, two differently shaped Si reference crystals obtained from the PTB were in use as the backscattering crystal. Their lattice parameters have been precisely determined beforehand (Becker, 2001; Becker et al., 1981). To measure the lattice parameters of $\alpha-Al_2O_3$ a sample thereof is used as backscattering crystal.

The backscattering crystal is mounted in a thermostat—oven or cryostat, depending on the desired temperature range. See Chapter 3 for details of these devices. For the Si reference crystal only the oven is used since we are interested here only in a narrow temperature range around 22.5 °C. The thermostat is installed on a 4-circle goniometer which allows the orientation of the crystal to back-reflect with different sets of lattice planes $(h\,k\,l)$ the x-rays having passed the λ-meter. The λ-meter has to be rotated to establish the coincidence of the wavelengths of the Si $(7\,7\,7)$ reflection and the $(h\,k\,l)$ back-reflection. Back-reflections with $2d_{hkl}$ close to λ_M are chosen.

Close to the exit of the λ-meter, an APD detector (Baron, 2000) is mounted in the beam path. It consists of a silicon wafer of 100 μm thickness which is semitransparent for the 14.4 keV x-rays. Thus it will let pass $\approx 50\%$ of the incident beam through, and can detect the prompt synchrotron radiation pulses and the delayed Mössbauer quanta coming from the λ-meter, as well as the back-reflected pulses. The time of flight of the back-reflected photons from the APD to the reflector and back is 30 ns for a 5 m beam path in between. The time resolution of the APD is ≈ 1 ns which allows easy discrimination of the Mössbauer radiation and the back-reflected pulse from the prompt pulse.

An aperture close to the exit of the λ-meter is used to align precisely the exact backscattering condition using an auto-collimation technique. The aperture is first adjusted so that the incoming beam passes the hole at its center, and then the backscattering crystal is aligned to let the reflected beam also pass through the hole. Aperture diameters as narrow as 0.1 mm were used, allowing to keep the deviation from exact backscattering below 10 μrad with

---

[a]Differently from the setup shown in Fig. 4.1.1, it is also possible to install the ^{57}Fe foil upstream of the λ-meter. In this case Mössbauer radiation will be generated whenever λ_M is within the bandpass of the high heat load monochromator, but it will only be further transmitted if it is also inside the bandpass of the Si $(7\,7\,7)$ channel-cut crystal.

5 m beam path.[a)] Apertures with larger diameters are used for a rough pre-alignment.

With the cubic symmetry of Si, some multiple beam diffraction may occur in the exact backscattering condition, resulting in poor intensity and energy shifts of the reflected beam (Steyerl and Steinhauser, 1979; Sutter, 2000). Therefore the aperture is removed after exact backscattering is adjusted, and the Si reference crystal is rotated 100 µrad off before the wavelength measurement with the λ-meter. See Section 2.3 for theoretical details on this subject and Section 6.4 for experimental results where this effect is actually showing up. With $\alpha-\mathrm{Al_2O_3}$, which has a hexagonal symmetry, the experiment is less affected by such a problem. Here, many reflections are free from multiple beam diffraction, and for other reflections the angular region where multiple beam reflection occurs is much narrower (Lerche and Shvyd'ko, 2004).

In one *run* of the experiment, the rotation angles ψ of the λ-meter are measured for the cases of transmission of Mössbauer radiation, and of transmission of back-reflected radiation for at least $n+1$ reflection planes with different $2d_{hkl}$, where n is the number of independent lattice parameters in the backscattering crystal to determine. The angular differences $\Delta\psi_{(hkl)}$ between the angular positions of the λ-meter for transmission of Mössbauer radiation and back-reflected beam are recorded for each back-reflection. In the following section we will discuss how to calculate the ratio between the wavelength of the Mössbauer radiation and the lattice parameters of both the backscattering crystal and the Si $(7\,7\,7)$ channel-cut crystal from a set of $n+1$ measurements of $\Delta\psi_{(hkl)}$.

4.2. Theory of the determination of the results

Weakly absorbing single crystals, like Si or $\alpha-\mathrm{Al_2O_3}$, reflect x-rays with a glancing angle of incidence θ_c to the atomic planes within a wavelength region centered around λ_c which is determined by Eq. 2.2.59, which can be rewritten as

$$\sin\theta_c = \frac{\lambda_c}{2d}\left(1 + w_H\right). \qquad (4.2.1)$$

This differs from Bragg's law by a small but important refractive correction w_H which is given in Eq. 2.2.60. Using Eqs. 2.2.5 and 2.2.6, and assuming $b = -1$, one can rewrite Eq. 2.2.60 in the form

$$w_H = \frac{2r_e\,d^2}{\pi\,V}\sum_a N\left[Z_a + f_a'(\lambda)\right], \qquad (4.2.2)$$

where r_e is the classical electron radius, V is the unit cell volume, N_a is the number of atoms of type a in the unit cell, Z_a is their atomic number, and $f_a'(\lambda)$ is the real anomalous correction to their forward scattering amplitude, respectively.

[a)]Note that when the deviation of the incident beam from normal incidence to the reflecting atomic planes in the backscattering crystal is $\delta\theta$, then the angle between incident and reflected beam is $2\delta\theta$.

To change λ_c the λ-meter is rotated. The rotation angle ψ, shown in Fig. 4.1.1, is measured directly in the experiment, but may be different from the glancing angle of incidence θ in Eq. 4.2.1. They are identical only if the rotation axis ψ is perfectly aligned perpendicular to the incident beam $\mathbf{k_0}$ and parallel to the $(7\,7\,7)$ atomic planes. Otherwise we have to apply a small correction. If ξ is the deviation from perpendicular alignment between the rotation axis ψ and $\mathbf{k_0}$, and η is the angle between ψ and the $(7\,7\,7)$ planes, then the relation between ψ and θ reads:

$$\sin\theta = \sin\psi\cos\eta\,\cos\xi + \sin\eta\,\sin\xi. \tag{4.2.3}$$

The rotation angle ψ can now be expressed as

$$\sin\psi = \frac{\lambda_c}{2d^\star} - \zeta \tag{4.2.4}$$

where $\zeta = \tan\eta\,\tan\xi$ is a parameter describing the correction by non-perfect alignment of the λ-meter, and $d^\star = d\,\cos\eta\,\cos\xi\,/\,(1+w_H)$ is an instrumental parameter of the λ-meter which is determined in the experiment. The value of $d^\star$ should be close to the Si $(7\,7\,7)$ interplanar distance since the correction terms are ≈ 1.

With Eq. 4.2.1 one can also describe the behavior of the backscattering crystal. With the interplanar distance of the back-reflecting lattice planes $d_{(hkl)}$, and a small deviation from exact backscattering $\delta\theta = \pi/2 - \theta \ll 1$, Eq. 4.2.1 takes the form

$$\lambda_c = 2d_{(hkl)}\left[1 - \frac{(\delta\theta)^2}{2} - w_H\right]. \tag{4.2.5}$$

Because of the square dependence on $\delta\theta$, the change of the center of the spectral region is small even for rather coarse adjustment of exact backscattering; e.g. if $\delta\theta \approx 0.1\,\mathrm{mrad}$ then the change of the wavelength of the reflected radiation is only $5\times 10^{-9}\,\lambda_c$. This allows us to neglect this small correction in the following in many cases.

As pointed out on p. 20, w_H is assumed to be constant within the wavelength range covered by the experiment.

In the experiment we measure the rotation angle $\psi_{(hkl)}$ of the λ-meter at which it selects the x-ray wavelength matching the back-reflection $(h\,k\,l)$. From Eq. 4.2.4 and Eq. 4.2.5 one obtains

$$\sin\psi_{(hkl)} = 2x\,\tilde{d}_{(hkl)}(\tilde{a},\tilde{b},\tilde{c})\,[1 - w_H] - \zeta. \tag{4.2.6}$$

Herein,

$$x = \frac{\lambda_M}{2d^\star}; \tag{4.2.7}$$

and $\tilde{d}_{(hkl)} = d_{(hkl)}/\lambda_M$, $\tilde{a} = a/\lambda_M$, $\tilde{b} = b/\lambda_M$, and $\tilde{c} = c/\lambda_M$; where a, b, c are the three lattice parameters in the backscattering crystal. The tilde denotes the ratio between the respective length and the wavelength of the Mössbauer radiation of ^{57}Fe. The relation $\tilde{d}_{(hkl)}(\tilde{a},\tilde{b},\tilde{c})$ is determined by the crystal structure.

From Eq. 4.2.4 and Eq. 4.2.7, one can find another expression for the reference angle ψ_M where the λ-meter selects the wavelength of the Mössbauer radiation of ^{57}Fe,

$$\psi_M = x - \zeta. \tag{4.2.8}$$

In the difference $\Delta\psi_{(hkl)} = \psi_M - \psi_{(hkl)}$, the uncertainty about the zero-setting of the λ-meter drops out, and one obtains

$$\Delta\psi_{(hkl)} = \arcsin\left\{2x\tilde{d}_{(hkl)}(\tilde{a},\tilde{b},\tilde{c})\left[1-w_H\right]-\zeta\right\} - \arcsin(x-\zeta). \tag{4.2.9}$$

Herein $\Delta\psi_{(hkl)}$ is measured directly in the experiment, and $\tilde{a},\tilde{b},\tilde{c},x,\zeta$ are unknowns to be determined. Thus five independent measurements of $\Delta\psi_{(hkl)}$ are necessary to compute the five unknowns.

However, this number can be reduced under certain conditions. If the λ-meter is well aligned, i.e. $\eta < 10^{-2}$ and $\xi < 10^{-3}$, then $\zeta < 10^{-5}$. By numerical analysis of Eq. 4.2.9 it can be ascertained that in this case the results for the three lattice parameters do not change by more than 10^{-10}. The λ-meter in our experiments has been aligned even better by an auto-collimation method.

Furthermore, in the Si or $\alpha-$Al$_2$O$_3$ backscattering crystals, the three lattice parameters are not independent. In Si with its cubic symmetry, there is only one independent lattice parameter, i.e. $a = b = c$, and the interplanar distance is

$$d_{(hkl)} = \frac{a}{\sqrt{h^2 + k^2 + l^2}}. \tag{4.2.10}$$

In $\alpha-$Al$_2$O$_3$ there is a hexagonal symmetry, with $a = b$. For the hexagonal base we make use of the $(hkil)$ notation of the Miller indices where $h+k+i=0$, i.e. only three indices are independent. In this case, the interplanar distance reads

$$d_{(hkil)} = \frac{1}{\sqrt{\frac{4}{3a^2}(h^2 + k^2 + hk) + \frac{1}{c^2}l^2}}. \tag{4.2.11}$$

Thus, for Si the minimum number of independent measurements of $\Delta\psi_{(hkl)}$ is reduced to two, and for $\alpha-$Al$_2$O$_3$ to three.

The experimental technique relies on the strict fulfillment of the relations Eq. 4.2.10 or Eq. 4.2.11, respectively. This is the case for perfect crystals, but crystal defects may violate the periodicity of the crystal structure and thus the $d_{(hkl)}$ relations. Measuring $\Delta\psi_{(hkl)}$ for more than the minimum required number of independent back-reflections may validate the $d_{(hkl)}$ relations or give some hint on the errors in determination of the lattice constant.

Since the relative variation of λ_M is certainly below 10^{-11}, cf. Section 2.1, every subsequent measurement of ψ_M should lead—within a measurement accuracy of some nrad—to exactly the same result if the experimental setup is perfectly stable. In practice this was not the case. Thus we can determine from the variation of ψ_M from run to run the measurement uncertainty arising from setup instability. We can also check directly if additional precautions to improve the stability have the desired effect or not.

4.3. Results of the experiment at the 1 km beamline at SPring-8

In this section we will present the raw measurement data from the experiment conducted in February 2002 at the 1 km beamline (Ishikawa et al., 2001) at SPring-8, and describe in detail how the value for the wavelength of the Mössbauer radiation of ^{57}Fe is calculated from these data.

In all of the four experiments the same data evaluation method was used. The experiment from February 2002 should in principle lead to the most reliable result, not only due to the unique conditions at the 1 km beamline, but also due to the effort that has been taken to keep control over some error sources which showed up in the previous experiments. These technical improvements of the setup will be further discussed in Section 4.4.

In the experiment in February 2002, 10 *runs* of the measurement procedure have been performed. During one run, the Si reference crystal is aligned subsequently to the back-reflections (12 4 0), (9 7 5), and (9 9 1), and the angles $\psi_{(hkl)}$ at which the λ-meter selects the x-ray wavelength matching the respective back-reflections $(h\,k\,l)$ are recorded. The angle ψ_M where the λ-meter selects the wavelength of the Mössbauer radiation of ^{57}Fe is also measured.

For each back-reflection, the Si reference crystal is first adjusted to exact backscattering geometry. With a 0.2 mm aperture, the precision of this adjustment is $\delta\theta \approx 20\,\mu$rad. In this position, the intensity of the back-reflected beam is strongly reduced, and the energy distribution of the back-reflected beam may be slightly deteriorated, due to multiple beam diffraction in the Si reference crystal (see Section 2.3). Therefore, the aperture is removed after the first adjustment, and $\delta\theta$ is set 100 μrad off. The preferable direction of this offset with respect to the crystal axes was calculated beforehand for the respective back-reflections by Sutter (2001); see also Section 2.3. In this geometry, the unadvantageous effects of multiple beam diffraction almost disappear.

The temperature calibration and corrections which have been introduced in Sections 3.2.4.4 and 3.2.6 are applied in the following discussion and in the associated figures.

The angles $\psi_{(hkl)}$ measured in each run, with the Si reference crystal in backscattering geometry with 100 μrad offset, is shown in Figs. 4.3.1, 4.3.2, 4.3.3, together with the respective temperature setting of the Si reference crystal. The angles ψ_M from each run are displayed in Fig. 4.3.4.

Due to the limited time available for the experiment, $\psi_{(9\,9\,1)}$ has only been measured in the first 6 runs.

The data of run No. 3 have been discarded because in this run ψ_M was about 4 μrad off the averaged value from the other nine runs. The remaining values for ψ_M show a standard deviation of 1 μrad. This is caused by the mechanical instability of the experimental setup, since the uncertainty of the Mössbauer radiation wavelength of ^{57}Fe is below 10^{-11} and thus should not lead to any measurable variation of ψ_M.

The errorbars in Figs. 4.3.1 to 4.3.4 denote the width of the respective rocking curve.
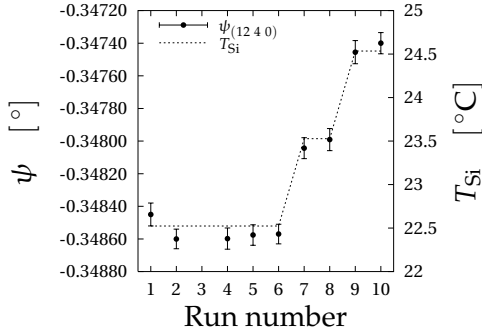
Fig. 4.3.1: Measurements of the angle $\psi_{(12\,4\,0)}$ where the λ-meter selects the back-reflected radiation of the (12 4 0) reflection of the Si *reference crystal (left axis), and temperature setting of the* Si *reference crystal (right axis)*
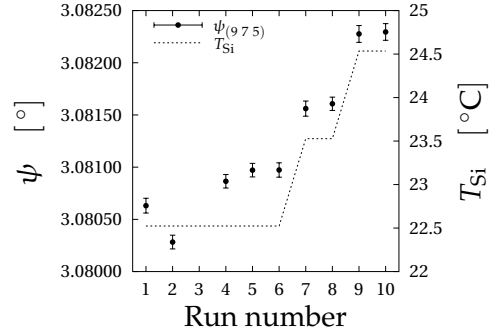
Fig. 4.3.2: Measurements of the angle $\psi_{(9\,7\,5)}$ where the λ-meter selects the back-reflected radiation of the (9 7 5) reflection of the Si *reference crystal, and temperature setting of the* Si *reference crystal*
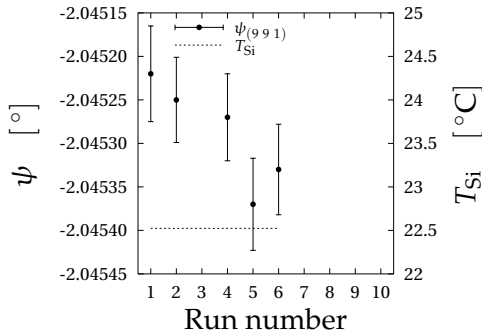
Fig. 4.3.3: Measurements of the angle $\psi_{(9\,9\,1)}$ where the λ-meter selects the back-reflected radiation of the (9 9 1) reflection of the Si *reference crystal, and temperature setting of the* Si *reference crystal*

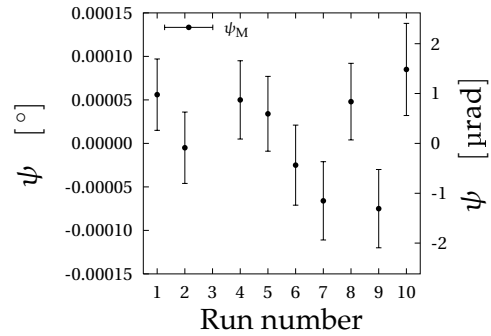*Fig. 4.3.4: Measurements of the angle ψ_M where the λ-meter selects the delayed Mössbauer radiation of the ^{57}Fe foil. The variation of ψ_M from run to run demonstrates the stability limits of the experimental setup. The errorbars denote the width of the λ-meter rocking curve.*

The ratio between the lattice parameter a_{Si} of the Si reference crystal and the wavelength of the Mössbauer radiation of ^{57}Fe can be calculated from a system of nonlinear equations like Eq. 4.2.9. Since in Si there is only one independent lattice parameter (i.e. $a = b = c$), and the λ-meter is aligned well enough (see p. 50), the number of unknowns to be determined is reduced to two: $\tilde{a}_{Si} = a_{Si}/\lambda_M$, and x. Thus, we need a system of two equations to determine λ_M. Since we have measured $\Delta\psi_{(hkl)}$ for three different back-reflections, we can put together three combinations of two equations of type Eq. 4.2.9 for each run.

We will first discuss the combination of the back-reflections (12 4 0) and (9 7 5), since this is the only one where we have experimental data for different temperatures of the Si reference crystal. In Fig. 4.3.5 the results for a_{Si}/λ_M—calculated for each run—are shown together with the temperature setting of the Si reference crystal.

Fig. 4.3.5: Ratio between lattice parameter of Si reference crystal and wavelength of the Mössbauer radiation of ^{57}Fe, calculated for each run from $\psi_{(12\,4\,0)}$ and $\psi_{(9\,7\,5)}$ (left axis); and temperature setting of the Si reference crystal (right axis)

Fig. 4.3.6: Ratio between lattice parameter of Si reference crystal and wavelength of the Mössbauer radiation of ^{57}Fe, averaged from the results from $\psi_{(12\,4\,0)}$ and $\psi_{(9\,7\,5)}$ for runs at the same temperature. The solid line is a linear fit. The dotted line denotes the reference temperature of $22.500\,^{\circ}$C for which a_{Si} is precisely known.

The width of the errorbars is determined by the uncertainty of the measured values of $\psi_{(hkl)}$ and ψ_M, which has been assumed to be 0.25 times the width of the respective rocking curve.

For subsequent runs at the same temperature of the Si reference crystal, averaged values of $\tilde{a}_{Si} = a_{Si}/\lambda_M$ have been calculated which are shown in Fig. 4.3.6. A linear fit of the form

$$\tilde{a}_{Si}(T) = \tilde{a}_0 + \tilde{\rho} \cdot (T - T_0) \tag{4.3.1}$$

[h k l] has been applied to these three data points. Here, $T_0 = 22.500\,°\text{C}$ is the reference temperature for which the lattice parameter of the WASO04 Si reference crystal has been precisely measured as

$$a_0 = 5.431\,020\,26(34)\ \text{Å} \tag{4.3.2}$$

beforehand at the PTB by Becker (2007). The following fit parameters were found:

$$\tilde{\rho}_0 = 6.313\,262\,36(19) \tag{4.3.3}$$

$$\tilde{\rho} = 0.000\,018\,8(16)\ \text{K}^{-1} \tag{4.3.4}$$

This leads to the determination of the wavelength of the Mössbauer radiation of ^{57}Fe by

$$\lambda_\text{M} = \frac{a_0}{\tilde{a}_0} = 0.860\,255\,75(26)\ \text{Å} \quad \text{for} \quad (12\ 4\ 0),(9\ 7\ 5). \tag{4.3.5}$$

For the other possible combinations of the back-reflections a slightly different approach has to be used, since $\psi_{(9\,9\,1)}$ has only been measured for a single temperature of the Si reference crystal, $T = 22.525\,°\text{C}$. The values of $a_\text{Si}/\lambda_\text{M}$ which have been calculated for each run from the back-reflections (12 4 0) and (9 9 1) are shown in Fig. 4.3.7, and the values from (9 7 5) and (9 9 1) in Fig. 4.3.8.
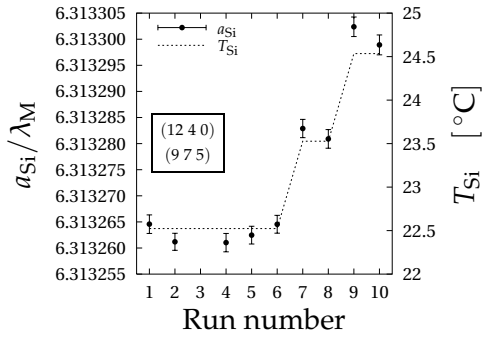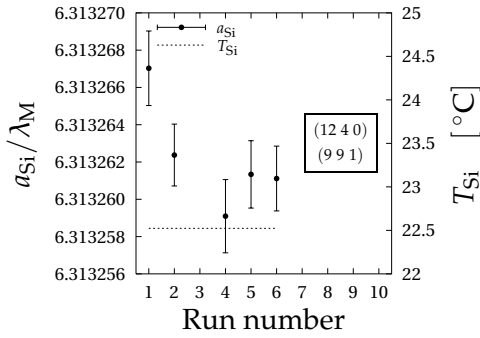

Fig. 4.3.7: Ratio between lattice parameter of Si *reference crystal and wavelength of the Mössbauer radiation of* ^{57}Fe, *calculated for each run from* $\psi_{(12\,4\,0)}$ *and* $\psi_{(9\,9\,1)}$; *and temperature setting of the* Si *reference crystal*
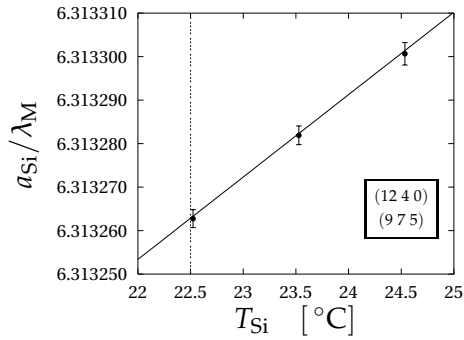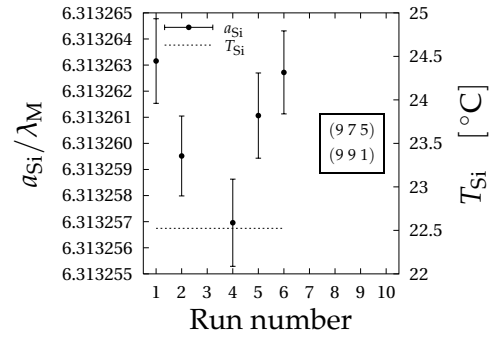
Fig. 4.3.8: Ratio between lattice parameter of Si *reference crystal and wavelength of the Mössbauer radiation of* ^{57}Fe, *calculated for each run from* $\psi_{(9\,7\,5)}$ *and* $\psi_{(9\,9\,1)}$; *and temperature setting of the* Si *reference crystal*

For both combinations an averaged value for $\tilde{a}_\text{Si}$ can be computed:

$$\tilde{a}_\text{Si}(T) = 6.313\,262\,2(21) \quad \text{for} \quad (12\ 4\ 0),(9\ 9\ 1) \tag{4.3.6}$$

$$\tilde{a}_\text{Si}(T) = 6.313\,260\,6(19) \quad \text{for} \quad (9\ 7\ 5),(9\ 9\ 1). \tag{4.3.7}$$

We write Eq. 4.3.1 in the form

$$\tilde{a}_0 = \tilde{a}_{Si}(T) - \tilde{\rho} \cdot (T - T_0) \tag{4.3.8}$$

and insert the $\tilde{a}_{Si}(T)$ values from Eqs. 4.3.6, 4.3.7, respectively, while $\tilde{\rho}$ is taken from Eq. 4.3.4. This leads to

$$
\begin{aligned}
\tilde{a}_0 &= 6.313\,261\,7(21) &\quad \text{for} \quad & (12\ 4\ 0),(9\ 9\ 1) & (4.3.9) \\
\tilde{a}_0 &= 6.313\,260\,2(19) &\quad \text{for} \quad & (9\ 7\ 5),(9\ 9\ 1). & (4.3.10)
\end{aligned}
$$

As in Eq. 4.3.5, the Mössbauer radiation wavelength of ^{57}Fe can now be computed to

$$
\begin{aligned}
\lambda_M &= 0.860\,255\,83(29)\,\text{Å} &\quad \text{for} \quad & (12\ 4\ 0),(9\ 9\ 1) & (4.3.11) \\
\lambda_M &= 0.860\,256\,04(27)\,\text{Å} &\quad \text{for} \quad & (9\ 7\ 5),(9\ 9\ 1) \quad , & (4.3.12)
\end{aligned}
$$

respectively. The final result for the wavelength of the Mössbauer radiation of ^{57}Fe is determined as the average of the three results from the different combinations of back-reflections:

$$\lambda_M = 0.860\,255\,87(26)\,\text{Å}. \tag{4.3.13}$$

The relative error in this result is 3×10^{-7}. It is mostly attributed to the measurement uncertainty and the scattering of the raw data for ψ_M and $\psi_{(hkl)}$. Other important error sources which are included in Eq. 4.3.13 are the uncertainties of a_0 and T. These are, however, comparably small: $\delta a_0 / a_0 = 6.3 \times 10^{-8}$ (cf. Eq. 4.3.2); and $\delta T \approx 0.01$ K, which leads with a linear thermal expansion of Si of about 2.6×10^{-6} K^{-1} (Mohr and Taylor, 2000) to an additional uncertainty of 2.6×10^{-8}.

Our result agrees quite well with the value reported by Xiaowei et al. (2000): $\lambda_M = 0.860\,255\,7(5)$ Å. The uncertainty of our result is about two times smaller. However, we find some inconsistency between Eq. 4.3.13 and the value we have reported earlier as a result of an experiment at APS where the same method was used: $\lambda_M = 0.860\,255\,474(16)$ Å (Shvyd'ko et al., 2000). This requires some more in-depth discussion of the technical details and the changes and improvements which have been made between the experiments at APS and SPring-8—see Section 4.4.

From Eqs. 4.3.1 to 4.3.4 it is possible to derive the linear thermal expansion coefficient of the Si reference crystal by $\rho = \tilde{\rho}/\tilde{a}_0 = 2.99(26) \times 10^{-6}$ K^{-1}. Due to the measurement uncertainties in ψ and the narrow temperature range covered, this result has a quite large relative error of about 9%. Unfortunately, our result for ρ disagrees with other results of high-precision experiments on the lattice spacing and the thermal expansion of Si, where $\rho = 2.581(2) \times 10^{-6}$ K^{-1} has recently been reported by Bergamin et al. (1997) (see also e.g. Becker et al. (1981); Bergamin et al. (1999); Mohr and Taylor (2000)). We have to accept this as a hint on some remaining systematic error in our experimental procedure. The investigation of the temperature distribution inside the oven and along the Si (7 7 7) channel-cut crystal, which is described

in the sections 3.2.6 and 3.2.7, was in fact motivated by the search for such an error. However, with special regard to the measurement of ρ it did not lead to any considerable change. Thus, the discrepancy between our value for ρ and the results of precision measurements by Bergamin et al. (1997) and others is an evidence for some remaining problem in the realization of the experimental method, which cannot be understood only by the temperature measurements.

4.4. Historical background and improvements of the setup

The experiment for measurement of the wavelength of the Mössbauer radiation of ^{57}Fe was conducted four times in the years from 1998 to 2002, at different synchrotron radiation facilities. The first experiment in 1998 was performed at the wiggler beamline BW4 at HASYLAB. Here the experimental method was verified, but the uncertainty of the result was limited to $\gtrsim 10^{-6}$ due to large beam divergence $12(2)\,\mu\mathrm{rad}$ and low count rate of Mössbauer photons $5\,\mathrm{Hz}$. Since the method should be able to produce an accuracy better than 10^{-7}, the experiment was carried out a second time in 1999 at the undulator beamline 3-ID at APS. Here it was possible to work with $4.5\,\mu\mathrm{rad}$ beam divergence and $100\,\mathrm{Hz}$ count rate for Mössbauer photons. The result for the wavelength of the Mössbauer radiation of ^{57}Fe

$$\lambda_{\mathrm{M}} = 86.025\,474\,(16)\,\mathrm{pm} \qquad (4.4.1)$$

has a relative accuracy of 1.9×10^{-7}. The results from HASYLAB and APS have been reported by Shvyd'ko et al. (2000).

We expected, however, that it should be possible to get an even better accuracy. Beyond that, there was some disagreement between our result Eq. 4.4.1 and another result reported by Xiaowei et al. (2000): $\lambda_{\mathrm{M}} = 86.025\,57\,(5)\,\mathrm{pm}$. The error ranges of both results do not overlap although they are about 5 orders of magnitude broader than the natural reproducibility of λ_{M}. Thus it seems clear that at least one of these reported experiments suffers from some undiscovered systematical errors.

Therefore we have repeated the experiment in 2001 at the beamline BL29XUL at SPring-8. This beamline is unique in the world since it provides a distance between radiation source and experimental setup of about $1\,\mathrm{km}$ (Ishikawa et al., 2001). Thus it is easily possible to cut down the beam divergence to $\approx 1\,\mu\mathrm{rad}$ by using two $1\,\mathrm{mm}$ slits with a distance of $950\,\mathrm{m}$, independent from the x-ray energy.

For this experiment there have also been made some other improvements: As Si reference crystal, a special sample was prepared by the PTB. It is part of the WASO04 reference crystal which has a precisely determined lattice parameter (Becker, 2001):

$$a_0 = 543.102\,026\,(34)\,\mathrm{pm} \text{ at } T = 22.5\,^{\circ}\mathrm{C} \text{ in vacuum.} \qquad (4.4.2)$$

In the experiments before, another high-quality Si sample from the PTB was deployed as the reference crystal. Its lattice constant

$a = 5.431\,020\,30(36) \times 10^{-10}\,\mathrm{m}$ has been calibrated against the Si standard crystal (Becker et al., 1981) with a relative uncertainty of 7×10^{-8} at $22.5\,°\mathrm{C}$ in vacuum.

Furthermore, the sample from the WASO04 Si reference crystal was manufactured in a special outer shape that fits well into the oven, thus eliminating the need for an additional sample holder which might deteriorate the thermal contact between oven and crystal. The gap of several $100\,\mathrm{\mu m}$ between oven shell and crystal was filled with heat-conductive compound. The same was used between the oven body and front cap, and between the cap and the window which is made of aluminum foil. The temperature measurement system was completed by a pair of thermocouples, where one of them was placed on the Si reference crystal surface, $\approx 5\,\mathrm{mm}$ off the center (pos. [1] in Fig. 3.2.1), and another one close to the PT100 (pos. [2] in Fig. 3.2.1). These were used to check if the temperature of the PT100 and of the crystal surface are the same. The thermocouple wires run through a narrow groove in the cap into the interior of the oven. The groove also ensures that the oven is evacuated together with the outer vacuum tank.

The deviation from exact backscattering was decreased from $0.3\,\mathrm{mrad}$ at the APS experiment to $0.1\,\mathrm{mrad}$ at SPring-8. There are some unfavorable azimuthal directions for the deviation, where the multiple beam diffraction effects are still large for $\delta\theta = 0.1\,\mathrm{mrad}$, as discussed in Section 2.3. Therefore, Sutter (2001) has calculated in advance the azimuthal directions which are favorable and those which are not (cf. Tab. 2.3.1), and in the experiment the deviation from exact backscattering was adjusted according to these considerations.

The refractive correction w_H in Eq. 2.2.60 contains a dependence on the so-called asymmetry parameter $b = -\sin(\theta - \eta)/\sin(\theta + \eta)$ with the Bragg angle θ and the angle η between the reflecting lattice planes and the crystal surface. We have estimated that the uncertainty in the refractive correction introduced by b may significantly deteriorate the accuracy of the measurement results for the Si $(7\,7\,7)$ reflection if $\eta > 0.25\,\mathrm{mrad}$ for $\theta \approx 74\,°$. The silicon channel-cut crystal was therefore specially prepared to keep the angle η below $0.2\,\mathrm{mrad}$. The refractive correction term δ in Eq. 4.2.5 is not affected by such a consideration because $b = -1$ for exact backscattering.

The cylindrical thermal insulating cap on the λ-meter holder was improved by replacing the $2\,\mathrm{mm}$ foam layer with $25\,\mathrm{mm}$ of another foam with higher density, and adding a thin aluminum foil to the inner side of the cap. The Si $(7\,7\,7)$ channel-cut crystal was fixed on the holder with a drop of beeswax.

With the reduced beam divergence of $\lesssim 0.1\,\mathrm{mrad}$ at the $1\,\mathrm{km}$ beamline it was, in the experiment from 2001, easily possible to narrow down the angular width of the ψ_M measurements to $0.9\,\mathrm{\mu rad}$. This is even below the theoretical intrinsic width of $1.2\,\mathrm{\mu rad}$ of the Si $(7\,7\,7)$ reflection. The reason for this behavior is not fully understood. Unfortunately, the reproducibility of ψ_M from one run to another was worse than the beam divergence: the ψ_M values measured in 15 subsequent runs were scattered within a $7\,\mathrm{\mu rad}$ interval, cf. Fig. 4.4.1 on p. 59. Therefore, a result more accurate than given in Eq. 4.4.1 could not be obtained from these data.

Possible reasons are instabilities either in mechanics or in temperature. A problem with temperature alone is however unlikely, since the change of the Bragg angle with temperature is $d\theta/dT = -8.83\,\mu\text{rad}\,\text{K}^{-1}$ for the Si $(7\,7\,7)$ reflection. Thus a temperature drift of 0.8 K would be required to change ψ_M by 7 μrad. This should not happen because the λ-meter was precisely temperature controlled and well insulated. The mechanical strength of the λ-meter crystal holder was however identified as the most likely weak spot. This gave reason to a new construction of this part with improved strength (see Fig. 3.2.3). Also an aluminum clamp was added to the crystal support which should allow better fixation without applying too much mechanical stress to the crystal.

The PT100 was moved from the copper plate into a groove in the Si $(7\,7\,7)$ channel-cut crystal to allow even more precise control of the crystal's temperature itself. A pair of thermocouples was installed on the faces of the channel-cut crystal, at the positions denoted in Fig. 3.2.3, to check for temperature differences between them. By additional table-top experiments the temperature distribution inside the λ-meter was further analyzed, as described in Section 3.2.7. It was found that with thin insulation and too high temperature setpoint there is some risk of remarkable temperature gradients within the faces of the channel-cut crystal. Such temperature gradients do not only shift the wavelength and angle of the two $(7\,7\,7)$ reflections against each other, but impose also the risk of mechanical stress in the crystal, at the point where the beam is reflected, due to thermal expansion. This could violate the assumption that the transmitted beam is parallel to the incident beam. According to the estimation above, this is probably only a small but considerable contribution to the instability of ψ_M.

With respect to the thermal behavior of the λ-meter setup the recommendation for operation is as follows: If possible, i.e. the ambient temperature does not drift by more than $\approx 10\,\text{mK}$, the λ-meter should be operated with no temperature control but in equilibrium with its environment. If the ambient temperature stability is not that good, the setpoint of the temperature control should be no more than $\approx 0.5\,\text{K}$ above the environmental temperature.

Anyway, it is difficult to tell which part of the experiment is really stable enough if it depends on microradians, even if everything is carefully selected to be as solid and accurate as possible. So we have to consider also some other parts of the setup as error sources. These include but are not limited to the measurement accuracy of the λ-meter goniometer and encoder, the mechanical stability of those devices or the tables where they are mounted on, and even the stability of the ground where the beamline is built on.

After having improved the λ-meter support and temperature measurement, the experiment was conducted a second time at the 1 km beamline at SPring-8 in the year 2002. Here also some investigations and improvements have been made in the meantime. The long-term stability of the λ-meter goniometer and encoder have been measured by Tamasaku (2002). The air-conditioning in the experimental station was set to 26.5 °C, and in the surrounding beamline building to 25 °C. After closing the doors of the experimental station, a drift of the encoder reading of about -4.8 μrad was observed within one day. This shows that opening and closing the doors, which is an
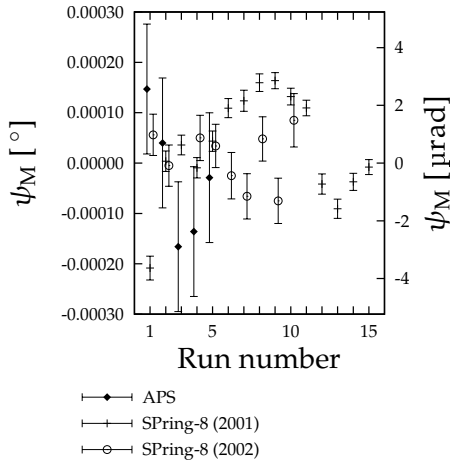
^{57}Fe
APD
Detector
Oven
22.5 °C
Si reference crystal
[1 1 0]
[h k l]
ψ
X-rays
$2\delta\theta$
50
987
988
from the undulator [m]
line BL29XUL at SPring-8
993

Fig. 4.4.1: Comparison of the scattering of the angle ψ_M where the λ-meter selects the delayed Mössbauer radiation from the ^{57}Fe foil between the experiments at APS (Shvyd'ko et al., 2000) and the two experiments at SPring-8 in 2001 and 2002. Ther errorbars denote the width of the rocking curve of the λ-meter.

unavoidable operation in such an experiment, may have a considerable effect on the λ-meter's reproducibility.

Therefore we have decided to operate the air-conditioners of both the experimental station and the beamline building at the same temperature, 25 °C. Thus the temperature shifts introduced by opening the doors and entering the station should be minimized. The stated accuracy of the temperature control of the air-conditioner in the experimental station is 0.1 K. It would also be a good idea to wait some hours with the continuation of the experiment after closing the door, but in practice the tight schedule does not allow this.

We have also minimized the temperature gradient between the oven and its chilled vacuum tank. In the previous experiments the temperature of the chilling water was about 5 °C, since at APS there was a facility-wide chilling water supply with no temperature control available. In the experiment at SPring-8 in 2002, the temperature setpoint of the chilling water was 4.5 K below the setpoint of the Si reference crystal, i.e. 18 °C for the water if the Si reference crystal is at 22.5 °C. This temperature difference is, by experimental analysis, the lowest where the temperature controller was operating stable. With changes of the Si reference crystal temperature the chilling water temperature was adapted to keep the difference. Due to the length of the water pipes between cooling system and vacuum tank, the temperature difference between vacuum tank and oven was probably even lower than 4.5 K.

With the new setup in the 2002 experiment, the measured values of ψ_M from 9 subsequent runs are now scattered within a 2.8 µrad interval. This is about 2 times narrower than before at the APS experiment, and about 2.5 times narrower than at the first SPring-8 experiment in 2001. In Fig. 4.4.1 the scattering of ψ_M from run to run in the APS experiment and the two experiments at SPring-8 is compared.

However, due to the scattering of the $\psi_{(hkl)}$ measurements, and the fact that data for the (9 9 1) back-reflection were not available for different temperatures of the Si reference crystal, the overall uncertainty of the result for the wavelength of the Mössbauer radiation of ^{57}Fe Eq. 4.3.13 is not better than in the result from Shvyd'ko et al. (2000). Furthermore, the discrepancy between
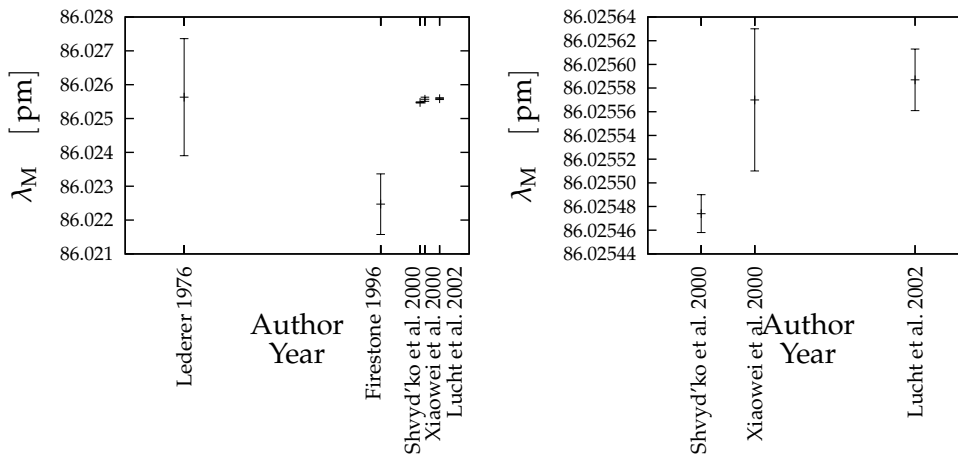
X-rays   987

$2\delta\theta$

50   988
          Distance from the undulator [m]
987
      at the beamline BL29XUL at SPring-8

                        993
988**60**   *CHAPTER 4. MEASUREMENTS OF THE WAVELENGTH OF THE MÖSSBAUER RADIATION OF* ^{57}*FE*

nce from the undulator [m]
eamline BL29XUL at SPring-8

993

Fig. 4.5.1: Updated historical overview of the measured results for the Mössbauer radiation wavelength of ^{57}Fe*, including the new result from SPring-8 in 2002, which is labeled "Lucht et al. 2002" according to the time of measurement—it is, however, reported first in the present thesis. The right panel shows only the recent results which were obtained with synchrotron radiation.*

our result for the thermal expansion coefficient of Si and other precision measurements, discussed on p. 55, is an evidence that the result in Eq. 4.3.13 is of limited reliability, and that the realization of the method does still need more improvement.

4.5.   Conclusion

The updated history of measurements of the wavelength of the Mössbauer radiation of ^{57}Fe is shown in Fig. 4.5.1. The results from Shvyd'ko et al. (2000); Xiaowei et al. (2000) and from the present report are a remarkable improvement over previously published values.

Obviously, there is some disagreement left between the recently reported values which were obtained using synchrotron radiation. In the experimental method discussed in the present report, there are still some open issues regarding the stability of the λ-meter, both in temperature and in angular setting; and also regarding the discrepancy of the measurement of the linear thermal expansion coefficient by our most recent experiment and by other precision experiments.

The linear thermal expansion coefficient could probably be better analyzed if a larger temperature range were chosen, and possible problems with temperature stability could be avoided by longer settling times. Apart from that, improving the experimental technique significantly over the current state seems very difficult and expensive. Therefore, up to now no attempt has been made to gain more accurate measurements using the same method, although an im-

provement of about one order of magnitude should be possible if everything were perfect.

Our method is finally limited by the underlying length standard, the lattice parameter of Si, which will probably never be more accurately known than 10^{-9} (Bergamin et al., 1999). An improvement beyond that may become possible by another method which is currently under development: A combined x-ray Fabry-Pérot resonator for x-ray and optical wavelengths, measuring the wavelength of the Mössbauer radiation of ^{57}Fe in units of the wavelength of an optical He-Ne laser which has an accuracy and stability of about 10^{-12}. See Section 6.3 for more details, and also Shvyd'ko (2002, 2004); Shvyd'ko et al. (2003).

Chapter 5

Applications

With the wavelength of the Mössbauer radiation of ^{57}Fe a new length standard for the measurement of lattice parameters in single crystals, or of wavelengths in the Å range, has been introduced. In this chapter, we will present two further experimental works carried out by our research group, which are the first applications of the new length standard. These are:

- The measurement of the lattice parameters of $\alpha-Al_2O_3$ in the temperature range from 4.5 K to 374 K. These are of special interest for the design of forthcoming backscattering x-ray monochromators and resonators. Here, precise knowledge of the lattice parameters and their temperature dependence is required to predict the Miller indices of back-reflections and the relevant temperature of the backscattering crystal to tune the energy of the reflected beam to any energy in the $10 \ldots 50$ keV range. While previously reported lattice parameters of sapphire differ by more than 10^{-4}, our measurements with the Mössbauer wavelength standard provide an uncertainty of 10^{-6}.

- The measurement of the wavelengths of the Mössbauer radiation of other isotopes: ^{119}Sn, ^{151}Eu, and ^{161}Dy, with sub-ppm accuracy. Together with the wavelength of the Mössbauer radiation of ^{57}Fe these provide a set of four reference wavelengths in the hard x-ray region with uniquely small uncertainty and easy reproducibility. The measurement of the wavelength of the Mössbauer radiation is complementary to the measurement of lattice parameters of $\alpha-Al_2O_3$, and has been carried out in the same experiment. By selecting an appropriate back-reflection and tuning the temperature, the wavelength of the back-reflected beam, and thus the interplanar distance in the $\alpha-Al_2O_3$ crystal, is adjusted to match the wavelength of the Mössbauer radiation to be measured. Then the lattice parameters are measured at the same temperature, allowing to calculate the interplanar distance of the reflecting atomic planes, and thus the wavelength of the Mössbauer radiation.

Our measurements of the lattice parameters of $\alpha-Al_2O_3$ in the temperature range from 286 K to 374 K, and the wavelength of the Mössbauer radiation of ^{119}Sn, ^{151}Eu, and ^{161}Dy, have been published by Shvyd'ko et al. (2002). The measurements of the lattice parameters in the temperature range from 4.5 K to 250 K are reported by Lucht et al. (2003).

In the following we will describe the experimental setup and the data evaluation procedures for these measurements, as far as they are different from the experiment for the measurement of the wavelength of the Mössbauer radi-

ation of ^{57}Fe which has already been discussed in Chapter 4. The results will also be presented and discussed.

5.1.   Measurement of the lattice parameters of sapphire

5.1.1.   Motivation

The knowledge of the lattice parameters of $\alpha-Al_2O_3$ is of interest because $\alpha-Al_2O_3$ is potentially a new material for x-ray crystal optics, especially attractive in applications as Bragg backscattering mirrors for interferometers, high-energy resolution monochromators, and analyzers, since it allows (unlike silicon, cf. Section 2.3) *exact* Bragg backscattering with high reflectivity for x rays in the $10-50$ keV spectral range (cf. Shvyd'ko, 2004; Shvyd'ko and Gerdau, 1999; Shvyd'ko et al., 1998).

Precise values of the sapphire lattice parameters and their temperature dependences are required to select suitable back-reflections and relevant crystal temperatures for work with desired x-ray energies. However, the lattice parameters of $\alpha-Al_2O_3$ previously reported by Aldebert and Traverse (1982); Brown et al. (1992); Burghartz and Schulz (1994); Kirfel and Eichhorn (1990); Lewis et al. (1982); Yim and Paff (1974) differ by more than 10^{-4}. This imposes large uncertainties in the prediction of the back-reflections and the relevant crystal temperatures. To ensure more precise predictions, the lattice parameters of $\alpha-Al_2O_3$ have been measured with a relative uncertainty of less than 6×10^{-6} in the temperature range from 4.5 K to 374 K.

The temperature region below 250 K is of special interest for x-ray backscattering because—compared to room temperature and above—the thermal expansion of $\alpha-Al_2O_3$ is lower, leading to less strict requirements for the stability of the temperature control for the crystals which are used as x-ray optical elements. This is especially important for x-ray energies above ≈ 30 keV, since with higher energy the bandpass of the back-reflections becomes narrower and the extinction depth increases. This leads to a required temperature stability which cannot be fulfilled with the thermal expansion of $\alpha-Al_2O_3$ at room temperature.

Also the thermal conductivity of $\alpha-Al_2O_3$ rises at low temperature, making $\alpha-Al_2O_3$ a potential material for high-heat-load monochromators for synchrotron radiation. The thermal conductivity measured in $\alpha-Al_2O_3$ is up to $200 \, W \, cm^{-1} \, K^{-1}$ around 30 K (Touloukian and Ho, 1970), which is higher than the thermal conductivity of any other mono-crystalline material suitable for x-ray optics. For temperatures above 100 K the thermal conductivity of $\alpha-Al_2O_3$ drops below $5 \, W \, cm^{-1} \, K^{-1}$. The unique combination of high thermal conductivity and low thermal expansion of $\alpha-Al_2O_3$ at ≈ 30 K may become important at the synchrotron radiation facilities of the fourth generation (XFEL, LCLS) which are currently under development, since such sources will provide a beam intensity and heat load that is several orders of magnitude higher compared with today's facilities.

Another important application of $\alpha-Al_2O_3$ which depends on its low thermal expansion at low temperature, are cryogenic optical resonators (CORE)

with ultra-stable frequency in the optical range (Seel et al., 1997). Such devices have recently been used, e.g., in the most accurate verification of special relativity (Braxmaier et al., 2001).

5.1.2. Introduction

The experimental method that was used to measure the lattice parameters of $\alpha-Al_2O_3$ is very similar to the technique that was used to measure the wavelength of the Mössbauer radiation of ^{57}Fe (see Chapter 4). The differences are, first, that the Si reference crystal is now replaced by the $\alpha-Al_2O_3$ crystal under study, and second, that the complementary problem has to be solved: to determine the unknown lattice parameters in terms of the known wavelength. The crystal structure of $\alpha-Al_2O_3$ can be described by a hexagonal structure with two independent lattice parameters a and c. For symmetry reasons, in the hexagonal structure the Bragg reflections are denoted by four indices $(h\,k\,i\,l)$. Obviously, only three of the indices are independent, and the relation $h + k + i = 0$ is always valid.

Since there are now two independent lattice parameters, the number of unknowns to determine by the experiment, and thus the number of necessary independent measurements of $\psi_{(h k i l)}$, is increased by one compared to the case of Si. In the data evaluation, we have to solve a nonlinear system of three equations of type Eq. 4.2.9, with $\delta\theta < 100\,\mu\text{rad}$, $\zeta \approx 0$ (see p. 50), and $\tilde{a} = \tilde{b}$ (see Eq. 4.2.11) for the unknown parameters $\tilde{a}, \tilde{c}, x$. In $\tilde{a} = a/\lambda_M$ and $\tilde{c} = c/\lambda_M$ we presume λ_M as known from our other experiments (see Chapter 4 and Shvyd'ko et al. (2000)) and are thus able to compute a and c in SI units.

Thus, one run of the measurement of the lattice parameters requires measurements of ψ_M, and $\psi_{(h k i l)}$ for at least three different back-reflections $(h\,k\,i\,l)$. Four back-reflections were selected for the experiment by their Bragg wavelength $\lambda_B = 2d_{(h k i l)}(1 - w_H)$ being in the proximity of λ_M. They are listed in Tab. 5.1.1.

| $(h\,k\,i\,l)$ | λ_B | $\widehat{[000\overline{1}][hkil]}$ | $\widehat{[10\overline{1}0][hkil]}$ | ΔE |
	[pm]	[°]	[°]	[meV]
$(0\,0\,0\,30)$	86.60572	0.0	0.0	13.2
$(1\,6\,\overline{7}\,22)$	86.07066	43.2162	52.4109	1.8
$(1\,3\,\overline{4}\,21)$	85.97935	22.0934	46.1021	6.1
$(2\,6\,\overline{8}\,20)$	85.81588	48.6577	46.1021	4.5

Tab. 5.1.1: Miller indices $(h\,k\,i\,l)$ of selected back-reflections in $\alpha-Al_2O_3$ with Bragg wavelengths $\lambda_B = 2d_{(h k i l)}(1 - w_H)$ close to λ_M. The λ_B values are calculated by using the lattice parameters at $T = 287.3\,\text{K}$ as obtained in the experiment at APS (Shvyd'ko et al., 2002). The angular deviation of the diffraction vector from the main crystallographic directions, as well as the expected theoretical energy widths of the back-reflections are also shown.

The hexagonal structure of $\alpha-Al_2O_3$ is less symmetric than the cubic structure of Si, leading to a less frequently occurence of multiple beam diffraction

988
nce from the undulator [m]
eamline BL29XUL at SPring-8

993

in backscattering geometry. As pointed out by Lerche and Shvyd'ko (2004), for the $(1\,3\,\overline{4}\,21)$ back-reflection we have a four beam case, but the excitation of the parasitic reflections can be easily suppressed by a deviation of only $12\,\mu\mathrm{rad}$ from the exact backscattering condition.

5.1.3. Experimental setup for the measurement of lattice parameters

The experiment was carried out at two synchrotron radiation facilities, APS and PETRA. Due to the large temperature range to be covered, two different thermostat devices, an oven and a cryostat, were used for the $\alpha-\mathrm{Al_2O_3}$ crystal. The setup, which is basically the same as for the measurement of the wavelength of the Mössbauer radiation of $^{57}\mathrm{Fe}$ is shown in Fig. 5.1.1.
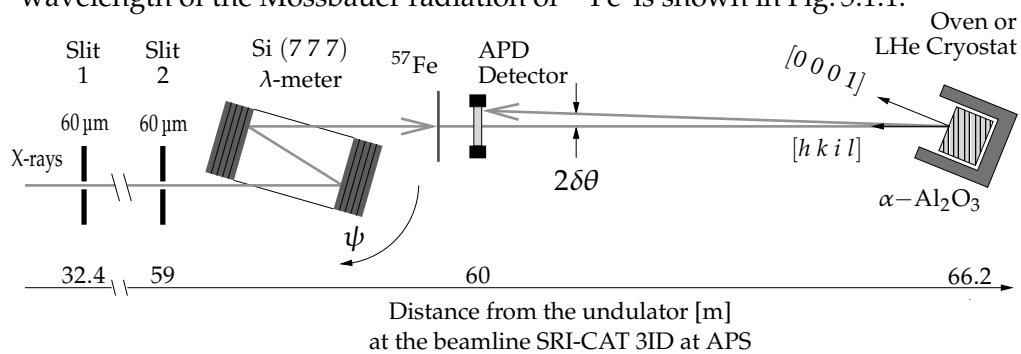

Fig. 5.1.1: Setup for the experiment to measure the lattice parameters of $\alpha-\mathrm{Al_2O_3}$ in units of the wavelength of the Mössbauer radiation of $^{57}\mathrm{Fe}$.

The measurements in the range from $286\,\mathrm{K}$ to $374\,\mathrm{K}$ (Shvyd'ko et al., 2002) were taken at the SRI-CAT 3ID beamline at APS. The $\alpha-\mathrm{Al_2O_3}$ was kept in an oven similar to the one that was used for the measurements of the wavelength of the Mössbauer radiation of $^{57}\mathrm{Fe}$ (see Fig. 3.2.1). The $\alpha-\mathrm{Al_2O_3}$ crystal has the shape of a disc with $15\,\mathrm{mm}$ diameter and $1\,\mathrm{mm}$ thickness. It was grown by the heat-exchange method (Schmid et al., 1994). The dislocation density in the sample was measured to be $4\times10^3\,\mathrm{cm^{-2}}$ with white-beam backscattering x-ray topography (Chen et al., 2001; Tuomi et al., 1974).

The $\alpha-\mathrm{Al_2O_3}$ sample was adapted to the oven with a specially designed sample holder. To maintain a good thermal contact between oven and crystal, and to keep temperature gradients low, the oven was filled with air at room pressure and closed with a vacuum-tight cap. Thus the air remains in the oven when the surrounding vacuum tank is evacuated. The oven is operated with a temperature control which allows to maintain the crystal at a fixed temperature with a stability of $\approx1\,\mathrm{mK}$ (Lucht, 1998). See also Chapter 3 for details on temperature measurement and control.

In the experiment at APS, a total of 13 runs of the experiment was performed at different temperature settings of the $\alpha-\mathrm{Al_2O_3}$. The temperature settings were partly determined by the measurement of the wavelengths of the Mössbauer radiation of $^{119}\mathrm{Sn}$, $^{151}\mathrm{Eu}$, and $^{161}\mathrm{Dy}$, which was in fact a part of same experiment, but will be discussed later in Section 5.2.

The measurements from 4.5 K to 250 K (Lucht et al., 2003) were performed at the PETRA-1 beamline, which is one of two synchrotron radiation beamlines at the single undulator at the PETRA-II storage ring at HASYLAB (cf. Franz et al., 2000; Hahn et al., 1997; Kracht et al., 1995). The $\alpha-Al_2O_3$ sample was installed in the cryostat described in Section 3.2.2. Five runs of the experiment were made with the $\alpha-Al_2O_3$ kept at temperatures of 250 K, 200 K, 150 K, 100 K, and 4.5 K.

This method allows absolute measurement of the lattice parameters a and c in units of λ_M. For a change of the back-reflection of the $\alpha-Al_2O_3$ or the x-ray wavelength transmitted by the λ-meter the goniometers have to be moved over large angular distances. However, the movements of the goniometers are very slow, and so the procedure takes up a great deal of time.

Therefore, in the range from 100 K to 4.5 K a technique of relative measurements was used additionally. It allows a faster data acquisition with smaller temperature steps. The relative change of the inter-planar distance $d_{(0\,0\,0\,30)}$ was measured by using the $(0\,0\,0\,30)$ back-reflection. Beginning at 100 K, the $\alpha-Al_2O_3$ temperature was changed in steps of $\Delta T = -5$ K. For each temperature step, the angle $\psi(T)$ where the λ-meter transmits the back-reflected radiation is recorded. This procedure is repeated with the $\alpha-Al_2O_3$ at the $(1\,6\,\overline{7}\,22)$ back-reflection to determine the relative change of the inter-planar distance $d_{(1\,6\,\overline{7}\,22)}$. The change $\Delta d_{(hkil)}(T) = d_{(hkil)}(T) - d_{(hkil)}(100\,K)$ against the absolutely measured inter-planar distance at 100 K is calculated from the corresponding change in the angle of the λ-meter $\Delta\psi_{(hkil)}(T) = \psi_{(hkil)}(100\,K) - \psi_{(hkil)}(T)$ by

$$\Delta d_{(hkil)}(T) = d_{Si(7\,7\,7)} \cdot \Delta\psi_{(hkil)}(T) \cdot \cos\left[\psi_{(hkil)}(100\,K)\right]. \qquad (5.1.1)$$

In both experiments, the λ-meter was mounted on a high-resolution angular rotation stage Kohzu[a] KTG-15 which has a step width of 25 nrad. The rotation angle ψ is measured with a Heidenhain[b] ROD800C angle encoder and an IK320 interpolation electronics, rendering an absolute angular resolution of 43 nrad.

For a perfectly stable setup, the angle ψ_M where the λ-meter selects the Mössbauer radiation should be constant during all runs of the experiment, since the relative stability of the wavelength of the Mössbauer radiation is about 10^{-13}, while the intrinsic relative width of the Si (7 7 7) reflection is about 3.5×10^{-7} for x-rays with $\lambda \approx 0.86$ Å. As shown in Fig. 5.1.2, in practice this is not the case. Thus we can see the stability of our setup from the variation of ψ_M from run to run.

The angular acceptance of the (7 7 7) Bragg reflection in Si for x-rays with $\lambda \approx \lambda_M$ is 1.2 µrad, corresponding to an energy bandpass of 5.3 meV and an intrinsic relative width $\Delta\lambda/\lambda = 3.5 \times 10^{-7}$. Thus it should be possible to measure wavelengths with a better relative accuracy than 10^{-7}. To achieve this goal it is necessary that both the angular divergence and the variation of the
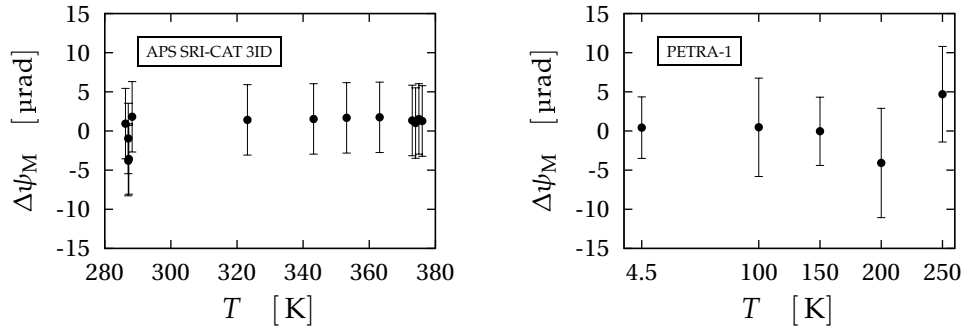
Fig. 5.1.2: Variation from run to run of the angle ψ_M where the λ-meter selects the wavelength of the Mössbauer radiation of ^{57}Fe for the experiment at APS (left panel) and for the experiment at PETRA-1 (right panel). The errorbars denote the width of the respective rocking curve.

direction of the incident beam are below the 1.2 µrad limit imposed by the angular acceptance of the $(7\,7\,7)$ reflection.

Two vertical slits in the beam path, between beam source and λ-meter, were used to narrow down the beam divergence close to this limit. At APS, they were installed at distances of 32.4 m and 59 m from the undulator which acts as the radiation source. The aperture of both slits was 60 µm. This should, for geometrical reasons, provide an angular divergence of 2.3 µrad. At PETRA-1, there were two slits installed about 107 m and 121 m from the source with a vertical aperture of 200 µm. A beam divergence of 1.7 µrad was expected.

Unfortunately, the beam divergence—determined from the width (FWHM) of the angular reflection curve measured with Mössbauer radiation, which also is shown in Fig. 5.1.2—was much broader at both beamlines: 9 µrad at APS, and about 10 µrad at PETRA-1. This large divergence deteriorates the accuracy of the measurements. It may be attributed to scattering from the beryllium windows in the beam path, or—at PETRA-1—from the components of the high heat load monochromator (diamond $(1\,1\,\overline{1})$ in Laue geometry, and Ge $(2\,2\,0)$) which are located about 10 m upstream of the second slit. The quality of the λ-meter Si crystal is probably not the origin of this problem, since the same crystal provided a beam divergence of about 1 µrad at the 1 km beamline at SPring-8 (see p. 57).

The APD detector was of the same type that was used in the experiment on the measurement of the Mössbauer radiation wavelength of ^{57}Fe, cf. p. 47.

5.1.4. Results of the lattice parameter measurements

For each crystal temperature, the angular differences $\Delta\psi_{(hkil)} = \psi_{(hkil)} - \psi_M$ have been measured for four different $(hkil)$ back-reflections as listed in Tab. 5.1.1. This allows us to compose four different sets, each with three equations of type Eq. 4.2.9, yielding its own solution for the three free parameters a, c, and $d^\star$ of the problem. An iteration procedure is used to solve these nonlinear systems of equations.

From the four independent solutions, the averaged values of a and c and their standard errors can be computed. However, we have ignored the solution resulting from the combination of $(0\ 0\ 0\ 30)$, $(2\ 6\ \overline{8}\ 20)$, and $(1\ 6\ \overline{7}\ 22)$ reflections, since it yields systematically significantly different values—see Fig. 5.1.5. The average values were computed only from the three remaining combinations. This is attributed to the fact that the $(2\ 6\ \overline{8}\ 20)$ and $(1\ 6\ \overline{7}\ 22)$ atomic planes are only $\approx 7°$ apart from each other (cf. Tab. 5.1.1), which—together with non-perfect crystal quality and temperature gradients—may increase the error.

Mean values and relative errors of a and c are given in Tab. 5.1.2 for different temperatures in units of λ_M and units of Å. In the unit conversion from λ_M to Å the value $\lambda_M = 0.860\,254\,74(16)$ Å from Shvyd'ko et al. (2000) was used. The errors of $\tilde{a}$ and $\tilde{c}$ are primarily due to the averaging process, as described above. The error introduced by the uncertainty in T is about two orders of magnitude smaller. The relative errors of the lattice parameters in metric units, a and c, are slightly larger than the errors of $\tilde{a}$ and $\tilde{c}$ because the relative error of λ_M, which is 1.9×10^{-7}, must also be considered.

The smaller relative error in the determination of the lattice parameter c compared with that of the a is evidently due to the fact that all reciprocal lattice vectors of the back-reflections used in the measurements are much closer to the c-axis of the crystal.

5.1.5. Discussion

In the Debye model of thermal expansion, the linear expansion coefficient ρ has a T^3 dependence for $T \to 0$, and is constant for $T > \Theta_D$, where Θ_D is the Debye temperature (Ashcroft and Mermin, 1976). We have fitted the following function that resembles this behavior to the data we have measured:

$$x(T) = \left(x_{44}T^4 + x_{04}\right) w(T) + \left(x_{11}T + x_{01}\right) \left[1 - w(T)\right]$$

$$w(T) = \cfrac{1}{1 + \exp \cfrac{\sqrt{T} - \sqrt{\Theta_x}}{\sqrt{\Delta\Theta_x}}}. \tag{5.1.2}$$

Herein, x takes the values a or c, respectively. The polynomial terms in parentheses represent the asymptotic temperature dependences of ρ as described above, and $w(T)$ and $1 - w(T)$ are weighting factors that provide a smooth transition between the $T \to 0$ and $T \to \infty$ regions. For $T = 0$, the second weighting factor vanishes, and for $T \to \infty$ the first one. The transition region is centered around Θ_x where both weighting factors equal 0.5, and the width

$T[\,\mathrm{K}]$	$\widetilde{a}[\lambda_{\mathrm{M}}]$	$\widetilde{c}[\lambda_{\mathrm{M}}]$	$a[\,\text{Å}]$	$c[\,\text{Å}]$	$\delta\widetilde{a}/\widetilde{a}$	$\delta\widetilde{c}/\widetilde{c}$
374.287(10)	5.534804	15.109758	4.761341	12.998241	6.3×10^{-7}	0.77×10^{-7}
373.304(10)	5.534768	15.109658	4.761310	12.998155	2.1×10^{-7}	0.77×10^{-7}
371.339(10)	5.534699	15.109478	4.761251	12.998000	6.3×10^{-7}	$1.5\ \times10^{-7}$
361.661(9)	5.534379	15.108467	4.760976	12.997130	6.3×10^{-7}	0.77×10^{-7}
351.836(9)	5.534064	15.107456	4.760705	12.996261	16.8×10^{-7}	$2.3\ \times10^{-7}$
342.010(9)	5.533741	15.106472	4.760427	12.995414	10.5×10^{-7}	$1.5\ \times10^{-7}$
332.184(9)	5.533428	15.105504	4.760158	12.994581	8.4×10^{-7}	$1.5\ \times10^{-7}$
322.359(9)	5.533110	15.104526	4.759884	12.993740	6.3×10^{-7}	0.77×10^{-7}
312.533(9)	5.532822	15.103584	4.759636	12.992930	10.5×10^{-7}	$1.5\ \times10^{-7}$
288.108(8)	5.532106	15.101369	4.759020	12.991024	16.8×10^{-7}	$3.1\ \times10^{-7}$
287.125(8)	5.532083	15.101278	4.759001	12.990946	21.0×10^{-7}	$3.9\ \times10^{-7}$
286.968(8)	5.532080	15.101262	4.758998	12.990932	18.9×10^{-7}	$3.1\ \times10^{-7}$
286.143(8)	5.532056	15.101192	4.758977	12.990872	8.4×10^{-7}	$1.5\ \times10^{-7}$
250.0	5.5310735	15.0982130	4.7581322	12.9883093	4.7×10^{-6}	$8.1\ \times10^{-7}$
200.0	5.5300551	15.0948850	4.7572561	12.9854463	4.2×10^{-6}	$8.0\ \times10^{-7}$
150.0	5.5293469	15.0925178	4.7566469	12.9834100	2.2×10^{-6}	$4.5\ \times10^{-7}$
100.0	5.5290080	15.0912297	4.7563553	12.9823018	4.3×10^{-6}	$9.4\ \times10^{-7}$
100.0	5.5290324	15.0912367	4.7563763	12.9823079	5.9×10^{-6}	$4.1\ \times10^{-6}$
95.0	5.5290134	15.0911419	4.7563600	12.9822264	6.0×10^{-6}	$4.0\ \times10^{-6}$
90.0	5.5289856	15.0910917	4.7563361	12.9821832	5.9×10^{-6}	$4.1\ \times10^{-6}$
85.0	5.5289794	15.0910209	4.7563308	12.9821223	5.9×10^{-6}	$4.1\ \times10^{-6}$
80.0	5.5289735	15.0909606	4.7563257	12.9820703	6.0×10^{-6}	$4.1\ \times10^{-6}$
75.0	5.5289658	15.0909087	4.7563191	12.9820257	5.9×10^{-6}	$3.6\ \times10^{-6}$
70.0	5.5289413	15.0909148	4.7562980	12.9820310	5.9×10^{-6}	$4.2\ \times10^{-6}$
65.0	5.5289384	15.0908806	4.7562954	12.9820015	5.9×10^{-6}	$4.1\ \times10^{-6}$
60.0	5.5289078	15.0908808	4.7562691	12.9820018	5.7×10^{-6}	$4.1\ \times10^{-6}$
55.0	5.5289012	15.0908693	4.7562634	12.9819919	5.7×10^{-6}	$4.2\ \times10^{-6}$
50.0	5.5289011	15.0908634	4.7562634	12.9819867	5.8×10^{-6}	$4.1\ \times10^{-6}$
45.0	5.5289063	15.0908324	4.7562679	12.9819601	5.7×10^{-6}	$4.1\ \times10^{-6}$
40.0	5.5289057	15.0908153	4.7562674	12.9819454	5.7×10^{-6}	$4.1\ \times10^{-6}$
35.0	5.5289047	15.0908079	4.7562665	12.9819390	5.8×10^{-6}	$4.1\ \times10^{-6}$
30.0	5.5289001	15.0908002	4.7562625	12.9819324	5.7×10^{-6}	$4.1\ \times10^{-6}$
30.0	5.5288962	15.0908002	4.7562592	12.9819324	5.6×10^{-6}	$4.1\ \times10^{-6}$
30.0	5.5288960	15.0908002	4.7562590	12.9819324	5.5×10^{-6}	$4.1\ \times10^{-6}$
25.0	5.5289025	15.0907940	4.7562646	12.9819271	5.6×10^{-6}	$4.0\ \times10^{-6}$
25.0	5.5288896	15.0908062	4.7562535	12.9819375	5.7×10^{-6}	$4.0\ \times10^{-6}$
25.0	5.5289293	15.0908062	4.7562876	12.9819375	5.9×10^{-6}	$4.0\ \times10^{-6}$
20.0	5.5289209	15.0908316	4.7562804	12.9819594	5.9×10^{-6}	$4.2\ \times10^{-6}$
20.0	5.5289331	15.0907962	4.7562909	12.9819289	5.9×10^{-6}	$4.0\ \times10^{-6}$
15.0	5.5289219	15.0908227	4.7562813	12.9819517	5.8×10^{-6}	$4.3\ \times10^{-6}$
15.0	5.5289343	15.0907928	4.7562919	12.9819260	5.8×10^{-6}	$3.9\ \times10^{-6}$
10.0	5.5289227	15.0908102	4.7562819	12.9819410	5.9×10^{-6}	$4.2\ \times10^{-6}$
4.5	5.5289188	15.0908190	4.7562786	12.9819485	5.9×10^{-6}	$4.2\ \times10^{-6}$

Tab. 5.1.2: Lattice parameters of $\alpha-\mathrm{Al}_2\mathrm{O}_3$ in units of λ_{M} and Å. For the unit conversion the λ_{M} value from Shvyd'ko et al. (2000) was used. The double line separates the results from the experiments at APS (above) and PETRA-1 (below). The single line separates the results from PETRA-1 which were obtained with the direct (above) or the relative (below) measurement method. Refer to Tab. 3.2.1 for the accuracy of the temperature readings at PETRA-1.
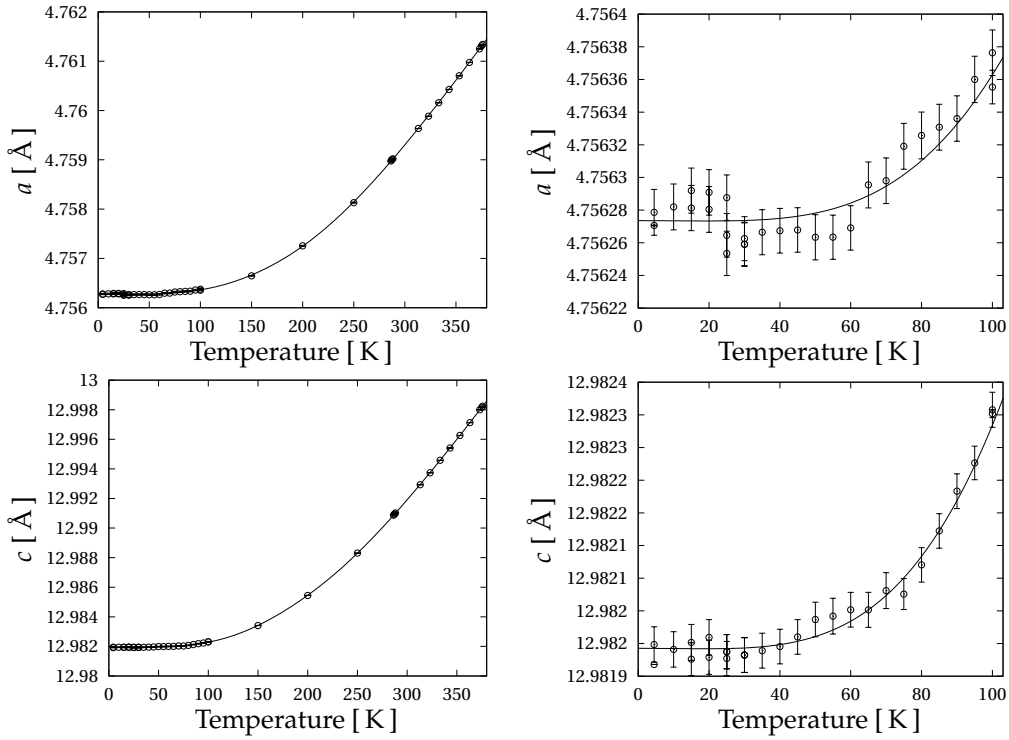
Fig. 5.1.3: Lattice parameters a and c in $\alpha-Al_2O_3$. Left panels: Results for the whole temperature range. Right panels: Detailed view on the results for temperatures below 100 K. The solid lines are fits with functions Eq. 5.1.2 and the parameters from Eq. 5.1.4.
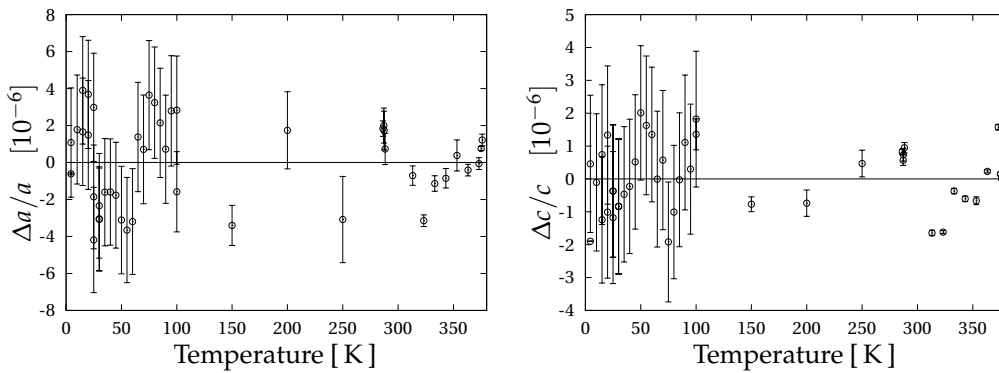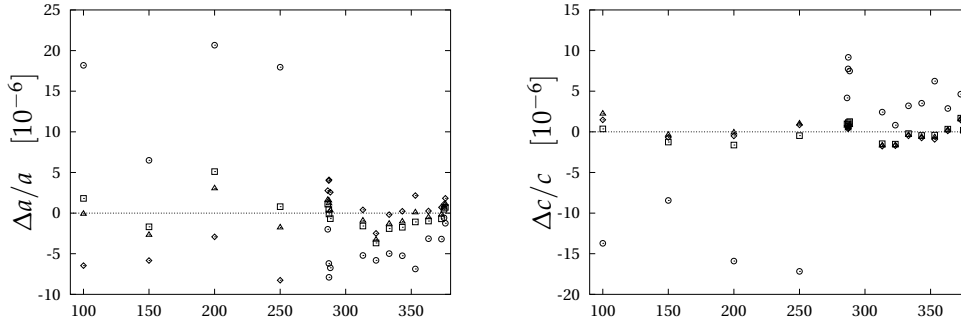

Fig. 5.1.4: Deviation of the measured lattice parameters a and c in $\alpha-Al_2O_3$ from the fit function Eq. 5.1.2 with parameters from Eq. 5.1.4.

of the transition region is indicated by $\Delta\Theta_x$. The square root dependency in the weighting factors makes the transition region asymmetric, extending more to higher than to lower temperature. This provides a remarkably better fit than with a symmetric transition, i.e. without the square root. Since the weighting factor of the low temperature term extends far into the range above Θ_x, the Debye temperature is expected to be $\Theta_D \gg \Theta_x$. The Debye temperature can be estimated to be $995\,K$ for the sub-lattice of O atoms, and $890\,K$ for the Al sub-lattice (see Shvyd'ko, 2002, p.63).

From Eq. 5.1.2 one can now calculate the linear thermal expansion coefficients for the limiting cases of low and high temperature[a]:

$$
\begin{aligned}
\rho_x(T) &= 4\,x_{44}/x(0\,\mathrm{K}) \cdot T^3 \quad \text{for} \quad T \to 0 \\
\rho_x(T) &= \quad x_{11}/x(374\,\mathrm{K}) \quad \text{for} \quad T \gg \Theta_x.
\end{aligned}
\tag{5.1.3}
$$

One expects that the fit for $a(T)$ and $c(T)$ should lead to $\Theta_a \approx \Theta_c$, and $\Delta\Theta_a \approx \Delta\Theta_c$.

The best fit parameters were found to be

$$
\begin{aligned}
a_{04} &= 4.756274(4) &&\times 10^{-10}\ \mathrm{m} \\
a_{44} &= 1.5(1.0) &&\times 10^{-22}\ \mathrm{m \cdot K^{-4}} \\
a_{01} &= 4.7501(4) &&\times 10^{-10}\ \mathrm{m} \\
a_{11} &= 2.95(9) &&\times 10^{-15}\ \mathrm{m \cdot K^{-1}} \\
\Theta_a &= 193(30) && \mathrm{K} \\
\Delta\Theta_a &= 1.0(3) && \mathrm{K} \\
c_{04} &= 12.981943(4) &&\times 10^{-10}\ \mathrm{m} \\
c_{44} &= 5.8(1.1) &&\times 10^{-22}\ \mathrm{m \cdot K^{-4}} \\
c_{01} &= 12.9633(5) &&\times 10^{-10}\ \mathrm{m} \\
c_{11} &= 9.2(1) &&\times 10^{-15}\ \mathrm{m \cdot K^{-1}} \\
\Theta_c &= 187(7) && \mathrm{K} \\
\Delta\Theta_c &= 0.99(9) && \mathrm{K}
\end{aligned}
\tag{5.1.4}
$$

The solid lines in Fig. 5.1.3 are the fit functions, Eq. 5.1.2, with the parameters from Eq. 5.1.4.

The fit curves are shown in Fig. 5.1.3 together with the measured results for a and c. Figure 5.1.4 shows the deviation of the measured results from the fit. As we can see there the relative accuracy of the fit is about 4×10^{-6} which is close to the measurement uncertainty at low temperature, but worse than the uncertainty of the measurements at higher temperature.

The better accuracy of the APS measurements is directly related to the error which is introduced by averaging over different combinations of back-reflections. In Fig. 5.1.5 the results for the lattice parameters are shown separately for each of the four possible combinations. The figure shows three remarkable results:

---

[a]The value $374\,K$ in the second line in Eq. 5.1.3 is the maximum temperature used in the determination of the fit.

Fig. 5.1.5: Deviation of the measured lattice parameters a and c in $\alpha-\mathrm{Al_2O_3}$ from the fit function Eq. 5.1.2 with parameters from Eq. 5.1.4, shown separately for the results from the four different combinations of back-reflections.

$\square$: $(1\,3\,\overline{4}\,28)$, $(0\,0\,0\,30)$, $(1\,6\,\overline{7}\,22)$; $\diamond$: $(1\,3\,\overline{4}\,28)$, $(0\,0\,0\,30)$, $(2\,6\,\overline{8}\,20)$;

$\triangle$: $(1\,3\,\overline{4}\,28)$, $(1\,6\,\overline{7}\,22)$, $(2\,6\,\overline{8}\,20)$; $\circ$: $(0\,0\,0\,30)$, $(1\,6\,\overline{7}\,22)$, $(2\,6\,\overline{8}\,20)$.

The $\circ$ values are ignored in computing the average since they are systematically significantly different from the other values.

1. The values of the lattice parameters for different combinations of back-reflections are scattered over a broader range in the low temperature region (below 250 K) than in the high temperature region.

2. The lattice parameters resulting from the combination $(0\,0\,0\,30)$ $(1\,6\,\overline{7}\,22)$ $(2\,6\,\overline{8}\,20)$ are significantly different from the results of the other combinations. Therefore, they were ignored in computing the averaged lattice parameters, as discussed on p. 69.

3. For the combination $(0\,0\,0\,30)$ $(1\,6\,\overline{7}\,22)$ $(2\,6\,\overline{8}\,20)$, in the low temperature region the results for a are higher and the results for c are lower than the results from the other combinations, while in the high temperature region the order is reversed.

Since the major difference between the low and high temperature experiments is the device which was used to control the temperature of the $\alpha-\mathrm{Al_2O_3}$ crystal, it is possible that these effects are a consequence of different temperature gradients across the crystal which are resulting from the respective construction of the cryostat and the oven, cf. Sections 3.2.1 and 3.2.2.

From Eqs. 5.1.3 and 5.1.4 we obtain the following approximate expressions for the thermal expansion coefficients in the limiting cases:

$$
\begin{aligned}
\rho_a &= 1.3(1.0) \times 10^{-12}\,\mathrm{K^{-1}} \cdot (T/\mathrm{K})^3 &\quad \text{for} \quad & T \to 0 \\
\rho_c &= 1.79(35) \times 10^{-12}\,\mathrm{K^{-1}} \cdot (T/\mathrm{K})^3 &\quad \text{for} \quad & T \to 0 \\
\rho_a &= 6.2(2) \quad \times 10^{-6}\;\mathrm{K^{-1}} &\quad \text{for} \quad & T \gg 200\,\mathrm{K} \\
\rho_c &= 7.07(8) \quad \times 10^{-6}\;\mathrm{K^{-1}} &\quad \text{for} \quad & T \gg 200\,\mathrm{K}
\end{aligned}
\tag{5.1.5}
$$

Independently from our work, a result for the thermal expansion of $\alpha-\mathrm{Al_2O_3}$ at low temperature was recently published by Seel et al. (1997). By

modulating the temperature of a cryogenic optical resonator and observing the resulting change in resonator frequency, they have determined the thermal expansion of $\alpha-Al_2O_3$ in c-direction at 1.9 K as $5 \times 10^{-12}\,\mathrm{K}^{-1}$. The uncertainty was not reported. By extrapolation of our results using Eq. Eq. 5.1.5 in the low temperature range, we obtain $12.3(2.4) \times 10^{-12}\,\mathrm{K}^{-1}$, which is more than twice as high as the result of Seel et al. (1997). This difference is remarkably large; however, the results are difficult to compare because of the following reasons: Firstly, our value for the thermal expansion of $\alpha-Al_2O_3$ in c-direction at 1.9 K is not the result of a direct measurement at that temperature, but of an extrapolation from measurements over a broad temperature range at higher temperatures, under the assumption that the Debye model is valid. Secondly, in the work of Seel et al. (1997) the thermal expansion was measured directly at 1.9 K, but no error was reported. Since only one significant digit is given in the result, one must assume that the error is at least 10%. Thirdly, the accuracy of our method for the measurement of the lattice parameters is about 10^{-6} in the low temperature region. The difference between the the thermal expansion coefficients of $\alpha-Al_2O_3$ in c-direction at 1.9 K reported by Seel et al. (1997) and the value extrapolated from our measurements would, however, lead to a change in the lattice parameter c of only about 10^{-11}. Thus, our method seems to be too insensitive to detect such a small difference, and the extrapolation using Eq. 5.1.5 should be considered only as an approximation.

We have also applied a 6$^{\text{th}}$ order polynomial fit to the lattice parameters measured in the $285.9\ldots374.3$ K temperature range (cf. Shvyd'ko et al., 2002):

$$a[\text{Å}] \quad = \quad \sum_{i=0}^{6} p_i \left(T[\mathrm{K}]\right)^i \qquad c[\text{Å}] \quad = \quad \sum_{i=0}^{6} q_i \left(T[\mathrm{K}]\right)^i$$

$$=$$

$$
\begin{aligned}
p_0 &= 16.59120 & q_0 &= 13.05720 \\
p_1 &= -0.2219875 & q_1 &= -8.895871 \cdot 10^{-4} \\
p_2 &= 1.7306085 \cdot 10^{-3} & q_2 &= 3.922787 \cdot 10^{-6} \\
p_3 &= -7.1775855 \cdot 10^{-6} & q_3 &= -7.039581 \cdot 10^{-9} \\
p_4 &= 1.6704009 \cdot 10^{-8} & q_4 &= 4.768008 \cdot 10^{-12} \\
p_5 &= -2.0681896 \cdot 10^{-11} & q_5 &= -5.355554 \cdot 10^{-19} \\
p_6 &= 1.0643281 \cdot 10^{-14} & q_6 &= 6.789434 \cdot 10^{-22}
\end{aligned}
\tag{5.1.6}
$$

Within this temperature range, the accuracy of the fit is about 10^{-6}, which is four times better than the accuracy of Eqs. 5.1.2 and 5.1.4. However, Eq. 5.1.6 is inapplicable for extrapolation outside the $285.9\ldots374.3$ K temperature range, and does not correspond to any theoretical model of thermal expansion. From Eq. 5.1.6 one can compute the following values for the lattice parameters of $\alpha-Al_2O_3$ at room temperature, $T = 295.65$ K:

$$
\begin{aligned}
a_{\text{RT}} &= 4.759\,213(8)\ \text{Å} \\
c_{\text{RT}} &= 12.991\,586(4)\ \text{Å}.
\end{aligned}
\tag{5.1.7}
$$

In Fig. 5.1.3 one can see a large variation of a at 25 K. This is corresponding to a drift of $\psi_{(1\,6\,\overline{7}\,22)}$ of about 9 µrad which was directly observed in three sub-

sequent measurements at the same temperature of the backscattering crystal. Approximately the same variation was observed in the measurements of ψ_M, cf. Fig. 5.1.2. This may be attributed to the sensitivity of the λ-meter table or the high heat load monochromator to changes in environmental temperature, which are originating from insufficient shielding of the beamline building.

5.1.6. Demonstration of the prediction of the relevant crystal temperature for backscattering

As a demonstration how the results from this experiment can be used, on can make an estimation where the $(1\,6\,\overline{7}\,22)$ back-reflection will reflect the delayed Mössbauer photons from ^{57}Fe. By inserting Eq. 5.1.2 for both lattice parameters $a(T)$ and $c(T)$ with the fit parameters from Eq. 5.1.4 into Eq. 4.2.11 with $(h\,k\,i\,l) = (1\,6\,\overline{7}\,22)$, one can find numerically that the relation $2\,d_{(1\,6\,\overline{7}\,22)}(T)\cdot(1-w_H) = \lambda_M$ should be fulfilled for $T = 159$ K. The uncertainty of this predicted temperature is assumed to be in the range of 1 K, since the linear thermal expansion coefficients are about 10^{-6} K^{-1}, and the measurement accuracy of the lattice parameters is also about 10^{-6}. Thus, a change of the temperature by 1 K would change the lattice parameters only within their measurement uncertainty.

According to these considerations, in the last few hours of the experiment at PETRA we have tried to find at which temperature the $\alpha-$Al$_2$O$_3$ crystal in $(1\,6\,\overline{7}\,22)$ backscattering position would indeed reflect the delayed Mössbauer photons from the ^{57}Fe foil. With temperature scans in the proximity of the expected temperature the backscattering of Mössbauer photons was found at 158.8 K. The final scan, which covers a temperature interval of 0.6 K, is shown in Fig. 5.1.6.

Together with $(1\,3\,\overline{4}\,28)$ which was used in previous experiments (Shvyd'ko et al., 1998), we have now two back-reflections in $\alpha-$Al$_2$O$_3$ which are suitable for experiments with Mössbauer radiation from ^{57}Fe. The relation between the interplanar distance of these back-reflections and the wavelength of the Mössbauer radiation of ^{57}Fe is shown in Fig. 5.1.7.

In applications where a single back-scattering $\alpha-$Al$_2$O$_3$ crystal is to be used as a monochromator, the $(1\,6\,\overline{7}\,22)$ back-reflection is more favorable because its energy bandpass is only about 1.9 meV, compared to 5.8 meV for $(1\,3\,\overline{4}\,28)$. On the other hand, the $(1\,3\,\overline{4}\,28)$ reflection has a higher reflectivity of 0.87 while the reflectivity of the $(1\,6\,\overline{7}\,22)$ reflection is only 0.63. Thus, $(1\,3\,\overline{4}\,28)$ is preferred in applications like the x-ray Fabry-Pérot resonator (see Section 6.3), where high reflectivity is important.

However, in the measurement of $(1\,6\,\overline{7}\,22)$ shown in Fig. 5.1.6 the temperature width corresponds only to an energy width of about 5 meV. This is probably not only attributed to the crystal quality, but also to the fact that the cryostat used in the experiment is not optimized for good temperature homogeneity across the crystal. Another cryostat which should yield better results is currently under development, cf. Section 6.2.
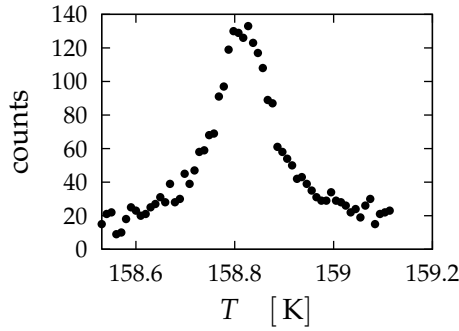
Si reference crystal

[1 1 0]

[h k l]

ψ

X-rays

$2\delta\theta$

50

987

988

Distance from the undulator [m]

at the beamline BL29XUL at SPring-8

993

Fig. 5.1.6: Temperature scan of Mössbauer photons from ^{57}Fe reflected by the $(1\,6\,\overline{7}\,22)$ back-reflection in $\alpha-\mathrm{Al}_2\mathrm{O}_3$. The sampling time was 60 s per data point.
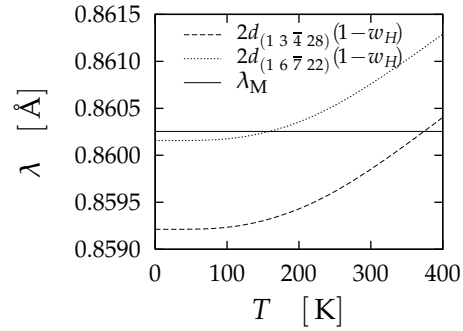
Fig. 5.1.7: Temperature dependence of selected interplanar distances in $\alpha-\mathrm{Al}_2\mathrm{O}_3$ where $2\,d_{(h\,k\,i\,l)}(1-w_H)$ is in the proximity of the Mössbauer radiation wavelength of ^{57}Fe, λ_{M}. At the intersection between the $2\,d_{(h\,k\,i\,l)}$ curve and the λ_{M} line the back-reflection $(h\,k\,i\,l)$ will reflect the Mössbauer radiation from ^{57}Fe.

5.2. Measurement of the wavelengths of the Mössbauer radiation of ^{119}Sn, ^{151}Eu, and ^{161}Dy

Besides ^{57}Fe, there are many other isotopes which can be used to generate Mössbauer radiation with uniquely low energy bandwidth and high stability. This can be achieved by exciting the appropriate nuclear transitions with synchrotron radiation. Attractive canditates are transitions to the low-lying excited states in ^{119}Sn, ^{151}Eu, and ^{161}Dy. The properties of the Mössbauer radiation from these isotopes are summarized in Tab. 5.2.1 (cf. Firestone et al., 1996), together with the composition of targets which can be used to generate the Mössbauer radiation.

Isotope	E_{M}	τ	Γ	Target
	[keV]	[ns]	[neV]	
^{57}Fe	14.4	141.2	4.7	α-^{57}Fe
^{151}Eu	21.5	13.8	47.5	^{151}EuO
^{119}Sn	23.8	26.0	25.3	^{119}Sn$_2$O
^{161}Dy	25.6	41.0	15.7	^{161}Dy (at 20 K)

Tab. 5.2.1: Excitation energy E_{M}, lifetime τ, and natural energy width Γ of selected Mössbauer nuclei.
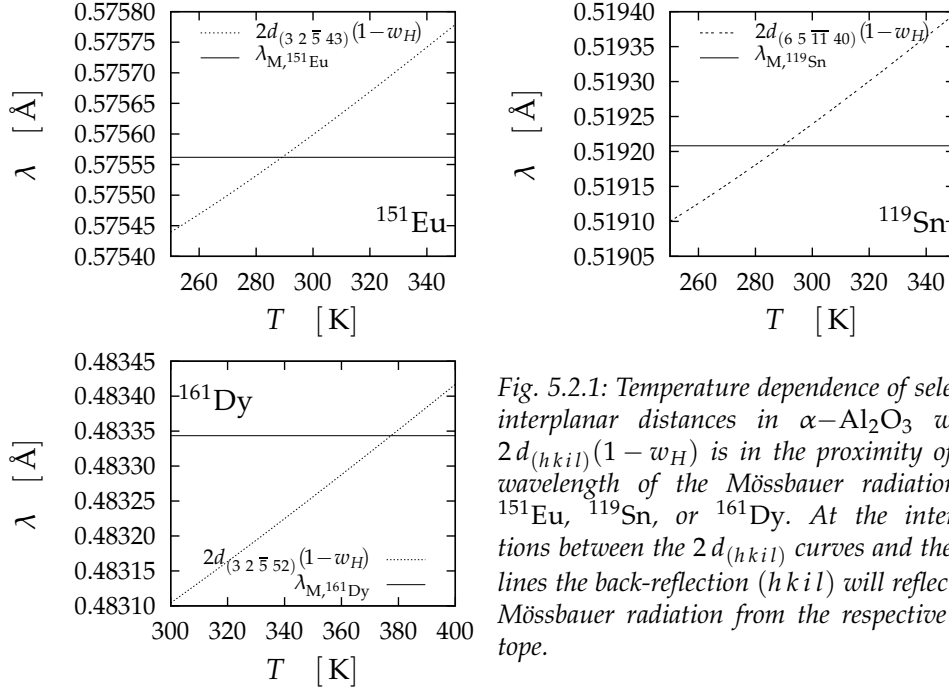
Fig. 5.2.1: Temperature dependence of selected interplanar distances in $\alpha-\mathrm{Al_2O_3}$ where $2\,d_{(hkil)}(1-w_H)$ is in the proximity of the wavelength of the Mössbauer radiation of ^{151}Eu, ^{119}Sn, or ^{161}Dy. At the intersections between the $2\,d_{(hkil)}$ curves and the λ_M lines the back-reflection $(hkil)$ will reflect the Mössbauer radiation from the respective isotope.

Isotope	$(h k i l)$	T	ΔT	ΔE	ΔE
			(exp.)	(exp.)	(theory)
		[K]	[mK]	[meV]	[meV]
^{57}Fe	$(1\,3\,\overline{4}\,28)$	371.582(8)	66	6.5	5.8
^{151}Eu	$(3\,2\,\overline{5}\,43)$	287.125(8)	67	8.3	0.6
^{119}Sn	$(6\,5\,\overline{11}\,40)$	286.968(10)	109	14.5	1.1
^{161}Dy	$(3\,2\,\overline{5}\,52)$	374.624(40)	46	7.6	0.7

Tab. 5.2.2: Miller indices $(h k i l)$, measured crystal temperature T and temperature width ΔT, and energy width ΔE of back-reflections in $\alpha-\mathrm{Al_2O_3}$ for the Mössbauer radiation of ^{57}Fe, ^{151}Eu, ^{119}Sn, and ^{161}Dy. Targets which can be used to generate the Mössbauer radiation with synchrotron radiation are also shown.

The wavelengths of the Mössbauer radiation of these isotopes could provide a set of reference wavelengths in the hard x-ray region.

For each isotope, a back-reflection in $\alpha-\mathrm{Al_2O_3}$ was selected with its Bragg wavelength $\lambda_B = 2d_{(hkil)}(1-w_H)$ being in the proximity of the wavelength of the Mössbauer radiation of the respective nucleus. They are listed in Tab. 5.2.2. As illustrated in Fig. 5.2.1, by tuning the temperature of the $\alpha-\mathrm{Al_2O_3}$ crystal it is possible to match the spectral range of a certain back-reflected radiation and the wavelength of the Mössbauer radiation of the respective isotope. These temperature values are shown in Tab. 5.2.2 too.

With the measured temperature dependence of the lattice parameters of sapphire (Tab. 5.1.2, Eq. 5.1.6), the crystal temperatues for backscattering of

Isotope	$\tilde{\lambda}_M[\lambda_{M,^{57}Fe}]$	$\delta\tilde{\lambda}_M/\tilde{\lambda}_M[10^{-7}]$	$\lambda_M[\text{Å}]$	$\delta\lambda_M/\lambda_M[10^{-7}]$	$E_M[\text{eV}]$
^{57}Fe	1.0	0	0.86025474(16)	1.9	14412.497(3)
^{151}Eu	0.66905978(28)	4.1	0.57556185(27)	4.7	21541.418(10)
^{119}Sn	0.60355158(43)	7.1	0.51920811(39)	7.4	23879.478(18)
^{161}Dy	0.56186073(18)	3.3	0.48334336(19)	4.0	25651.368(10)

Tab. 5.2.3: Wavelengths λ_M and energies E_M of the Mössbauer radiation of ^{151}Eu, ^{119}Sn, and ^{161}Dy, as determined by exact backscattering from a $\alpha-Al_2O_3$ crystal. The λ_M and E_M data for ^{57}Fe are from Shvyd'ko et al. (2000).

Mössbauer radiation (Tab. 5.2.2), and Eqs. 4.2.11, 4.2.5, it is now possible to determine wavelengths of the wavelength of the Mössbauer radiation of ^{151}Eu, ^{119}Sn, and ^{161}Dy. The results are presented in Tab. 5.2.3.

Our results agree well with the Mössbauer energy values previously reported by Koyama et al. (1996): $E_M = 21541.49(16)\,\text{eV}$ and Leupold et al. (1996): $E_M = 21541.7(5)\,\text{eV}$ for ^{151}Eu, by Kikuta (1994) for ^{119}Sn : $E_M = 23879.5(5)\,\text{eV}$, and by Koyama et al. (1996) for ^{161}Dy : $E_M = 25651.29(16)\,\text{eV}$. The relative uncertainty of our data is by more than one order of magnitude smaller.

The relative error in the determination of the wavelengths of the Mössbauer radiation is about $4\ldots7\times10^{-7}$. The major source of errors for the $\tilde{\lambda}_M$ values are the uncertainties in the in the lattice parameters of $\alpha-Al_2O_3$. The uncertainty in λ_M and E_M includes additionally the uncertainty of $\lambda_{M,^{57}Fe}$. The accuracy of the wavelengths of the Mössbauer radiation is deteriorated mostly by the large divergence of the incoming beam, which was about 9 µrad instead of the expected 2 µrad, and by crystal lattice defects in the $\alpha-Al_2O_3$ crystal. If everything were perfect the measurement accuracy could be improved by one order of magnitude.

Chapter 6

Outlook

6.1. Mössbauer radiation wavelengths of different isotopes as a set of reference wavelengths

The wavelengths of the Mössbauer radiation of ^{57}Fe, ^{151}Eu, ^{119}Sn, and ^{161}Dy (see Chapter 4, and Section 5.2) provide a set of reference wavelengths in the hard x-ray region. The advantages of Mössbauer radiation as a wavelength standard have already been discussed in the introduction of this thesis, and have been successfully demonstrated in the experiments described in Chapter 5, see also Lucht et al. (2003); Shvyd'ko et al. (2002). With the Mössbauer radiation of the abovementioned isotopes, there are now four reference wavelengths available which have a high accuracy of better than 10^{-6}, and are easy to reproduce. Besides the measurement of lattice parameters, they could also be useful for the calibration of high-resolution monochromators at synchrotron radiation facilities.

6.2. Cryogenic backscattering monochromator

Recent experiments with exact Bragg backscattering of x-rays (Lerche and Shvyd'ko, 2004; Lucht et al., 2003; Shvyd'ko et al., 1998, 2001, 2000, 2002) have used a temperature between $\approx 10\,^{\circ}$C and $\approx 100\,^{\circ}$C of the $\alpha-$Al$_2$O$_3$ crystal, depending on the wavelength of the radiation to be reflected, and the appropriately selected reflex ($h\,k\,i\,l$). Within this region, the effort which is necessary for the temperature control with mK stability is expected to remain manageable. However, for some applications the region from about 75 K to 250 K is of special interest, cf. Section 5.1.1. The cryostat (cf. Section 3.2.2) which was used for the measurement of the lattice parameters of $\alpha-$Al$_2$O$_3$ is, however, difficult to operate in this temperature region if high stability is required. This is mostly because the LHe flux and the two heaters have to be controlled simultaneously, and may influence each other due to the large temperature gradient between LHe and heaters. Also the cryostat is not optimized for good temperature homogeneity across the crystal.

A general disadvantage of LHe flow cryostats is the requirement for additional bulky equipment which is needed for operation. This includes the liquid helium containers and two vacuum pumps. Some experimental stations which are suitable for backscattering are too narrow to place this equipment close to the cryostat (e.g. BW4 at HASYLAB).

Slit
1
Slit
2
1 mm
(7 7 7)
λ-meter
^{57}Fe
APD
Detector
Oven
22.5 °C
Si reference crystal
[1 1 0]
[h k l]
ψ
X-rays
2δθ
50
987
988
Distance from the undulator [m]
at the beamline BL29XUL at SPring-8
993

Therefore, another cryostat has been constructed which uses LN_2[a)] as the chilling medium, and a single heater. This device is shown in Fig. 6.2.1.
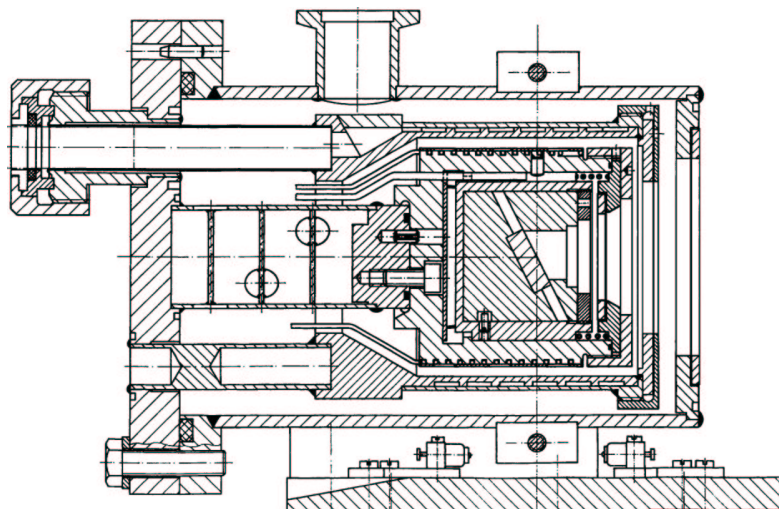

Fig. 6.2.1: Liquid Nitrogen flow cryostat for $\alpha-Al_2O_3$ backscattering experiments at temperatures between 77 K and room temperature

The design of the LN_2 flow cryostat follows the concept of the oven which was described in Section 3.2.1. The main difference is of course the LN_2 heat exchanger which is integrated in a thin shell between the outer vacuum tank and the inner sample holder. The latter one is made of copper and can hold samples with a diameter of up to 27 mm. The angle of the sample surface to the cryostat axis can be pre-adjusted by exchangeable copper blocks inside the sample holder. An electric heating wire is mounted on the outer surface of the copper shell. Together with a PT100 thermoresistor inside, it is possible to control the temperature of the sample using the same method as in the oven (Lucht, 1998). The minimum temperature (with heating off) is, in the ideal case, determined by the 77 K of the LN_2 in the heat exchanger. Since the sample is embedded in a thick copper shell, the temperature homogeneity is expected to be superior to the LHe cryostat where the sample is attached on the outer surface of a copper block.

Despite the larger diameter of the sample holder and the additional heat exchanger in the LN_2 cryostat, its outer diameter is the same as with the oven. Thus it is possible to use the same proven type of goniometer to hold the respective device and to orient the crystal.

At the time of writing, there is only very few experience how well the cryostat is working. First tests have shown that there is some considerable direct heat exchange between the inner copper block and the outer tank of the cryostat. Thus the temperature inside the sample holder remains higher than the temperature of the heat exchanger. One should examine further the heat transport processes inside the cryostat, using multiple temperature sensors. This

---

[a)]liquid nitrogen

will probably lead to some modifications of the construction. Also the temperature homogeneity inside the sample holder should be verified experimentally.

6.3.   X-Ray Fabry-Pérot resonator

The unique sharpness of the Mössbauer radiation of at least 10^{-11} is, unfortunately, not fully exploited in the present experiments. Thus the accuracy of the application of the Mössbauer wavelength standard remains several orders of magnitude below the intrinsic width of the Mössbauer radiation. This is not only due to the limits of the experimental method, but also due to the uncertainty of the underlying Si length standard itself, which is not better known than 10^{-8} (Bergamin et al., 1999). In the following a different approach is presented which could make it possible to overcome these restrictions.

In the visible spectral region ($\lambda \approx 400 \ldots 800\,\mathrm{nm}$) of the electromagnetic radiation, Fabry-Pérot resonators (Fabry and Pérot, 1899) are well established instruments for high-precision wavelength measurements in many fields of natural science, such as atomic spectroscopy, astrophysics, laser physics, and life sciences (Born and Wolf, 1980; Vaughan, 1989).

Recently, a prototype of a Fabry-Pérot resonator for hard x-rays has been successfully demonstrated by Shvyd'ko et al. (2003). Using the $(0\,0\,0\,30)$ reflection of two back-reflecting $\alpha-\mathrm{Al_2O_3}$ mirrors at $E = 14.315\,\mathrm{keV}$, the measured width of the Fabry-Pérot transmission resonances was $0.76\,\mathrm{\mu eV}$.

Since $\alpha-\mathrm{Al_2O_3}$ is transparent for visible light, it should be possible to realize combined mirrors for optical and x-ray wavelengths by coating the $\alpha-\mathrm{Al_2O_3}$ crystal with a thin metal film. A Fabry-Pérot resonator made of two such mirrors, as shown in Fig. 6.3.1, could be used for a direct measurement of the wavelength of the Mössbauer radiation of $^{57}\mathrm{Fe}$ in terms of the wavelength of an optical He-Ne laser, which has a relative accuracy and stability of about 10^{-11}.

Such an experiment will exploit the fact that the Fabry-Pérot resonances appear every time when the spacing between the mirrors is changed by $d = m \cdot \lambda/2$,[a)] where d is the gap width between the two mirrors, λ the wavelength of the incident laser beam or x-rays, respectively, and $m = 0, \pm 1, \pm 2, \pm 3 \ldots$. If the distance between the mirrors is varied by an amount which is a few times larger than the wavelength of the laser beam, one could directly count how many Mössbauer radiation wavelengths fit into one laser wavelength (Shvyd'ko, 2002). The uncertainty of such a measurement of the x-ray wavelength is basically limited by the accuracy of the laser wavelength, and thus by several orders of magnitude better than our current results which are based on the Si length standard.

Although this concept is in principle very simple, one has to face a lot of technical challenges, like the following: For the Mössbauer radiation of $^{57}\mathrm{Fe}$ to

---

[a)]Provided that the beams are perfecty perpendicular to the reflecting surfaces of the mirrors, otherwise an angular correction has to be applied. For optical and x-ray wavelengths, the gaps between the mirrors are slightly different, but since we deal only with the change of the gap, this uncertainty drops out.
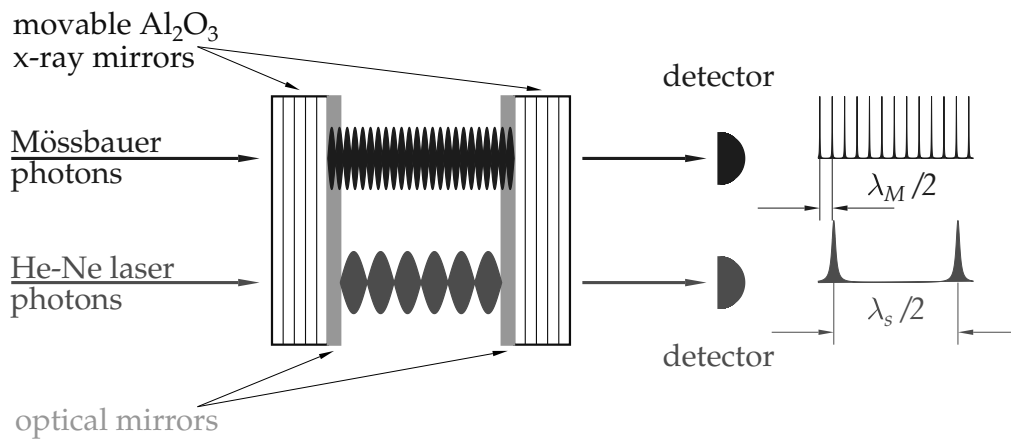
Slit
2
1 mm
Si (7 7 7)
λ-meter
^{57}Fe
APD
Detector
Oven
22.5 °C
Si reference crystal
[1 1 0]
[h k l]
ψ
X-rays
2δθ
50
987
988
993

ance from the undulator [m]

eamline BL29XUL at SPring-8

movable Al$_2$O$_3$
x-ray mirrors

detector

Mössbauer
photons

$\lambda_M/2$

He-Ne laser
photons

$\lambda_S/2$

detector

optical mirrors

Fig. 6.3.1: Combined x-ray Fabry-Pérot resonator for the comparison of the wavelength of the Mössbauer radiation and the wavelength of an optical He-Ne laser

be backreflected, the $(1\,3\,\overline{4}\,28)$ back-reflection has to be used, and the surface of the optical mirror has to be prepared to be precisely parallel to the x-ray reflecting atomic planes. Both mirrors must be aligned parallel with nrad accuracy, and this alignment must remain stable when the gap between the mirrors is varied over a μm distance. The temperature of the mirrors must be stabilized within a few mK at $\approx 100\,°C$ to tune the wavelength of the back-reflected x-rays to the wavelength of the Mössbauer radiation of ^{57}Fe (Shvyd'ko et al., 1998). This temperature region is not a good operating condition for the high-precision micro-motors which are necessary for the alignment and movement of the mirrors. The motors will also produce some additional heat during operation. This may deteriorate the temperature control for the mirrors, and, due to thermal expansion effects, the alignment of the setup. These problems have to be solved step-by step, and therefore some years of development will still be necessary to get the combined optical/x-ray Fabry-Pérot resonator working.

6.4. Experimental studies on multiple beam diffraction

In the experiment for the determination of the wavelength of the Mössbauer radiation of ^{57}Fe, we had to cope with multiple beam diffraction as an unwanted side effect of Bragg backscattering. This effect may lead to energy shifts and strongly reduced intensity of the reflected beam if one comes too close to the exact backscattering geometry (see Section 2.3). Multiple beam diffraction deserves, however, some comprehensive experimental studies on its own, and with the setup described in Chapter 4 one has everything at hand to do so.

In the experiment conducted at the 1 km beamline at SPring-8 in May 2001, we have attempted a short demonstration of the experimental observation of the effects described in Section 2.3. After adjusting exact backscattering for the
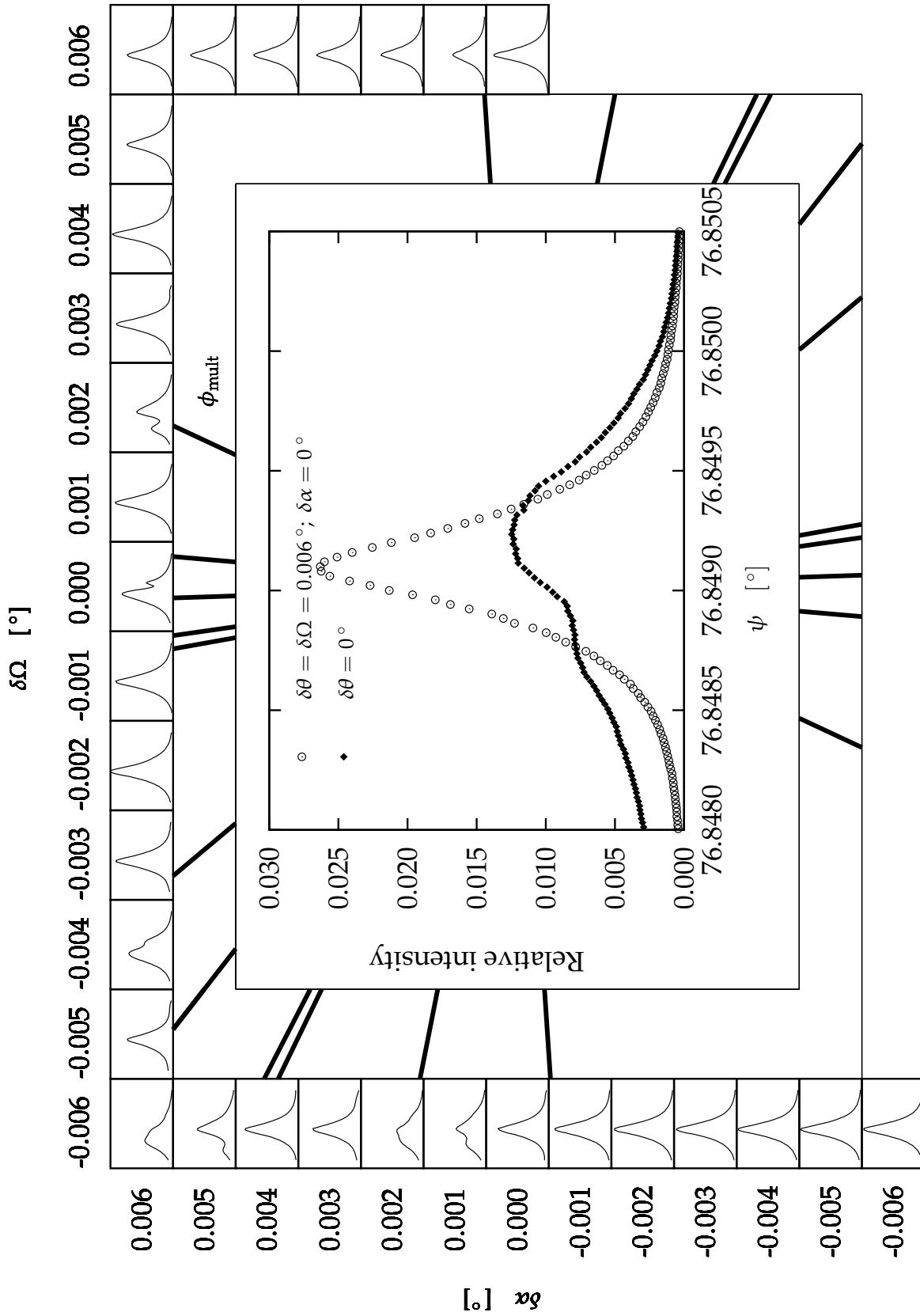
Fig. 6.4.1: Raw experimental data on the angular and energy dependence of multiple beam diffraction for the (9 7 5) back-reflection in Si. The photon energy is varied with the rotation angle ψ of the λ-meter. The large figure in the center shows an overlay of the energy dependence for the exact Bragg backscattering case ($\delta\theta = 0$) and for a near-backscattering case within the angular width of the back-reflection ($\delta\theta = 0.006° = 105\,\mu\text{rad}$). The small figures show the changes of the energy dependence while the azimuthal and deviation angles from exact backscattering (cf. Section 2.3) are varied by $\phi = \arctan(\delta\alpha/\delta\Omega) + \phi_0$ with $\phi_0 \approx 15.8°$, and $\delta\theta = \sqrt{\delta\Omega^2 + \delta\alpha^2}$. The ranges of ψ and intensity are the same for the large figure and all small figures. The bold radial lines denote the azimuthal directions ϕ_{mult} of the multiple beam cases from Tab. 2.3.1.

(9 7 5) reflection with an accuracy of about 10 μrad by using a 100 μm pinhole, the pinhole was removed and the raw data shown in Fig. 6.4.1 were measured. Herein, with the rotation angle ψ of the λ-meter the energy of the radiation is varied according to Bragg's law. The intensity scale shows the ratio between detected incident photons before they pass the λ-meter, and reflected photons from the Si reference crystal.

In the large figure one can see clearly the difference in the energy dependence between the exact backscattering case with $\delta\theta = 0$ and another case which is slightly off backscattering with $\delta\theta \approx 105$ μrad. In exact backscattering, the curve is not only broadened and has less peak intensity, but the peak is also shifted on the energy/angle scale and some non-pronounced side peak is showing up. The small figures show the energy dependence for near-backscattering cases with different azimuthal angles. The Si reference crystal was rotated around two axes Ω and α, which are perpendicular to each other and to the beam. For exact backscattering, $\delta\Omega = 0$ and $\delta\alpha = 0$. Then the azimuthal angle $\phi = \arctan(\delta\alpha/\delta\Omega) + \phi_0$ with $\phi_0 \approx 15.8\,°$, and the deviation from exact backscattering $\delta\theta = \sqrt{\delta\Omega^2 + \delta\alpha^2}$. For most azimuthal angles the abovementioned side effects of multiple beam diffraction vanish, and the curves are sharp and have high intensity. But there are some directions of ϕ where, with $\delta\theta \gtrsim 100$ μrad, the curves are broad, less intense, and sometimes even with pronounced additional peaks.

Due to the tight schedule of the experiment this study had to remain incomplete. The angles Ω and α were just varied in fixed steps, and no attempt was made to find the ϕ_{mult} values given in Tab. 2.3.1 exactly or to keep $\delta\theta$ constant. It is, however, evident that this experimental setup is suitable for the direct observation of the effects of multiple beam diffraction on Bragg backscattering. More detailed studies on this topic are desirable.

Bibliography

A. M. Afanas'ev and Y. Kagan. The role of lattice vibrations in dynamical theory of x-rays. *Acta Cryst. A*, 24:163, 1967.

P. Aldebert and J.P. Traverse. Neutron diffraction studies of structural characteristics and ionic mobility of $\alpha-Al_2O_3$ at high temperatures. *J. Am. Ceram. Soc.*, 65:460—464, 1982.

N.W. Ashcroft and N.D. Mermin. *Solid State Physics*. Saunders College, Philadelphia, 1976.

L. V. Azaroff, R. Kaplow, N. Kato, R. J. Weiss, A. J. C. Wilson, and R. A. Yung. *X-ray diffraction*. McGraw Hill, Inc., 1974.

A.Q.R. Baron. Detectors for nuclear resonant scattering experiments. *Hyperfine Interact.*, 125:29—42, 2000.

B. W. Batterman and H. Cole. Dynamical diffraction of x-rays by perfect crystals. *Rev. Mod. Phys*, 36:681–717, 1964.

J.A. Bearden. Selection of W $K_{\alpha 1}$ as the x-ray wavelength standard. *Phys. Rev.*, 137:B455—461, 1965.

P. Becker, 2001. Data sheet for the WASO04 Si reference crystal, internal documentation.

P. Becker, 2002. Private communication.

P. Becker, K. Dorenwendt, G. Ebeling, R. Lauer, W. Lucas, R. Probst, H.-J. Radermacher, G. Reim amd P. Seyfried, and H. Siegert. Absolute measurements of the (220) lattice spacing in a silicon crystal. *Phys. Rev. Lett*, 46:1540, 1981.

A. Bergamin, G. Cavagnero, and G. Mana. Lattice parameter and thermal expansion of monocrystalline silicon. *J. Appl. Phys.*, 82:5396–5400, 1997.

A. Bergamin, G. Cavagnero, G. Mana, and G. Zosi. Scanning x-ray interferometry and the silicon lattice parameter: towards 10^{-9} relative uncertainty? *Eur. Phys. J. B*, 9:225—232, 1999.

M. Born and E. Wolf. *Principles of Optics*. Pergamon Press, 1980.

C. Braxmaier, H. Müller, O. Pradl, J. Mlynek, A. Peters, and S. Schiller. Tests of relativity using a cryogenic optical resonator. *Phys. Rev. Lett*, 88:010401–1—010401–4, 2001.

A.S. Brown, M.A. Spackman, and R.J. Hill. The electron distribution in corundum. Study of the utility of merging single crystal and powder diffraction data. *Acta Cryst. A*, 49:513—527, 1992.

O. Brümmer, H. R. Höche, and J. Nieber. X-ray diffraction in the Bragg case at Bragg angles of about $\pi/2$. *Phys. Stat. Solidi (a)*, 53:565, 1979.

St. Burghartz and B. Schulz. Thermophysical properties of sapphire, AlN and $MgAl_2O_4$ down to 70 K. *Journal of Nuclear Materials*, 212–215:1065–1068, 1994.

A. Caticha and S. Caticha-Ellis. Dynamical theory of x-ray diffraction at angles near $\pi/2$. *Phys. Rev. B*, 25:971, 1982.

W. M. Chen, P. McNally, Yu. V. Shvyd'ko, T. Tuomi, M. Lerche, A. N. Danilewsky, J. Kanatharana, D. Lowney, M. O'Hare, L. Knuuttila, J. Riikonen, and R. Rantamäki. Quality assessment of sapphire wafers for x-ray crystal optics using white beam synchrotron x-ray topography. *physica status solidi (a)*, 186:365—371, 2001.

M. Deutsch and M. Hart. High energy x-ray anomalous dispersion correction for silicon. *Phys. Rev. B*, 37:2701—2703, 1988.

C. Fabry and A. Pérot. Theorie et applications d'une nouvelle methode de spectroscopie interferentielle. *Ann. Chim. Phys.*, 7:115, 1899.

R.B. Firestone, V.S. Shirley, S.Y.F. Chu, C.M. Baglin, and J. Zipkin. *Table of Isotopes*. John Wiley and Sons, New York, 1996.

H. Franz, B. Hukelmann, and J.R. Schneider. The nuclear-resonance-scattering station at the PETRA II undulator beamline. *Hyperfine Interactions*, 126:397—400, 2000.

E. Gerdau and H. de Waard, editors. *Nuclear Resonant Scattering of Synchrotron Radiation*. Baltzer, 1999/2000. special issues of the *Hyperfine Interact.*, vol. 123-125.

E. Gerdau, R. Rüffer, H. Winkler, W. Tolksdorf, C.P. Klages, and J.P. Hannon. Nuclear Bragg diffraction of synchrotron radiation in yttrium iron garnet. *Phys. Rev. Lett*, 54:835, 1985.

W. Graeff and G. Materlik. Milli-electronvolt energy resolution in Bragg backscattering. *Nucl. Instrum. Methods Phys. Res.*, 195:97, 1982.

P. Gütlich, R. Link, and A. Trautwein. *Mössbauer spectroscopy and transition metal chemistry*. Springer Verlag, Berlin, 1978.

U. Hahn, H. Schulte-Schrepping, K. Balewski, J.R. Schneider, P. Illinski, B. Lai, W. Yun, D. Legnini, and E. Gluskin. Measurements of emittance and absolute spectral flux of the PETRA undulator at DESY Hamburg. *J. Synchrotron Rad.*, 4:1—5, 1997.

J.B. Hastings, D.P. Siddons, U. van Bürck, R. Hollatz, , and U. Bergmann. Mössbauer spectroscopy using synchrotron radiation. *Phys. Rev. Lett.*, 66:770—773, 1991.

T. Ishikawa, K. Tamasaku, M. Yabashi, S. Goto, Y. Tanaka, H. Yamazaki, K. Takeshita, H. Kimura, H. Ohashi, T. Matsushita, and T. Ohata. One kilometer beamline at SPring-8. *SPIE Proceedings*, 4145:1—10, 2001.

R. W. James. *The Optical Principles of the Diffraction of X-rays in Crystals*. G. Bell & Sons, Ltd., 1950.

S. Kikuta. Studies of nuclear resonant scattering at TRISTAN-AR. *Hyperfine Interact.*, 90:335—349, 1994.

A. Kirfel and K. Eichhorn. Accurate structure analysis with synchrotron radiation. The electron density in $\alpha-Al_2O_3$ and Cu_2O. *Acta Cryst. A*, 46:271—283, 1990.

L. Kissel and R.H. Pratt. Corrections to tabulated anomalous scattering factors. *Acta Cryst. A*, 46:170—175, 1990. Also available from http://www-phys.llnl.gov/Research/scattering.

L. Kissel, B. Zhou, S. C. Roy, S. K. S. Gupta, and R. H. Pratt. Validity of form-factor, modified-form-factor and anomalous-scattering-factor approximations in elastic scattering calculations. *Acta Cryst. A*, 51:271—288, 1995.

V. G. Kohn, I. V. Kohn, and E. A. Manykin. Diffraction of x-rays at a Bragg angle of $\pi/2$ (back reflection) with consideration of multi-wave effects. *JETP*, 89:500, 1999.

K. Kohra and T. Matsushita. Some characteristics of dynamical diffraction at a Bragg angle of about $\pi/2$. *Z. Naturforsch. A*, 27:484, 1972.

I. Koyama, Y. Yoda, X.W. Zhang, M. Ando, and S. Kikuta. Nuclear resonant scattering of ^{161}Dy and ^{151}Eu by synchrotron radiation. *Japn. J. Appl. Phys.*, 35:6297—6300, 1996.

T. Kracht, J.R. Schneider, H. Schulte-Schrepping, and K. Joensen. Layout of the PETRA beamline for the energy range 8-56 keV. *HASYLAB annual report*, I:154—159, 1995.

Lake Shore. Temperature measurement and control, 1999. catalogue.

C.M. Lederer and V.S. Shirley. *Table of Isotopes*. John Wiley and Sons, New York, 1976.

M. Lerche. *Untersuchungen zum Bau eines Fabry-Perot-Interferometers f̈r Mössbauerstrahlung* . PhD thesis, University of Hamburg, 2004.

M. Lerche and Yu.V. Shvyd'ko. Multiple-beam Bragg diffraction in backscattering: The four-beam case. *Phys. Rev. B*, 70:134104–1, 2004.

O. Leupold, J. Pollmann, E. Gerdau, H. D. Rüter, G.Faigel, M.Tegze, G.Bortel, R.Rüffer, A.I.Chumakov, and A.Q.R.Baron. Nuclear resonant scattering of synchrotron radiation at the 21.5 keV resonance of ^{151}Eu. *Europhys. Lett.*, 35:671—675, 1996.

J. Lewis, D. Schwarzenbach, and H.D. Flack. Electric field gradients and charge density in corundum, $\alpha - Al_2O_3$. *Acta Cryst. A*, 38:733—739, 1982.

M. Lucht. A high-precision temperature control—applications in mono-chromatization and exact Bragg backscattering of synchrotron radiation., 1998. Univ. Hamburg, Diploma thesis (in German). Available from http://www.rrz.uni-hamburg.de/hfww/publications/diploma.html.

M. Lucht, M. Lerche, H.-C. Wille, Yu.V. Shvyd'ko, H. D. Rüter, E. Gerdau, and P. Becker. Precise measurement of the lattice parameters of $\alpha - Al_2O_3$ in the temperature range 4.5 K—250 K using the Mössbauer wavelength standard. *J. Appl. Cryst.*, 36:part 4, 1075—1081, 2003.

P. J. Mohr and B. N. Taylor. Special issue on the 1998 CODATA internationally recommended values. *Rev. Mod. Phys.*, 72:351—495, 2000.

R. L. Mössbauer. Kernresonanzfluoreszenz von Gammastrahlung in ^{191}Ir. *Z. für Physik*, 151:124, 1958.

Z.G. Pinsker. *Dynamical Scattering of x-rays in Crystals*. Springer, 1978.

F. Schmid, C.P. Khattak, and D.M. Felt. Producing large sapphire for optical applications. *Am. Ceram. Soc. Bull.*, 73:No.2, 39—49, 1994.

S. Seel, R. Storz, G. Ruoso, J. Mlynek, and S. Schiller. Cryogenic optical resonators: A new tool for laser frequency stabilization at the 1 Hz level. *Phys. Rev. Lett*, 78:4741—4744, 1997.

Yu.V. Shvyd'ko. *X-Ray Resonators and other Applications of Bragg Backscattering*. Habilitation thesis, DESY-THESIS-2002-028, ISSN 1435-8085, Hamburg, 2002.

Yu.V. Shvyd'ko. *X-Ray Optics: High Energy Resolution Applications*. Springer-Verlag, Heidelberg, 2004.

Yu.V. Shvyd'ko and E. Gerdau. Back-scattering mirrors for x-rays and Mössbauer radiation. *Hyperfine Interactions*, 123/124:741—776, 1999.

Yu.V. Shvyd'ko, E. Gerdau, J. Jäschke, O. Leupold, M. Lucht, and H.D. Rüter. Exact Bragg backscattering of x-rays. *Phys. Rev. B*, 57:4968—4971, 1998.

Yu.V. Shvyd'ko, M. Gerken, H. Franz, M. Lucht, and E. Gerdau. Nuclear resonant scattering of synchrotron radiation from ^{161}Dy at 25.61 keV. *Europhys. Lett.*, 56:309—315, 2001.

Yu.V. Shvyd'ko, M. Lerche, J. Jäschke, M. Lucht, E. Gerdau, M. Gerken, H.D. Rüter, H.-C. Wille, P. Becker, E.E. Alp, W. Sturhahn, J. Sutter, and T.S. Toellner. γ-ray wavelength standard for atomic scales. *Phys. Rev. Lett.*, 85: 495—498, 2000.

Yu.V. Shvyd'ko, M. Lerche, H.-C. Wille, E. Gerdau, H. D. Rüter, E. E. Alp, and R. Khachatryan. X-ray interferometry with micro-electronvolt resolution. *Phys. Rev. Lett.*, 90:013904, 2003.

Yu.V. Shvyd'ko, M. Lucht, E. Gerdau, M. Lerche, E.E. Alp, W. Sturhahn, J. Sutter, and T.S. Toellner. Measuring wavelengths and lattice constants with the Mössbauer wavelength standard. *J. Synchrotron Rad.*, 9:17—23, 2002.

Yu.V. Shvyd'ko, G.V. Smirnov, S.L. Popov, and T. Hertrich. Observation of the enhanced forward γ-emission in spontaneous nuclear decay. *Pis'ma. Zh. Eksp. Teor. Fiz.*, 53:69—73, 1991. [(1991) *JETP Lett.* **53**, 69-73].

D.P. Siddons, J.B. Hastings, and G. Faigel. A new apparatus for the study of nuclear Bragg scattering. *Nucl. Instrum. Methods*, A266:329—335, 1988.

A. Steyerl and K.-A. Steinhauser. Proposal of a fabry-perot-type interferometer for x-rays. *Z. Phys. B*, 34:221—227, 1979.

J. Sutter. *Applications of special x-ray diffraction cases in silicon crystals*. PhD thesis, Purdue University, 2000.

J. Sutter, 2001. Private communication.

K. Tamasaku, 2002. Private communication.

T. S. Toellner. Monochromatization of synchrotron radiation for nuclear resonant scattering experiments. *Hyp. Interact.*, 125:3, 2000.

Y. S. Touloukian and C. Y. Ho, editors. *Thermophysical Properties of Matter, Vol. 2, Thermal Conductivity – Nonmetallic solids*. IFI/PLENUM, New York - Washington, 1970.

T. Tuomi, K. Naukkarinen, and P. Rabe. Use of synchrotron radiation in in x-ray diffraction topography. *phys. stat. sol. (a)*, 25:93—106, 1974.

J. M. Vaughan. *The Fabry-Pérot Interferometer*. Hilger, 1989.

M. von Laue. Die dynamische Theorie der Röntgenstrahlinterferenzen in neuer Form. *Ergeb. Exakt. Naturwiss.*, 10:133—158, 1931.

Z. Xiaowei, Y. Yoda, and Y. Imai. Precision wavelength measurement of the 14.4 keV Mössbauer photon. *J. Synchrotron Rad.*, 7:189—195, 2000.

W.M. Yim and R.J. Paff. Thermal expansion of AlN, sapphire, and silicon. *J. Appl. Phys.*, 45:1456—1457, 1974.

W. H. Zachariasen. *Theory of X-ray Diffraction in Crystals*. John Wiley & Sons, Inc., 1945.

J. M. Ziman. *Principles of the theory of solids*. Cambridge University Press, 1969.

Acknowledgements

I am grateful Peter Becker from the PTB for providing the silicon reference crystals, for calibration of the temperature sensors, and for sharing his experience in high-precision wavelength measurements.

Furtermore, I want to thank Hermann Franz from HASYLAB for supporting our experiments at the PETRA I beamline.

Our research is highly dependent on specially constructed devices like oven, cryostat, sample holders, positioning stages, detectors, and so on. Many people at the Institut für Experimentalphysik in Hamburg were involved in these developments. I wish to thank our engineer Benno Frensche and his predecessor Dieter Giesenberg for their technical designs, and I also thank our draftswomen Margit Draht and Jutta Pelz who were temporarily on their own with our requests for new constructions. For manufacturing or repair of the equipment for our experiments I am grateful to the head of our precision engineering workshop, Jürgen Römmert and his predecessor Jürgen Weber, and also to the head of our electronics workshop, Armin Spikowsky. Karl Geske's experience in analogue electronics was indispensable for the construction and operation of the APD detectors.

Barbara Lohl's advices in any circumstances are very much appreciated, not only when it comes to bureaucracy and organisation. Many problems with unaccommodating vendors were solved by her sharp tongue on the telephone. Her five o'clock tea was the daily occasion for many stimulating discussions in our research group.

Finally, I wish to express my sincere gratitude to my parents for their continuous support during many years of education, even in hard times.

Munich, December 8, 2004
Martin Lucht